



University of
BRISTOL

Development & Implementation of the Trigger
for a Short-baseline Reactor Antineutrino
Experiment (SoLid)

Lukas On Arnold

A dissertation submitted to the University of Bristol in accordance with the requirements for award of the degree of Master of Science by Research in Physics in the Faculty of Science in March 2017

~ 20000 words

Abstract

SoLid, located at SCK-CEN in Mol, Belgium, is a reactor antineutrino experiment at a very short baseline of 5.5 – 10m aiming at the search for sterile neutrinos and for high precision measurement of the neutrino energy spectrum of Uranium-235. It uses a novel approach using Lithium-6 sheets and PVT cubes as scintillators for tagging the Inverse Beta-Decay products (neutron and positron).

Being located overground and close to the BR2 research reactor, the experiment faces a large amount of backgrounds. Efficient real-time background and noise rejection is essential in order to increase the signal-background ratio for precise oscillation measurement and decrease data production to a rate which can be handled by the online software. Therefore, a reliable distinction between the neutrons and background signals is crucial. This can be performed online with a dedicated firmware trigger. A peak counting algorithm and an algorithm measuring time over threshold have been identified as performing well both in terms of efficiency and fake rate, and have been implemented onto an FPGA.

After having introduced the experimental and theoretical background of neutrino oscillation physics, as well as SoLid's detector technology, read-out system and trigger scheme, the thesis presents the design of the firmware neutron trigger implemented by applying machine learning methods.

Acknowledgements

I would like to thank my supervisor, Dave Newbold, whose expertise and support in the field of trigger and firmware development has been of essential value in conducting the present research.

I also would like to express my thanks to David Cussans whose advice and competence in electronics and detector technology has been of greatest benefit.

I want to thank my other collaborators on SoLid, namely Nick Ryder, Dan Saunders, Steve Manley, Kostas Petridis, Jonas Rademacker, Sakari Ihantola, Antonin Vacheret, Simon Vercaemer and Yamiel Abreu, as well as Jules Desjardin, who was of great help as a summer student.

I also would like to acknowledge the scholarship provider, ZÜHLKE AG.

Author's declaration

I declare that the work in this dissertation was carried out in accordance with the requirements of the University's Regulations and Code of Practice for Research Degree Programmes and that it has not been submitted for any other academic award. Except where indicated by specific reference in the text, the work is the candidate's own work. Work done in collaboration with, or with the assistance of, others, is indicated as such. Any views expressed in the dissertation are those of the author.

Signed:

Date:

Contents

List of Figures	9
List of Tables	12
1 Introduction	13
2 Searching for Sterile Neutrinos	15
3 The SoLid Detector	35
4 The SoLid Read-out System	47
5 The SoLid Trigger	57
6 Conclusion	91
7 References	93
Appendix A	105

Contents (detailed)

List of Figures	9
List of Tables	12
1 Introduction	13
2 Searching for Sterile Neutrinos	15
2.1 Neutrinos in the Standard Model	15
2.2 Neutrinos beyond the Standard Model	16
2.2.1 Mass Mixing	16
2.2.2 Neutrino Oscillations	18
2.3 Neutrino Experiments	19
2.4 Reactor Antineutrino Emission	22
2.5 Reactor Anomaly	24
2.6 Gallium Anomaly	25
2.7 Accelerator Anomaly	27
2.8 The Sterile Neutrino Hypothesis	27
2.8.1 Sterile Neutrino Mass Mixing	28
2.8.2 Sterile Neutrino Oscillations	30
2.9 Other Applications of SoLid	32
2.9.1 5MeV Excess	33
2.9.2 Non-Proliferation	34
3 The SoLid Detector	35
3.1 BR2 Reactor	35
3.2 IBD Capture	37
3.2.1 Detector Components	37
The Cube	38
The Plane	38
The Module	38
3.2.2 Positron Capture	38
3.2.3 Neutron Capture	39
3.2.4 Light Capture	40
Wavelength-Shifting Fibres	40
Silicon Photomultipliers	41
3.2.5 Background	42
Cosmic Muons	42
Cosmogenic Background	42
Intrinsic Background	42
3.3 Status of the experiment	43

3.3.1	NEMENIX	43
3.3.2	SM1	43
3.3.3	Phase 1	44
3.3.4	Phase 2	45
4	The SoLid Read-out System	47
4.1	Analogue Front-end	47
4.2	Digital Front-end	48
4.3	Other Boards	49
4.4	Shielding	49
4.5	Data Generation and Rates	49
	Data Generation	50
	Data Handling Capacity	50
4.6	The SoLid Firmware	51
4.6.1	Buffer	51
4.6.2	Trigger	53
4.6.3	Controls	53
4.6.4	Hardware	54
5	The SoLid Trigger	57
5.1	Trigger Types	57
5.2	Classification Theory	57
5.2.1	Signal Space	57
5.2.2	Discrete Time Domain	58
5.2.3	Data Representation	60
5.2.4	Trigger Formalisation	61
5.3	Trigger Design	63
5.3.1	Metaheuristics	64
5.3.2	Feature Evaluation	65
5.3.3	Feature Extraction Algorithms	67
	Maximum Amplitude	68
	Number-of-Peaks	68
	Weighted Peaks/Number of Photon Avalanches	69
	Time-over-Threshold	70
	Decay Time	70
	Integral-over-Threshold and Integral	71
	Integral-over-Amplitude	71
	Statistical Moments	72
5.3.4	Machine Learning Algorithms	72
	Threshold Function	72
	Perceptron	72
	Feed-Forward Neural Network	73

5.4	Results	74
5.4.1	Test Setup	74
5.4.2	Feature Extraction Algorithms	76
	Tuning	76
	Comparison	76
5.4.3	Machine Learning Algorithms	81
	Correlations	81
	Perceptron	83
	Feed-Forward Neural Network	83
	Triggering	83
5.5	Implementation	86
5.5.1	Resource Usage	86
5.5.2	Power Consumption	89
5.6	Plane-level Trigger	90
6	Conclusion	91
7	References	93
Appendix A		105
A.1	\tilde{U}	105
A.2	Conventions in Section 5	106
A.3	Abbreviations	107
A.3.1	Particles	107
A.3.2	Atoms/Molecules/Materials	107
A.3.3	Physical Quantities	108
A.3.4	Units	108
A.3.5	Unit Pre-fixes	109
A.3.6	Electronics	109
A.3.7	Machine Learning	110
A.3.8	Other	111

List of Figures

2.1	Δm^2 and mixing angle θ favoured or excluded by various neutrino oscillation experiments on different oscillation types. <i>Source:</i> [18].	21
2.2	Feynman diagram of the fundamental level of a β^- -decay producing $\bar{\nu}_e$	22
2.3	Time-development of the composition of the nuclear core during a reactor cycle of a water reactor. Note the different time scales. <i>Source:</i> [49].	23
2.4	$\bar{\nu}_e$ detection spectrum for the ^{235}U isotope. The shape results from folding the emitted spectrum (black dashed-dotted curve), parameterisation and IBD cross section (red dashed curve). <i>Source:</i> [52].	24
2.5	The ratio of observed $\bar{\nu}_e$ events to expected events in case of the new calculations of the three neutrino flavour mixing model (red line) and the case of the existence of a sterile neutrino (blue line). The reactor antineutrino experiments seem to favour the sterile neutrino model. <i>Source:</i> [53].	25
2.6	The ratio of observed $\bar{\nu}_e$ events to expected events for the two GALLEX experiments with the ^{51}Cr source and the SAGE experiment with both ^{51}Cr and ^{37}Ar sources. The error bar shows the 1σ -limit. A deficit up to 20% of the expected rate was observed. <i>Source:</i> [22].	26
2.7	Survival probability for reactor antineutrinos for different sterile neutrino mass splitting factors Δm_{41}^2 as a function of baseline-to-energy ratio L/E . <i>Source:</i> [70] (edited).	30
2.8	Exclusion curves for $\sin^2 2\theta_{12}$ and Δm_{41}^2 for the 3+1 sterile neutrino model for reactor (blue), atmospheric (green) and accelerator (dark blue) experiments and their combined fit (red) at a 99% C.L. <i>Source:</i> [71].	31
2.9	Ratio of observed to expected neutrino rate is shown for different reactor antineutrino experiments. The dashed line represents the three-flavour mixing model, while the solid line corresponds to the 3+1 mode. SoLid will search for sterile neutrinos at a baseline from $L = 5.5 \dots 10\text{m}$ (blue area). <i>Source:</i> [74] (edited).	32
2.10	Comparison of neutrino events expected by simulation (blue) and observed (black dots) by the RENO near detector at a baseline of $L = 293\text{m}$. An excess of $\bar{\nu}_e$ occurs at the region surrounding 5MeV at a level of 3.6σ . <i>Source:</i> [76].	33
2.11	Inverse β -decay e^+ energy spectra of different isotopes at a 150m baseline from a 1GW-reactor (simulation). <i>Source:</i> [78].	34
3.1	The BR2 reactor facility at SCK•CEN in Mol, Belgium. The reactor is shown in yellow and the SoLid detector module is shown in blue. <i>Source:</i> [79] (edited).	35
3.2	A SoLid module placed in the BR2 reactor hall. <i>Source:</i> [81] (edited).	36
3.3	Preliminary calculations of the $\bar{\nu}_e$ energy spectrum of the BR2 reactor. Different colours indicate different measurement periods. <i>Source:</i> [82].	36
3.4	Feynman diagram of Inverse β -decay $\bar{\nu}_e + p \rightarrow e^+ + n$	37
3.5	An array of PVT cubes with $^6\text{LiF} : \text{ZnS}(\text{Ag})$ -layers. The PVT is used for positron capture, while the $^6\text{LiF} : \text{ZnS}(\text{Ag})$ -sheets capture the neutrons. <i>Source:</i> [86].	38
3.6	Three-dimensional rendering of a ten-plane SoLid module. <i>Source:</i> [31].	39

3.7	A PVT cube wrapped in TYVEK sheets as optical shielding and one WLS fibre attached to it. <i>Source:</i> [88].	40
3.8	Feynman diagram of electron-positron annihilation $e^+ + e^- \rightarrow \gamma + \gamma$	40
3.9	Right: Interaction of n and e^+ in the detector cube. Left: Comparison of the signals of n capture (upper) in ${}^6\text{LiF} : \text{ZnS}(\text{Ag})$, and e^+ capture in PVT (lower). <i>Source:</i> [89].	41
3.10	Absorption and emission spectra of the WLS fibre is shown in blue, Photon Detection Efficiency (PDE) of the SiPM is shown in black. <i>Source:</i> [94] [95] (edited).	42
3.11	The SM1 prototype module. <i>Source:</i> [81].	43
3.12	Three-dimensional rendering of the 1.6t-detector, consisting of 50 planes, used in Phase 1. <i>Source:</i> [101].	44
3.13	Three-dimensional rendering of Phase 1-detector placed in a container with surrounding water shielding. <i>Source:</i> [102].	45
3.14	The estimated sensitivity of the SoLid experiment for Phase 1 (blue line) and Phase 2 (black line) to the reactor antineutrino anomaly (RAA) region (blue area) and the Gallium anomaly region (red area) as a function of Δm^2 and $\sin^2 2\theta$. The 95% C.L. are shown. <i>Source:</i> [89].	46
4.1	Three-dimensional rendering of a plane containing the cubes, the frame and the read-out electronics. <i>Source:</i> [31].	47
4.2	Flow of the signal: The SiPM input signal is shaped by the analogue board, then sampled and processed by the digital board before being fed into the online software. The expected data rate at each stage is outlined.	48
4.3	Three-dimensional rendering of a digital front-end board. <i>Source:</i> [31].	49
4.4	The shielding and grounding scheme of the read-out electronics. <i>Source:</i> [31].	50
4.5	Raw data is segmented into defined blocks or time windows, usually consisting of 256 samples. The trigger decides on a block-by-block basis whether data should be read out.	52
4.6	Following a trigger decision on one plane, the trigger can be spread along neighbouring planes.	54
4.7	TRENT module containing the XILINX Artix 7 FPGA. <i>Source:</i> [110].	55
4.8	Block diagram of the firmware. <i>Source:</i> [31] (edited).	56
5.1	(a) Continuous input signal. (b) Signal after time-discretisation (Dirac deltas connected by lines) and quantisation. <i>Source:</i> [116].	59
5.2	Data cube (or tensor) containing signal information. Corresponds to equation 5.16.	61
5.3	In the filter method, the quality of a feature space is evaluated using a score independent from the machine learning algorithm. <i>Source:</i> [124].	64
5.4	In the wrapper method, the quality of a feature space is evaluated using the machine learning algorithm. <i>Source:</i> [124].	65
5.5	Example of categorisation for the Number-of-Peaks feature corresponding to i . The threshold θ_i is shown in green, the values \mathbf{F}_{i} in blue, and the value \mathbf{E}_i on the y -axis. The differently coloured areas mark the four different categories TP , TF , FP and FN	66
5.6	Peak finding algorithm. Green crosses represent found maxima above threshold.	69
5.7	Time-over-Threshold algorithm.	70
5.8	Falling time algorithm. The value is given as the x -axis projection of the green line.	71
5.9	Block diagram of a perceptron.	72

5.10	Block diagram of a feed-forward neural network.	73
5.11	Test setup for taking data of an AmBe source for neutron trigger evaluation.	75
5.12	Evaluation of individual features for the Number-of-Peaks (a), Time-over-Threshold (b), Integral-over-Amplitude (c) and maximum amplitude (d) algorithms on the efficiency-purity plane (each left) and for categorisation (see figure 5.5) (each right). The green cross and green horizontal line indicate the optimum trigger threshold.	77
5.13	Surface plot for Time-over-Threshold feature tuning. Threshold is swept from 0 to 4.5PA with a mountain visible in the range of 0.5PA, indicating the optimum value.	78
5.14	Line plot for Time-over-Threshold feature tuning.	78
5.15	Histograms for the number-of-peak (a) and for the maximum amplitude (b) values on the test data. Neutron signals and photon/dark count signals are clearly distinguishable, in contrast, the maximum amplitude feature values overlap for the most part.	79
5.16	Results for feature evaluation on the purity-efficiency plane.	79
5.17	Results for feature evaluation on the purity-fake rate (false positive rate, fallout) plane. The ROC curve summarising fewer algorithms is shown in figure 6.1.	80
5.18	Two-dimensional histograms indicating correlation for both neutrons and non-neutrons be- tween different features.	82
5.19	Perceptron evaluation.	84
5.20	Two-dimensional parameter sweep for a two-layer two-input (Number-of-Peaks and Time- over-Threshold) feed-forward neural network. No significant improvement in performance is achieved.	85
5.21	Code snipped from the VHDL Number-of-Peaks feature extraction source code.	86
5.22	From the code, an RTL netlist is generated (a) that is then implemented into FPGA (b). . .	87
5.23	Hardware usage of different feature extraction algorithms versus efficiency at a 20% purity level and on a window size of 256 samples. The red line indicates hardware resource availability per channel.	87
5.24	Hardware usage of different feature extraction algorithms versus time window size. The ex- pected window size is 256 samples. The red line indicates hardware availability per channel. .	88
6.1	Summarising ROC curve of different features in terms of efficiency (TPR) and fake rate (fallout, FPR), with the Number-of-Peaks algorithm performing best on the test data set. . .	91

List of Tables

2.1	Overview of properties of leptons. <i>Source</i> : [1] [4].	15
2.2	Properties of neutrinos by source, as orders of magnitude. <i>Source</i> : [18].	19
2.3	Neutrino oscillation parameter fit values, derived from a global fit of current data of neutrino oscillation experiments. *: Parameters are the same for both mass hierarchies. †: For δ_{CP} , the 2σ confidence level is given. <i>Source</i> : [18] [19].	20
2.4	Overview of very short-baseline reactor antineutrino experiments with baseline $L < 10\text{m}$. <i>act.</i> is an abbreviation for <i>mass of active material</i> , P_R denotes reactor power.	20
4.1	Data rates at the different stages of the data acquisition chain per second and per day. Reduction factor is given to the previous stage.	50
4.2	Available resources for the XILINX Artix 7-200T FPGA for the whole device and divided by the 64 read-out channels. <i>Source</i> : [111].	54
5.1	Characteristic values for time-discretisation and quantisation.	60
5.2	Optimum thresholds θ for the Number-of-Peaks and Time-over-Threshold algorithms acquired by parameter sweeps.	76
5.3	Correlation matrix for selected features and the perceptron on both neutrons and non-neutrons. Dark red indicates highest, white lowest correlation ($p = 1$, $p = 0$). <i>ToT</i> : Time-over-Threshold. <i>nPeaks</i> : Number-of-Peaks. <i>weighted</i> : Weighted Number-of-Peaks = Number of Photon Avalanches. <i>maxA</i> : Maximum Amplitude. <i>int/maxA</i> : Integral-over-Amplitude. <i>Perceptr</i> : Perceptron.	81
5.4	Current and power consumption for the trigger algorithms for different number of channels.	89
5.5	Efficiency and purity values on Number-of-Peaks feature for the same threshold value and data set. In this example, by using logical conjunction, a small drop in efficiency is contrasted by a high increase in purity.	89

1 Introduction

The research presented in this dissertation covers two fields, both of vital and substantial interest for particle physics and beyond: Neutrino Physics, and Triggering, or, as an engineer might call it, real-time classification.

Recent discoveries in neutrino physics have not only advanced the knowledge on neutrinos themselves, but have also raised questions on physics beyond the current state of the Standard Model. One of these questions is what SoLid aims to answer: Might there be a fourth type of neutrino, a type not yet observed, and not included within the three flavours of the Standard Model? A type which does not interact weakly with any of the leptons? A type, however, which could give explanation to recently discovered anomalies? Might there be a *sterile* neutrino?

SoLid – short for **S**earch for **o**scillations with a **L**ithium-6 **d**etector – aims to answer these questions by measuring reactor neutrinos at a very short distance from the nuclear core. It employs a novel technique by using solid Lithium-6 as the neutron detector material and provides a high degree of granularity.

However, being located overground in the very close proximity of a reactor core means that a large amount of background signals is faced. In fact, the data produced by background processes exceed the capability of storage and software by several orders of magnitude. It is therefore a crucial task to reduce the data to what are possibly meaningful data. This is achieved by the *trigger*: Signals are classified as either possibly meaningful or not, and sent for further processing only if they are potentially useful.

The decision – or classification – whether or not a set of data can be considered as potentially useful has to be made as data arrive, i.e. in real time. Field-Programmable Gate Arrays (FPGAs), re-configurable digital microelectronics devices, are ideal for the trigger to be implemented onto as they are programmable, fast and cover a wide range of application.

Designing and implementing the trigger is the research topic of the present thesis. This includes the creation of feature extraction algorithms, their evaluation, as well as their implementation on an FPGA.

From the methodological point of view, the decision on the feature is based on the evaluation of the classification performance of each feature in terms of efficiency and fake rate. The implementability into an FPGA in terms of logic resources and power consumption has to be taken into consideration, as these form limiting factors on the algorithm's complexity.

The field of triggering can be considered as essential not only for this particular experiment, but for particle physics in general. As particle physics experiments grow bigger, reach higher resolution and better

sensitivity, their limits are often set by their capability to handle very high data rates, rather than by their sensor technology.

Also looking on a wider level beyond particle physics, triggers – or real-time classifiers – will get more important as well, as data volume is massively increasing by the societal change to a data-driven mode of production.

The dissertation gives an introduction to theoretical and experimental considerations of neutrinos and neutrino oscillations in general, and reactor neutrinos and sterile neutrinos in particular in section 2. Other applications than the search for sterile neutrinos, namely investigation of the 5MeV excess and non-proliferation applications, are discussed in subsection 2.9. Section 3 explains SoLid’s detector technology and its deployment, and the read-out system including firmware is described in section 4. Section 5 – the main part and representing the research carried out by me – discusses methodology, concept, design and implementation of SoLid’s trigger system extensively. A conclusion is made in section 6.

2 Searching for Sterile Neutrinos

After a theoretical overview on neutrinos in and beyond the Standard Model, the methods and history of neutrino oscillation experiments are discussed, with an emphasis on reactor antineutrino experiments. Finally the question is answered: Which anomalies have been observed in these experiments, and for what reason do they suggest the existence of *sterile neutrinos*?

2.1 Neutrinos in the Standard Model

The Standard Model (SM) gives a very accurate description of elementary particles – point-like particles without substructure – and their interactions. The SM divides particles into matter particles that are fermions with half-integer spin $\frac{1}{2}$, and gauge bosons with integer spin 1. SM particles gain mass through the interaction with the Higgs field, whose excitation is the Higgs boson. Fermions are classified into quarks and leptons. Leptons (ℓ) comprise electrons (e^-), muons (μ^-), and taus (τ^-) with charge $Q = -1$, and their corresponding neutrinos (ν_e, ν_μ, ν_τ), with no charge. An overview of the leptons is given on table 2.1. Generally, antiparticles with the same mass, but opposite charges to the respective particles are assumed for all fermions. [1] [2] [3]

Name	Symbol	Mass [MeV c_0^{-2}]	Charge [e]	Weak Isospin
Electron	e^-	$0.510998928 \pm (1.1 \times 10^{-8})$	-1	-1/2
Electron neutrino	ν_e	$\neq 0, < 0.002$	0	+1/2
Muon	μ^-	$105.6583715 \pm (3.5 \times 10^{-6})$	-1	-1/2
Muon neutrino	ν_μ	$\neq 0, < 0.002$	0	+1/2
Tau	τ^-	$1776.82 \pm (0.16)$	-1	-1/2
Tau neutrino	ν_τ	$\neq 0, < 0.002$	0	+1/2

Table 2.1: Overview of properties of leptons. *Source:* [1] [4].

Neutrinos are outstanding particles in many ways: Not only do they have a mass that is a tiny fraction of that of other fermions, they also interact only weakly, coupling solely to the weak bosons (W and Z bosons). Despite the fact that they occur abundantly – as an example, the cosmological neutrino density is $336\nu\text{cm}^{-3}$ [5] – they are elusive: The only fundamental forces neutrinos are prone to are weak interaction and gravitation, which makes them challenging to detect.

There are two types of neutrino interactions: Coupling to a Z^0 boson which leaves their identity unchanged, but changes their 4-momentum, and coupling to a W^\pm boson. The flavour of the neutrino will be the same type as the charged lepton that is connected to the reaction. Negatively charged leptons and

neutrinos have lepton number +1, while positively charged leptons and antineutrinos have lepton number -1 ; all other particles have lepton number 0. At all interactions in the SM, lepton number is conserved.

This should be illustrated by the following example of W decay reactions:

$$W^+ \rightarrow \ell^+ + \nu_\ell \tag{2.1}$$

and

$$W^- \rightarrow \ell^- + \bar{\nu}_\ell, \tag{2.2}$$

with $\ell \in \{e, \mu, \tau\}$. [6]

What is the difference between neutrinos and antineutrinos apart from their mode of production? According to the classical Standard Model, neutrinos have their spin anti-parallel to their momentum, i.e. have negative helicity and are *left-handed*, while antineutrinos have a parallel spin, i.e. have positive helicity and are *right-handed*. [7] [8] This, however, is not entirely correct, as will be discussed in section 2.8.

The Standard Model until recently assumed zero mass for neutrinos, and assumed no neutrino flavour transitions [9]; this has been proven wrong in the not-too-distant past.

2.2 Neutrinos beyond the Standard Model

A remarkable physical phenomenon, originally predicted by Bruno Pontecorvo in 1967 [10], was first confirmed at the SNO [11] and Super-Kamiokande [12] experiments in the early 2000s: neutrino flavour oscillations. As these require non-zero neutrino mass, as opposed to assumptions of the Standard Model, they are considered as going beyond the Standard Model [9].

2.2.1 Mass Mixing

Neutrinos produced in association with a charged lepton do not have a well-defined mass, but are a linear combination of mass eigenstates ν_i :

$$\begin{pmatrix} \nu_e \\ \nu_\mu \\ \nu_\tau \end{pmatrix} = U^* \begin{pmatrix} \nu_1 \\ \nu_2 \\ \nu_3 \end{pmatrix}, \tag{2.3}$$

or

$$|\nu_\ell\rangle = \sum_i U_{\ell i}^* |\nu_i\rangle \tag{2.4}$$

for neutrinos and

$$\begin{pmatrix} \bar{\nu}_e \\ \bar{\nu}_\mu \\ \bar{\nu}_\tau \end{pmatrix} = U \begin{pmatrix} \bar{\nu}_1 \\ \bar{\nu}_2 \\ \bar{\nu}_3 \end{pmatrix}, \quad (2.5)$$

or

$$|\bar{\nu}_\ell\rangle = \sum_i U_{\ell i} |\bar{\nu}_i\rangle \quad (2.6)$$

for antineutrinos, where U is the Pontecorvo–Maki–Nakagawa–Sakata (PMNS) matrix [13]. The PMNS matrix can be seen as analogous for neutrino mixing to the Cabibbo–Kobayashi–Maskawa (CKM) matrix [14] for quark mixing. If neutrinos are their own antiparticles, i.e. Majorana particles, U is commonly expressed in the three-flavour neutrino model as [15]:

$$\begin{aligned} U &= \begin{pmatrix} U_{e1} & U_{e2} & U_{e3} \\ U_{\mu1} & U_{\mu2} & U_{\mu3} \\ U_{\tau1} & U_{\tau2} & U_{\tau3} \end{pmatrix} \\ &= \begin{pmatrix} 1 & 0 & 0 \\ 0 & c_{23} & s_{23} \\ 0 & -s_{23} & c_{23} \end{pmatrix} \begin{pmatrix} c_{13} & 0 & s_{13}e^{-i\delta} \\ 0 & 1 & 0 \\ -s_{13}e^{i\delta} & 0 & c_{13} \end{pmatrix} \begin{pmatrix} c_{12} & s_{12} & 0 \\ -s_{12} & c_{12} & 0 \\ 0 & 0 & 1 \end{pmatrix} \begin{pmatrix} e^{i\alpha_1/2} & 0 & 0 \\ 0 & e^{i\alpha_2/2} & 0 \\ 0 & 0 & 1 \end{pmatrix}, \quad (2.7) \\ &= \begin{pmatrix} c_{12}c_{13} & s_{12}c_{13} & s_{13}e^{-i\delta} \\ -s_{12}c_{23} - c_{12}s_{23}s_{13}e^{i\delta} & c_{12}c_{23} - s_{12}s_{23}s_{13}e^{i\delta} & s_{23}c_{13} \\ s_{12}s_{23} - c_{12}c_{23}s_{13}e^{i\delta} & -c_{12}s_{23} - s_{12}c_{23}s_{13}e^{i\delta} & c_{23}c_{13} \end{pmatrix} \begin{pmatrix} e^{i\alpha_1/2} & 0 & 0 \\ 0 & e^{i\alpha_2/2} & 0 \\ 0 & 0 & 1 \end{pmatrix} \end{aligned}$$

where $c_{ij} = \cos(\theta_{ij})$ and $s_{ij} = \sin(\theta_{ij})$. If neutrinos are Dirac particles, i.e. neutrinos and antineutrinos are different [16], this would simplify to [17]

$$U = \begin{pmatrix} c_{12}c_{13} & s_{12}c_{13} & s_{13}e^{-i\delta} \\ -s_{12}c_{23} - c_{12}s_{23}s_{13}e^{i\delta} & c_{12}c_{23} - s_{12}s_{23}s_{13}e^{i\delta} & s_{23}c_{13} \\ s_{12}s_{23} - c_{12}c_{23}s_{13}e^{i\delta} & -c_{12}s_{23} - s_{12}c_{23}s_{13}e^{i\delta} & c_{23}c_{13} \end{pmatrix}, \quad (2.8)$$

as the matrix containing the phase factors α_1 and α_2 in equation 2.7 can be left out, since the neutrino's left- and right-handed fields are not correlated in this case. The matrix in equation 2.8 is unitary. Whether or not neutrinos are Majorana particles or Dirac fermions is impossible to determine based on past and current experiments [18].

The PMNS matrix can be parameterised using three mixing angles, θ_{12} , θ_{13} and θ_{23} , the CP-violating phase δ_{CP} , and, if neutrinos are Majorana-neutrinos, the phase factors α_1 and α_2 . In addition, parameters for the mass eigenstates are relevant, namely [19]

$$\Delta m^2 = m_3^2 - \frac{m_1^2 + m_2^2}{2}, \quad (2.9)$$

which in case it is positive would indicate a mass hierarchy $m_1 < m_2 < m_3$ and in case it is negative indicates $m_3 < m_1 < m_2$, and the mass splitting factors

$$\Delta m_{ij}^2 = (m_i - m_j)^2. \quad (2.10)$$

Δm_{21} is most often fit for in three-flavour mixing experiments. It is these parameters that neutrino experiments aim to measure. Current data provide evidence that the masses m_1 , m_2 and m_3 are light and different from each other [18].

2.2.2 Neutrino Oscillations

The propagation of neutrinos can be described by

$$|\nu_i(t)\rangle = U_{\ell i}^* e^{-i(E_i t - \vec{p}_i \cdot \vec{x})} |\nu_i(0)\rangle, \quad (2.11)$$

where E_i and \vec{p}_i are the energy and momentum associated with the mass eigenstate i , t denotes time and \vec{x} location. Natural units $c_0 = \hbar = 1$ are used. As neutrinos have very small masses, taking

$$E_i = \sqrt{p_i^2 + m_i^2} \sim p_i + \frac{m_i^2}{2p_i} \sim E + \frac{m_i^2}{2E} \quad (2.12)$$

and equating time t to baseline L (since $v \sim c_0$), equation 2.11 can be approximated by

$$|\nu_i(L)\rangle = U_{\ell i}^* e^{-i \cdot m_i^2 L / 2E} |\nu_i(0)\rangle. \quad (2.13)$$

The probability of flavour transition between two flavour eigenstates α and β then is

$$P(\nu_\alpha \rightarrow \nu_\beta) = |\langle \nu_\beta(L) | \nu_\alpha \rangle|^2 = \left| U_{\alpha i}^* U_{\beta i} e^{-im_i^2 L / 2E} \right|^2, \quad (2.14)$$

also commonly written as [20]

$$\begin{aligned}
P(\nu_\alpha \rightarrow \nu_\beta) = & \delta_{\alpha\beta} - 4 \sum_{i>j} \Re(U_{\alpha i}^* U_{\beta i} U_{\alpha j} U_{\beta j}^*) \sin^2 \left(\frac{\Delta m_{ij}^2 L}{4E} \right) \\
& + 2 \sum_{i>j} \Im(U_{\alpha i}^* U_{\beta i} U_{\alpha j} U_{\beta j}^*) \sin \left(\frac{\Delta m_{ij}^2 L}{2E} \right).
\end{aligned}
\tag{2.15}$$

Applying equation 2.14 to a system of only two neutrino flavours, U in equation 2.8 reduces to a simple rotation matrix

$$U = \begin{pmatrix} \cos \theta & \sin \theta \\ -\sin \theta & \cos \theta \end{pmatrix},
\tag{2.16}$$

leading to the probability function

$$P(\nu_\alpha \rightarrow \nu_\beta) = \sin^2(2\theta) \sin^2 \left(\frac{\Delta m^2 L}{4E} \right).
\tag{2.17}$$

(All equations from or derived from [21], if not indicated otherwise.)

2.3 Neutrino Experiments

Source	Type of ν	E [MeV]	L [m]
Sun	ν_e	10^0	1.5×10^{11}
Atmospheric	$\nu_e, \nu_\mu, \bar{\nu}_e, \bar{\nu}_\mu$	10^3	10^7
Accelerator	$\nu_\mu, \bar{\nu}_\mu$	10^3	$10^3 \dots 10^6$
Reactor	$\bar{\nu}_e$	10^0	$10^1 \dots 10^5$

Table 2.2: Properties of neutrinos by source, as orders of magnitude. *Source:* [18] .

Neutrino experiments can be divided according to neutrino source – emitting neutrinos of different energy scales – and baseline L into *solar*, *atmospheric*, *accelerator* and *reactor* neutrino experiments. The mean energy and baseline of the respective sources are given in table 2.2. When neutrino flavour oscillations exist, given a neutrino of a flavour α produced at the source, the probability to find it in another flavour state β is non-zero, i.e.

$$P(\nu_\alpha \rightarrow \nu_\beta) > 0,
\tag{2.18}$$

which is called the oscillation or transition probability. This implies that the survival probability of flavour α is less than 1, i.e.

$$P(\nu_\alpha \rightarrow \nu_\alpha) < 1.
\tag{2.19}$$

One would therefore observe a *disappearance* of neutrinos of flavour α at the detector, compared to the neutrinos of the same flavour at the source.

Neutrino disappearance has been observed for solar ν_e , reactor $\bar{\nu}_e$ and for atmospheric and accelerator ν_μ on neutrino experiments (e.g. SAGE [22] and GNO [23]), at the KamLAND reactor antineutrino experiment [24], K2K [25] and Super-Kamiokande [12] in the 1990s and 2000s. Following that, the MINOS [26] and T2K [27] experiment found evidence for ν_μ disappearance. $\nu_\mu \rightarrow \nu_\tau$ oscillations have been observed by the Super-Kamiokande [28] and OPERA [29] experiments subsequently. As a result, the existence of neutrino oscillations, implying a non-zero mass of the neutrino, can be considered as proven. The discovery of neutrino oscillations led to Nobel prizes in 2015. [18]

Mass hierarchy	Parameter	Best fit value, 3σ limits
$m_1 < m_2 < m_3$		
*	$\sin^2 \theta_{12}$	$0.297^{0.354}_{0.250}$
	$\sin^2 \theta_{23}$	$0.437^{0.616}_{0.379}$
	$\sin^2 \theta_{13}$	$0.0214^{0.0246}_{0.0185}$
	Δm^2	$(2.50^{2.63}_{2.37} \times 10^{-3})\text{eV}^2$
*	Δm_{21}^2	$(7.37^{7.97}_{6.93} \times 10^{-5})\text{eV}^2$
+	δ_{CP}	$(1.35^{1.99}_{0.92})\pi$
$m_3 < m_1 < m_2$		
*	$\sin^2 \theta_{12}$	$0.297^{0.354}_{0.250}$
	$\sin^2 \theta_{23}$	$0.569^{0.637}_{0.383}$
	$\sin^2 \theta_{13}$	$0.0218^{0.0248}_{0.0186}$
	Δm^2	$-(2.46^{2.60}_{2.33} \times 10^{-3})\text{eV}^2$
*	Δm_{21}^2	$(7.37^{7.97}_{6.93} \times 10^{-5})\text{eV}^2$
+	δ_{CP}	$(1.32^{1.99}_{0.83})\pi$

Table 2.3: Neutrino oscillation parameter fit values, derived from a global fit of current data of neutrino oscillation experiments. *: Parameters are the same for both mass hierarchies. +: For δ_{CP} , the 2σ confidence level is given. Source: [18] [19].

Experiment	Location	L [m]	Scintillator	act. [t]	P_R [MW]	Ref
SoLid	Mol, Belgium	5.5...10	PVT, ^6Li	1.6	40...80	[30] [31]
Nucifer	Saclay, France	7.2	Gd	0.74	67	[32]
POSEIDON	Gatchina, Russia	5	Gd	~ 3	100	[33] [34]
STEREO	Grenoble, France	8.8...11.2	Gd	1.75	57	[35] [34]
NEUTRINO-4	Dimitrovgrad, Russia	6...11	Gd	0.35	16	[36] [37]
Hanaro	Daejeon, Korea	6	Gd	~ 1	30	[38] [34]
DANSS	Tver Oblast, Russia	10...12	Gd	0.9	3000	[39]
PROSPECT	United States	7...20	Gd, ^6Li	11	85	[40]
NuLat	Idaho, United States	3...8	PVT, ^6Li	1	250...1500	[41]

Table 2.4: Overview of very short-baseline reactor antineutrino experiments with baseline $L < 10\text{m}$. *act.* is an abbreviation for *mass of active material*, P_R denotes reactor power.

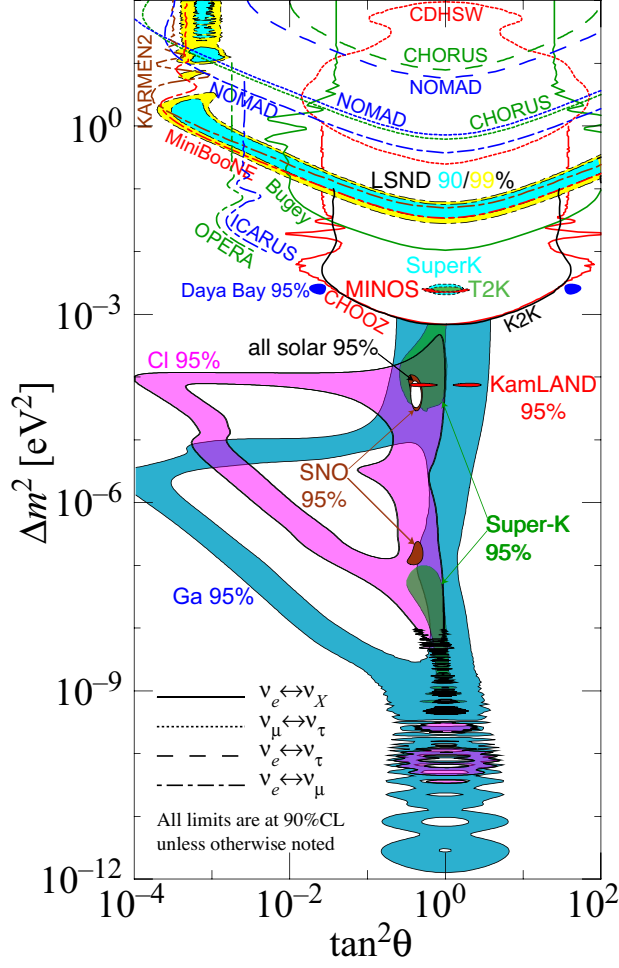


Figure 2.1: Δm^2 and mixing angle θ favoured or excluded by various neutrino oscillation experiments on different oscillation types. *Source:* [18].

Since then, efforts to investigate neutrino oscillations, particularly to determine the parameters described in section 2.2, continue at an intense level. Strong evidence of $\bar{\nu}_e$ disappearance at rather short baselines was reported by several reactor antineutrino experiments: by Double Chooz at $L = 1.1\text{km}$ [42], by Daya Bay at $L = 1.65\text{km}$ [43] and by RENO at $L = 1.38\text{km}$ [44].

As efforts by neutrino experiments looking at all the sources to measure neutrino oscillations are ongoing, parameters are being measured with successively greater accuracy. A summary of parameter fit values as for 2016 combining different experiments is given on table 2.3. A global plot of Δm^2 versus mixing angle θ favoured or excluded by various neutrino oscillation experiments is shown in figure 2.1.

As the three-flavour oscillation non-zero mass neutrino model has replaced the Standard Model's formulation of neutrinos, several anomalies discovered in the recent past in conjunction with reactor antineutrino

experiments support the hypothesis that one or more additional neutrino flavours exist. Several experiments at a short baseline are in construction or have recently obtained data, including SoLid. An overview of experiments with baseline $L < 10\text{m}$ is summarised on table 2.4. Reactor antineutrino emission and the discovered anomalies are discussed in sections 2.4 to 2.7.

2.4 Reactor Antineutrino Emission

Nuclear fission reactors are an intense source of neutrinos [45], emitting them isotropically [46] as products of β^- -decay fission fragments [47].

The most important processes in reactor $\bar{\nu}_e$ production by ^{235}U -fuelled n -induced nuclear fissions are of the type

$$n + {}^{235}\text{U} \rightarrow X_1 + X_2 + 2n + 204\text{MeV}. \quad (2.20)$$

The fragments X_1 and X_2 will undergo several β^- -decays,

$${}^A_Z X \rightarrow {}^A_{Z+1} X' + e^- + \bar{\nu}_e, \quad (2.21)$$

until they have reached a long-lived state, producing an average of $6\bar{\nu}_e$ per fission [6]. The Feynman diagram of the fundamental level of the β^- -decay,

$$n = udd \rightarrow udu + W^- \rightarrow udu + \bar{\nu}_e + e^- = p + \bar{\nu}_e + e^-, \quad (2.22)$$

is shown in figure 2.2. The $\bar{\nu}_e$'s energy is $< 10\text{MeV}$ [48]. Thus, reactor neutrinos are not only produced at a

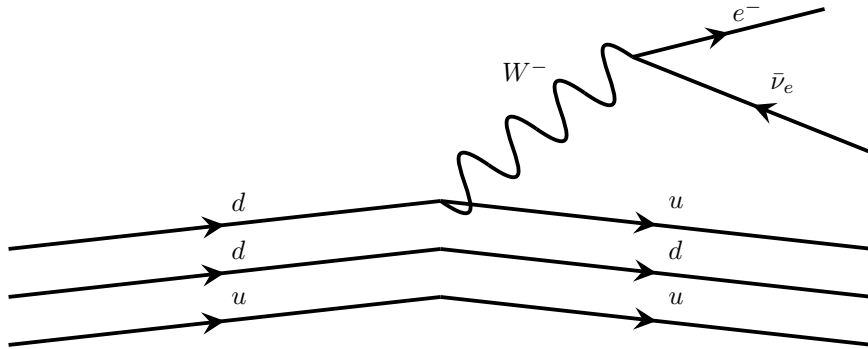


Figure 2.2: Feynman diagram of the fundamental level of a β^- -decay producing $\bar{\nu}_e$.

very high rate, but their energies also lie within a limited spectrum.

The emission energy spectrum of reactor neutrinos depends on the composition of the fissioning actinides:

$$S(E_\nu) = \sum_i f_i \left(\frac{dN_i}{dE_\nu} \right), \quad (2.23)$$

f_i being the number of fissions from actinide i and $\frac{dN_i}{dE_\nu}$ is the cumulative $\bar{\nu}_e$ spectrum of i normalised per fission. Thus, the parameters f_i must be known, requiring detailed information about the reactor core, including the exact composition. The total reactor thermal energy W_{th} is the sum of all the fission actinides' effective thermal energy e_i :

$$W_{th} = \sum_i f_i \cdot e_i. \quad (2.24)$$

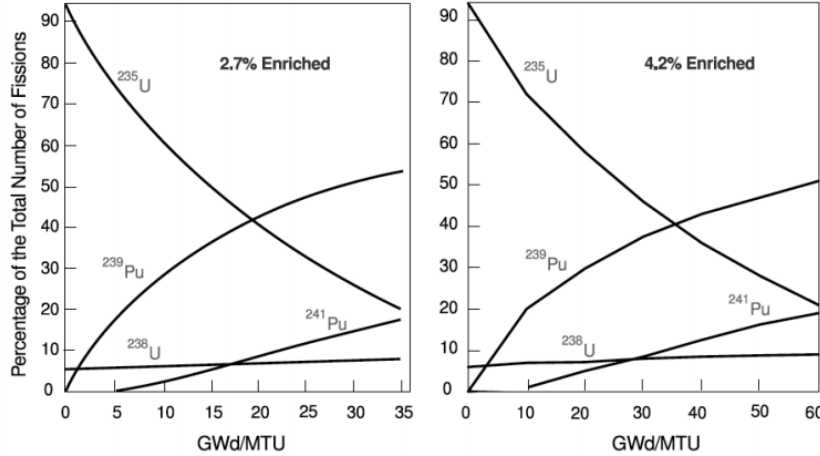


Figure 2.3: Time-development of the composition of the nuclear core during a reactor cycle of a water reactor. Note the different time scales. *Source:* [49].

99.9% of the reactor power stems from the fission of the ^{235}U , ^{238}U , ^{239}Pu and ^{241}Pu isotopes, and only these are considered for $\bar{\nu}_e$ energy spectrum calculations. The thermal energy of the reactor changes with time as the fuel gets burnt up. The time-development of fuel composition during a reactor cycle can be seen in figure 2.3. For practical purposes, f_i is expressed as the fraction of total number of fissions F . [50] So equation 2.23 can be re-written as [51]

$$S(E_\nu) = \frac{W_{th}}{\sum_i \left(\frac{f_i}{F} \right) e_i} \cdot \frac{f_i}{F} \left(\frac{dN_i}{dE_\nu} \right). \quad (2.25)$$

In order to obtain the Inverse β -decay spectrum – or detection spectrum – rather than the emission spectrum, the emission spectrum is folded with the Inverse β -decay cross section [52] (Inverse β -decay is later explained in section 3.2).

The calculations of reactor antineutrino spectra are quite complex in nature as they rely on parameters that are difficult to determine, such as the core composition and the individual emission spectra of the fragments’ energy dissipation, and an inaccurate estimation of these easily propagates to the estimate of total emission spectrum. This leads to final relative uncertainties in the 10% . . . 20% range [52]. As neutrino oscillation experiments rely on an exact estimate of neutrino emission for disappearance measurements (see section 2.2), emission calculations have a direct impact on uncertainty or error of these types of experiments.

2.5 Reactor Anomaly

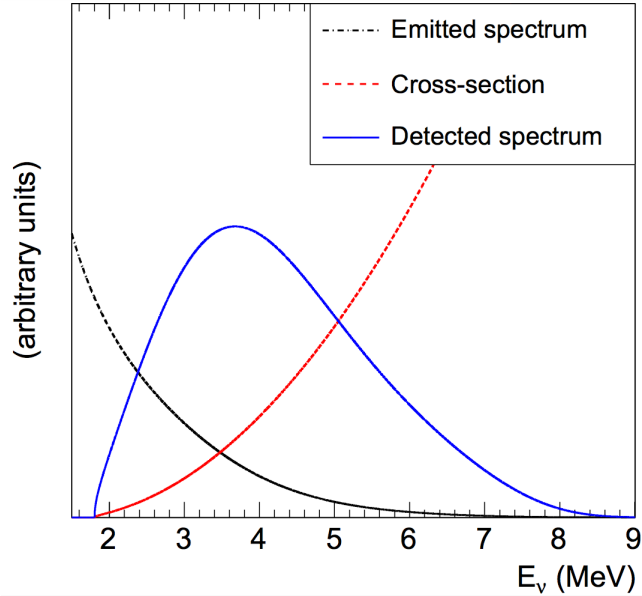


Figure 2.4: $\bar{\nu}_e$ detection spectrum for the ^{235}U isotope. The shape results from folding the emitted spectrum (black dashed-dotted curve), parameterisation and IBD cross section (red dashed curve). *Source:* [52].

A more accurate calculation for ^{235}U and ^{239}Pu antineutrino detection spectra has been performed in 2011 [52] by combining data from nuclear databases and electron energy spectra measured in the 1980s at the ILL reactor facility for the dominant ^{235}U , ^{239}Pu and ^{241}Pu isotopes (see figure 2.4).

These calculations shifted the ratio of predicted to observed $\bar{\nu}_e$ events combining various reactor antineutrino experiments at a baseline $L < 100\text{m}$ from 0.976 ± 0.024 – prediction and observation being consistent

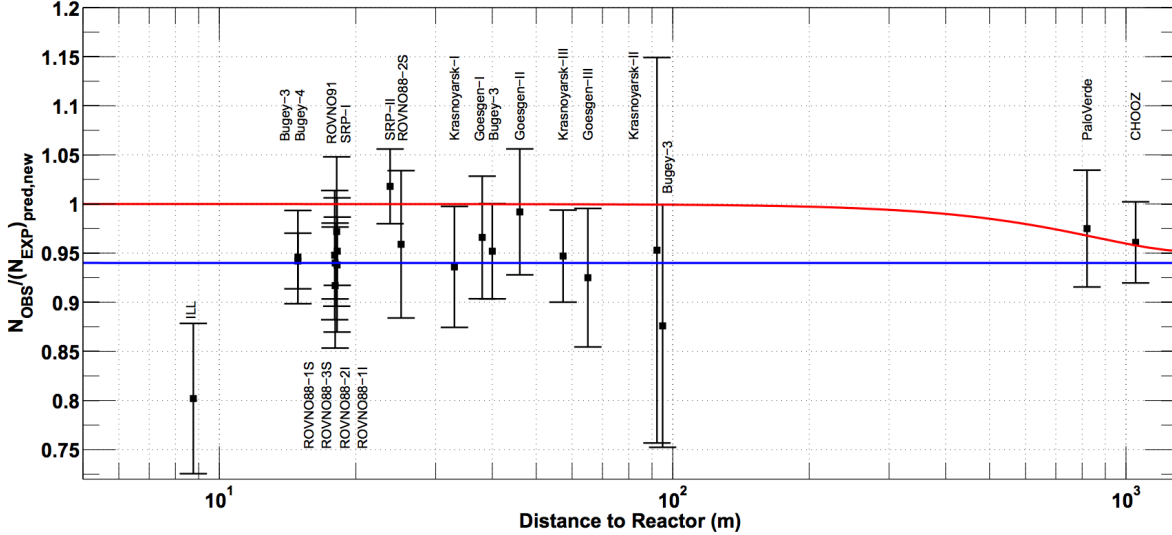


Figure 2.5: The ratio of observed $\bar{\nu}_e$ events to expected events in case of the new calculations of the three neutrino flavour mixing model (red line) and the case of the existence of a sterile neutrino (blue line). The reactor antineutrino experiments seem to favour the sterile neutrino model. *Source:* [53].

in this case – to 0.943 ± 0.023 – leading to a deficit at the 98.6% C.L. This is referred to as the *reactor antineutrino anomaly*. [53]

The deficit favours the existence of at least one additional flavour eigenstate, the sterile flavour ν_s , over the three-flavour mixing model (see figure 2.5). If one additional sterile neutrino is assumed, it would have a new mass eigenstate m_4 with $\Delta m_{41}^2 \sim 1\text{eV}^2$ [54]. The sterile neutrino hypothesis is discussed in section 2.8. A deficit of neutrinos compared to expectation was also observed by the reactor experiments Double Chooz in 2014 [55], RENO in 2015 [56] and Daya Bay in 2016 [57]. Despite the re-calculations of reactor neutrino spectra seeming to favour the sterile neutrino hypothesis, this might be as well be a result of a systematic error, affecting the results of all previous reactor antineutrino experiments simultaneously. Systematic errors cannot be excluded, as currently unknown, unconsidered or underestimated effect might have led to an incorrect estimation of the predicted reactor detection spectrum. However, an unknown background is unlikely to be the explanation, as the measured deficit is time-independent and correlated to reactor power [18].

2.6 Gallium Anomaly

A second observation supporting the sterile neutrino hypothesis is the *Gallium anomaly*. The GALLEX and SAGE detectors have been tested with intense ^{51}Cr and ^{37}Ar sources placed inside the detectors. Ratios R

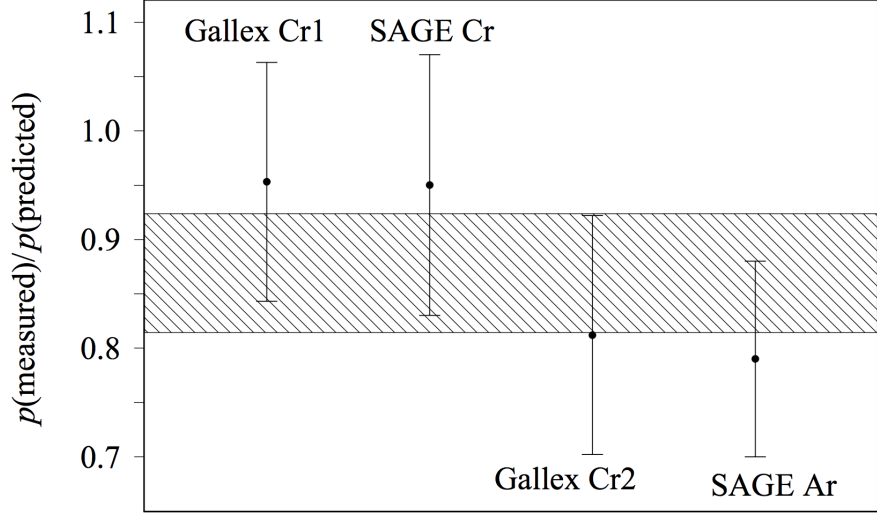


Figure 2.6: The ratio of observed $\bar{\nu}_e$ events to expected events for the two GALLEX experiments with the ^{51}Cr source and the SAGE experiment with both ^{51}Cr and ^{37}Ar sources. The error bar shows the 1σ -limit. A deficit up to 20% of the expected rate was observed. *Source:* [22].

of expected to observed ν_e events,

$$\begin{aligned}
 R_{\text{GALLEX-1}, ^{51}\text{Cr}} &= 0.953 \pm 0.11, \\
 R_{\text{GALLEX-2}, ^{51}\text{Cr}} &= 0.812^{+0.10}_{-0.11}, \\
 R_{\text{SAGE}, ^{51}\text{Cr}} &= 0.95 \pm 0.12, \\
 R_{\text{SAGE}, ^{37}\text{Ar}} &= 0.791^{+0.084}_{-0.078},
 \end{aligned}
 \tag{2.26}$$

subscripts denoting detector and source, have been measured; the quoted uncertainties are at the 1σ level. A clear deficit of neutrinos up to 20% of the expected number of events was observed (see figure 2.6). [22] [58]

However, these numbers do not take into account cross section uncertainty.

Both GALLEX and SAGE use the reaction



for detection, a reaction whose cross section has a large uncertainty [59]. Re-calculation with consideration of the cross section uncertainty modified the results and the 1σ level to new ratios of

$$\begin{aligned}
R_{\text{GALLEX-1}, {}^{51}\text{Cr}} &= 0.84_{-0.12}^{+0.13}, \\
R_{\text{GALLEX-2}, {}^{51}\text{Cr}} &= 0.71_{-0.11}^{+0.12}, \\
R_{\text{SAGE}, {}^{51}\text{Cr}} &= 0.84_{-0.13}^{+0.14}, \\
R_{\text{SAGE}, {}^{37}\text{Ar}} &= 0.70_{-0.09}^{+0.10}.
\end{aligned}
\tag{2.28}$$

These have slightly higher uncertainty, but significant lower result values have been obtained, leading to the confirmation of the Gallium anomaly at the 3.0σ level. [59] Combined analysis of the Gallium anomaly experiments and the reactor anomaly experiment disfavour the standard three-flavour mixing model even at a C.L. of 99.9%, or 3.3σ [60].

2.7 Accelerator Anomaly

The *accelerator anomaly*, or *LSND anomaly*, stems from measurements at the LSND accelerator neutrino experiment in Los Alamos [61] that observed $\bar{\nu}_e$ in a $\bar{\nu}_\mu$ -beam at a baseline of $L = 30\text{m}$. LSND measured an excess of neutrinos which would be consistent with the existence of a sterile neutrino with $\Delta m_{41}^2 \sim 1\text{eV}^2$. Further support of this excess was given by MiniBooNE at Fermilab at the 2.8σ level [62]. However, the KARMEN experiment could not reproduce the excess, despite having measured a similar phase space to LSND [63]. In addition, other accelerator neutrino experiments also disfavour the sterile neutrino hypothesis, such as CDHSW [64], MINOS [65], OPERA [66] and ICARUS [67]. However, not all regions of the relevant parameter space have been measured by these experiments [41].

In conclusion, the high confidence put on the sterile neutrino hypothesis by reactor experiments was not reproduced by accelerator neutrino experiments.

2.8 The Sterile Neutrino Hypothesis

As neutrinos have non-zero mass, they are a superposition of negative and positive chirality states. Only the negative chirality component interacts weakly. For neutrinos, the negative chirality state corresponds essentially exclusively to negative helicity, and for antineutrinos to positive helicity (with a small correction, that would vanish in the limit of zero neutrino mass). Neutrinos therefore interact essentially always as helicity left-handed particles, and anti-neutrinos as helicity right-handed particles.

There is no evidence so far that predominantly right-handed neutrinos or predominantly left-handed antineutrinos exist, nevertheless, if they exist, they should be *sterile* neutrinos, not coupling neither to W^\pm nor to Z^0 bosons, as obtained experimental data is compatible only with 3 flavour neutrinos that are coupled to the Z boson [68]. They could contribute significantly to open fundamental questions in physics such as the generation of the observed matter-antimatter asymmetry, the generation of neutrino masses and their disparity. [18]

2.8.1 Sterile Neutrino Mass Mixing

The sterile neutrino hypothesis suggests one or more additional neutrinos to the three active flavour neutrinos which are already known (ν_e, ν_μ, ν_τ), and is called the $3+n$ model depending on the number n of how many new flavour eigenstates are suggested. These n new *sterile* flavours would correspond to n corresponding additional mass eigenstates. [18] Taking the case of the $3+1$ model, i.e. of the model suggesting one additional sterile neutrino, the mass mixing equations 2.3 and 2.4 would be expressed as

$$\begin{pmatrix} \nu_e \\ \nu_\mu \\ \nu_\tau \\ \nu_s \end{pmatrix} = U^* \begin{pmatrix} \nu_1 \\ \nu_2 \\ \nu_3 \\ \nu_4 \end{pmatrix}, \quad (2.29)$$

with ν_s denoting the suggested sterile neutrino, increasing the number of linearly independent mass splitting factors Δm_{ij} from 3 to 4. In case of more than one sterile neutrino, the equation would simply contain more vector elements for the additional neutrino states. For n additional sterile neutrinos, the dimensionality of the PMNS matrix (equation 2.7 and 2.8) together with the number of mass splittings would also have to increase by n , thus the 3×3 matrix for the three-flavour model would become a 4×4 matrix together with 4 mass splitting factors in the $3+1$ model and to a 5×5 matrix with 5 mass splitting factors in the $3+2$

model [69]. In the 3+1 model, the new 4×4 mixing matrix \tilde{U} is expressed as

$$\begin{aligned}
\tilde{U} &= \begin{pmatrix} c_{14} & 0 & 0 & s_{14} \\ -s_{14}s_{24} & c_{24} & 0 & c_{14}s_{24} \\ -c_{24}s_{14}s_{34} & -s_{24}s_{34} & c_{34} & c_{14}c_{24}s_{34} \\ -c_{24}c_{34}s_{14} & -s_{24}c_{34} & -s_{34} & c_{14}c_{24}c_{34} \end{pmatrix} \begin{pmatrix} U_{e1} & U_{e2} & U_{e3} & 0 \\ U_{\mu1} & U_{\mu2} & U_{\mu3} & 0 \\ U_{\tau1} & U_{\tau2} & U_{\tau3} & 0 \\ 0 & 0 & 0 & 1 \end{pmatrix} \\
&= \begin{pmatrix} c_{14}U_{e1} & c_{14}U_{e2} & c_{14}U_{e3} & s_{14} \\ \cdots & \cdots & \cdots & c_{14}s_{24} \\ \cdots & \cdots & \cdots & c_{14}c_{24}s_{34} \\ \cdots & \cdots & \cdots & c_{14}c_{24}c_{34} \end{pmatrix} \\
&= \begin{pmatrix} \tilde{U}_{e1} & \tilde{U}_{e2} & \tilde{U}_{e3} & \tilde{U}_{e4} \\ \tilde{U}_{\mu1} & \cdots & \cdots & \cdots \\ \tilde{U}_{\tau1} & \cdots & \cdots & \cdots \\ \tilde{U}_{s1} & \cdots & \cdots & \cdots \end{pmatrix}.
\end{aligned} \tag{2.30}$$

A written-out representation of \tilde{U} is given in the appendix in equation A.1. The elements of the 3×3 PMNS matrix $U_{\alpha i}$ from equation 2.7 are included in this parameterisation. The CP phases are omitted as they do not affect survival probability for reactor neutrino oscillation. [70]

The sterile neutrino is called *sterile* as – unlike the confirmed 3 flavour eigenstates – it does not couple to the W^\pm nor to the Z^0 boson, thus does not interact weakly [6]. Not to mention, that – as for any other neutrino – it neither does have charge nor colour, hence it is only affected by the gravitational force. Therefore oscillations into the sterile neutrino state would simply lead to disappearance of neutrinos in observations. The additional disappearance caused by the existence of sterile neutrinos would be able to explain the measured neutrino deficit of the reactor and Gallium anomaly.

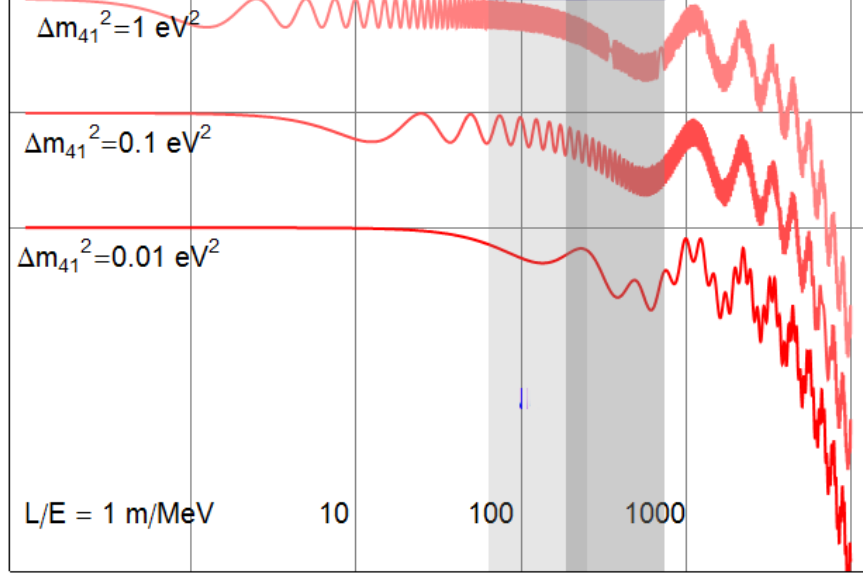


Figure 2.7: Survival probability for reactor antineutrinos for different sterile neutrino mass splitting factors Δm_{41}^2 as a function of baseline-to-energy ratio L/E . *Source:* [70] (edited).

2.8.2 Sterile Neutrino Oscillations

In the case of the 3+1 model, equation 2.15 applied to the case $\bar{\nu}_e \rightarrow \bar{\nu}_e$, where it becomes the survival probability of reactor antineutrinos, will become [70]

$$\begin{aligned}
 P(\bar{\nu}_e \rightarrow \bar{\nu}_e) &= \left| \sum_{j=1}^4 |\tilde{U}_{ej}|^2 \exp i \frac{\Delta m_{j1}^2 L}{2E_\nu} \right|^2 \\
 &= 1 - \sum_{i < j} 4 |\tilde{U}_{ei}|^2 |\tilde{U}_{ej}|^2 \sin^2 \left(\frac{\Delta m_{ij}^2 L}{4E_\nu} \right),
 \end{aligned} \tag{2.31}$$

approximated by [70]

$$\begin{aligned}
 P(\bar{\nu}_e \rightarrow \bar{\nu}_e) &= 1 - c_{14}^4 c_{13}^4 \sin^2 2\theta_{12} \sin^2 \left(\Delta m_{21}^2 \frac{L}{E} \right) \\
 &\quad - c_{14}^4 \sin^2 2\theta_{13} \sin^2 \left(\Delta m_{31}^2 \frac{L}{E} \right) \\
 &\quad - \sin^2 2\theta_{14} \sin^2 \left(\Delta m_{41}^2 \frac{L}{E} \right).
 \end{aligned} \tag{2.32}$$

The reactor antineutrino survival probability is plotted in figure 2.7 for sterile neutrino mass splitting factors $\Delta m_{41} = 0.01\text{eV}^2, 0.1\text{eV}^2, 1\text{eV}^2$ as a function of baseline-to-energy ratio L/E . As can be seen, sterile neutrinos of the range of $\Delta m_{41}^2 \sim 1\text{eV}$ would agree with the deficit of neutrinos in the reactor antineutrino anomaly. Indeed, in the 3+1 and 3+2 models that are commonly considered [18], the discussed anomalies

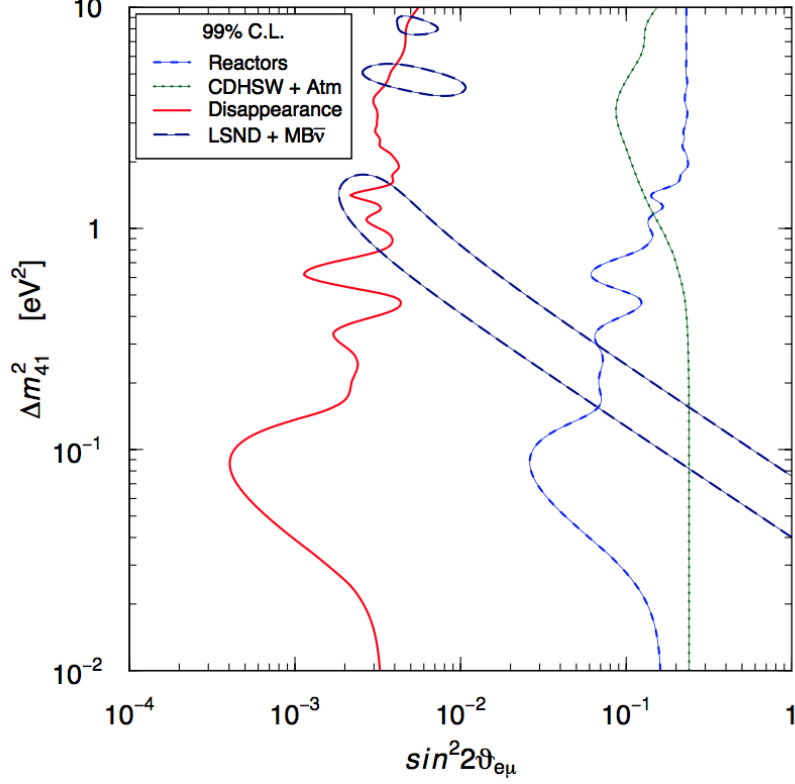


Figure 2.8: Exclusion curves for $\sin^2 2\theta_{12}$ and Δm_{41}^2 for the 3+1 sterile neutrino model for reactor (blue), atmospheric (green) and accelerator (dark blue) experiments and their combined fit (red) at a 99% C.L. *Source:* [71].

would be consistent with fits to $\Delta m_{41}^2 \sim 1\text{eV}^2$ in the 3+1 model or $\Delta m_{41}^2, \Delta m_{51}^2 \sim 1\text{eV}^2$ in the 3+2 model (see figure 2.8) [54].

Experimental data suggest that the mass splittings Δm_{21}^2 ($\mathcal{O}(10^{-5})\text{eV}^2$) and Δm_{31}^2 ($\mathcal{O}(10^{-3})\text{eV}^2$) are very small compared to Δm_{41}^2 (or Δm_{51}^2) $\sim 1\text{eV}^2$. In the short-baseline range, $\nu_\alpha \rightarrow \nu_s$ oscillations would be dominant to the level where oscillations between the three standard neutrinos are negligible, with these neutrinos becoming more dominant as baseline increases. Therefore Δm_{21} and Δm_{31} can be set to 0, or to *degenerate* state, for approximation in the short-baseline range in the sterile neutrino models. In the case of the 3+1, equation 2.32 can be approximated for very short-baseline reactor antineutrino experiments such as SoLid by [72] [73]:

$$P(\nu_\alpha \rightarrow \nu_\beta) = \delta_{\alpha\beta} - 4(\delta_{\alpha\beta} - U_{\alpha 4} U_{\beta 4}^*) U_{\alpha 4}^* U_{\beta 4} \sin^2 \left(\frac{\Delta m_{41}^2 L}{4E} \right) \quad (2.33)$$

for any oscillation $\nu_\alpha \rightarrow \nu_\beta$ which is in the particular case of $\bar{\nu}_e \rightarrow \bar{\nu}_e$ survival probability would become

$$P(\bar{\nu}_e \rightarrow \bar{\nu}_e) = 1 - \sin^2 2\theta_{14} \sin^2 \left(\Delta m_{41}^2 \frac{L}{E} \right), \quad (2.34)$$

the function that will be used for fitting the sterile neutrino parameters θ_{14} and Δm_{41}^2 in short-baseline reactor antineutrino experiments. SoLid will measure these neutrino oscillation parameters at a well-defined range from $L = 5.5\text{m}$ to $L = 10\text{m}$, as shown in figure 2.9, currently uncovered by reactor antineutrino experiments.

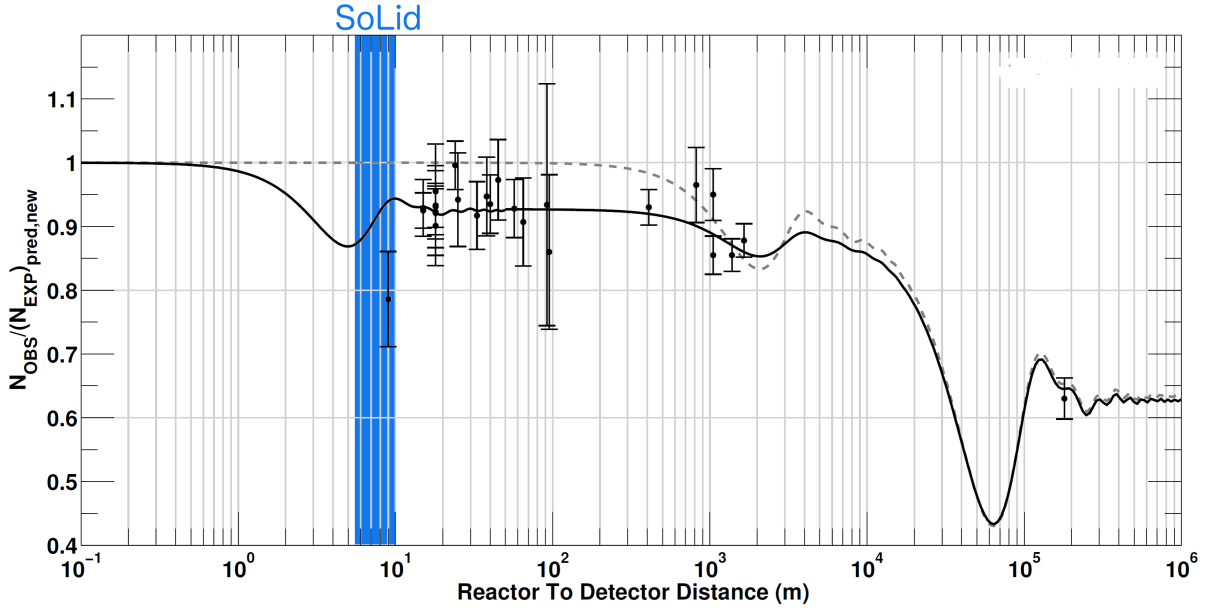


Figure 2.9: Ratio of observed to expected neutrino rate is shown for different reactor antineutrino experiments. The dashed line represents the three-flavour mixing model, while the solid line corresponds to the 3+1 mode. SoLid will search for sterile neutrinos at a baseline from $L = 5.5 \dots 10\text{m}$ (blue area). *Source:* [74] (edited).

2.9 Other Applications of SoLid

Although the hunt for sterile neutrinos is what SoLid mainly aims for, SoLid also allows the investigation of the 5MeV excess, and its technology might be used for reactor monitoring for nuclear non-proliferation applications.

2.9.1 5MeV Excess

The precise measurement of reactor antineutrino flux of ^{235}U -based reactors is also of interest due to an anomaly recently discovered by reactor antineutrino experiments: A discrepancy, or excess, at the region of about 5MeV has been discovered by Double Chooz in 2011 [42] and Daya Bay in 2012 [75], and later confirmed at a 3.6σ level by RENO in 2015 (see figure 2.10) [76].

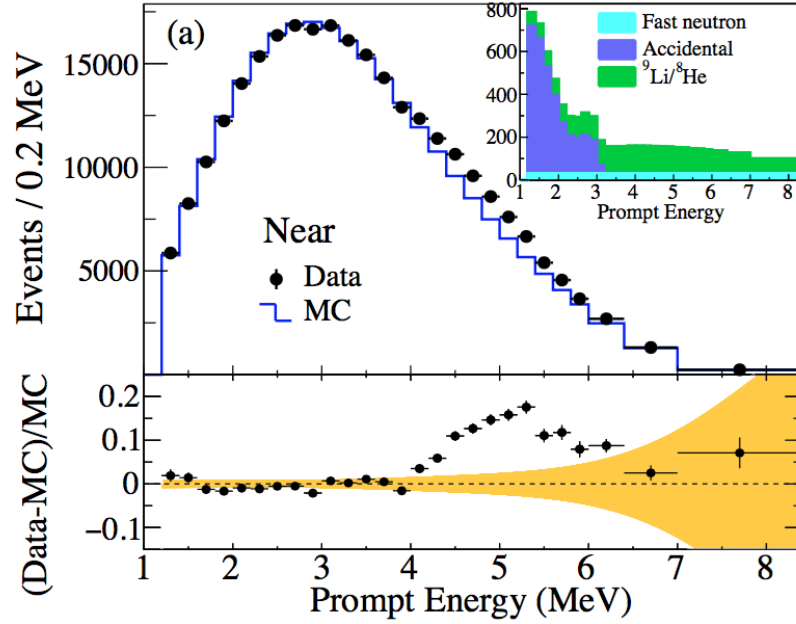


Figure 2.10: Comparison of neutrino events expected by simulation (blue) and observed (black dots) by the RENO near detector at a baseline of $L = 293\text{m}$. An excess of $\bar{\nu}_e$ occurs at the region surrounding 5MeV at a level of 3.6σ . *Source:* [76].

The discrepancy at 5MeV is not understood yet. Possible causes of the excess might be unaccounted background of the reactor flux, or even effects due to new physics [41].

Double Chooz is located at a baseline of $L = 1.1\text{km}$ from the reactor, Daya Bay at a baseline of $L = 1.64\text{km}$ and RENO at $L = 1.38\text{km}$ for the far detector and $L = 294\text{m}$ for the near detector [56] (see section 2.3). Hence, the baseline range of $L < 290\text{m}$ is uncovered so far. SoLid, along with other very short-baseline reactor antineutrino experiments, will provide evidence whether the 5MeV excess can be reproduced at the very near distance from the reactor.

2.9.2 Non-Proliferation

SoLid is a particle physics experiment aiming at the search on sterile neutrinos. However, despite not being a main target of the experiment, the SoLid detector also could explore potential applications of its technology in nuclear non-proliferation.

Monitoring the Pu content of nuclear reactors forms an essential measure in non-proliferation efforts. Usually, γ -ray spectroscopy is applied for this purpose, however short-baseline $\bar{\nu}_e$ flux monitoring has been suggested in the past with increasing recent interest as an appropriate tool of cross-validation in determining the composition of nuclear fuel [40] [51].

Reactors emit a characteristic $\bar{\nu}_e$ flux and energy spectrum according to their thermal power and to the isotopic composition of their fuel, namely ^{235}U , ^{238}U , ^{239}Pu and ^{241}Pu (see figure 2.11) [77]. This allows detection of Pu content in nuclear reactors by obtaining their $\bar{\nu}_e$ spectrum and flux. Because of the high penetration depth of neutrinos, it is possible to perform the measurements remotely. [78]

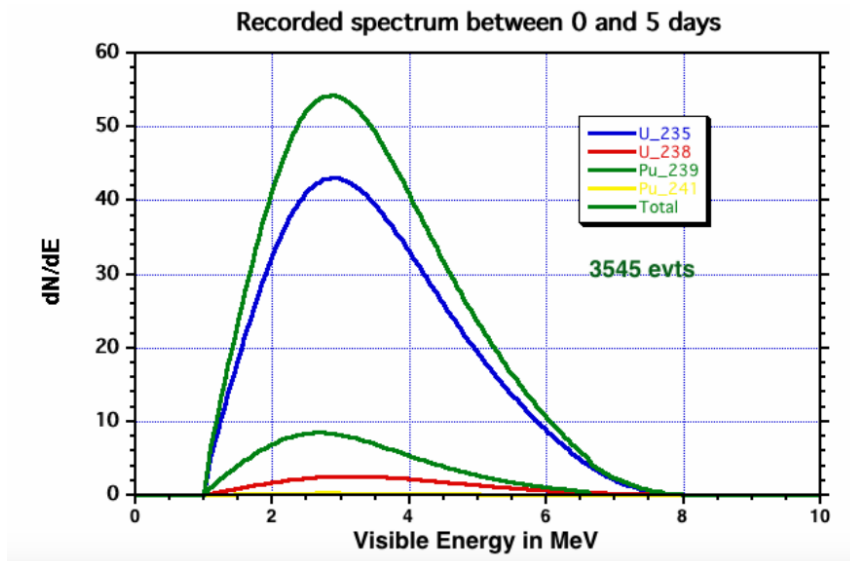


Figure 2.11: Inverse β -decay e^+ energy spectra of different isotopes at a 150m baseline from a 1GW-reactor (simulation). *Source:* [78].

Due to the compactness of the technology used for SoLid, as well as its usage of solid material (PVT and $^6\text{LiF} : \text{ZnS}(\text{Ag})$), SoLid's novel neutrino detection technology is a potential candidate for employment in non-proliferation monitoring applications.

3 The SoLid Detector

The SoLid detector is unique not only in terms of its very short baseline to the reactor core, but also in terms of the employed scintillators – Polyvinyl toluene (PVT) and ${}^6\text{LiF} : \text{ZnS}(\text{Ag})$ – and in providing a high level of segmentation and granularity of the detector modules.

3.1 BR2 Reactor

SoLid’s neutrino source is the BR2 nuclear fission reactor located at the Belgian nuclear research facility SCK•CEN in Mol. BR2 is designed and operated as a tank-type material research reactor, with a power range up to 100MW [79]. A picture of BR2’s architecture can be seen in figure 3.1.

Its core measures only 50cm in diameter [80], which makes it an almost point-like $\bar{\nu}_e$ source. The architecture allows the SoLid detector modules to be placed at a very short distance of 5.5...10m from the reactor core, as shown in figure 3.2. SoLid is intended to be the only experiment running at BR2, contributing to the stability of background conditions as other experiments might contribute to spallation neutron background [81].

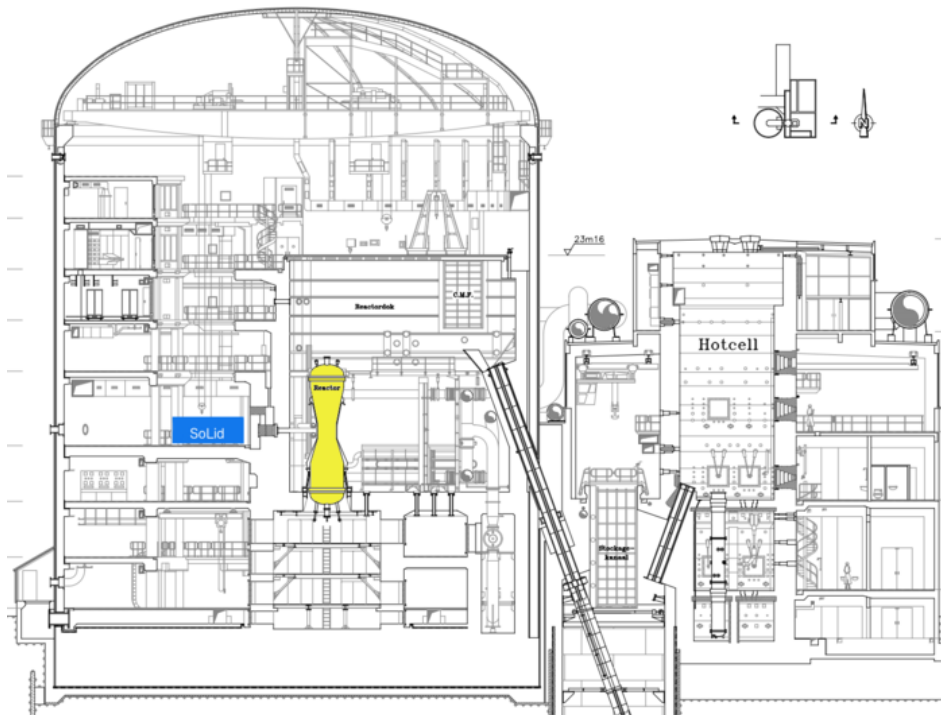


Figure 3.1: The BR2 reactor facility at SCK•CEN in Mol, Belgium. The reactor is shown in yellow and the SoLid detector module is shown in blue. *Source:* [79] (edited).

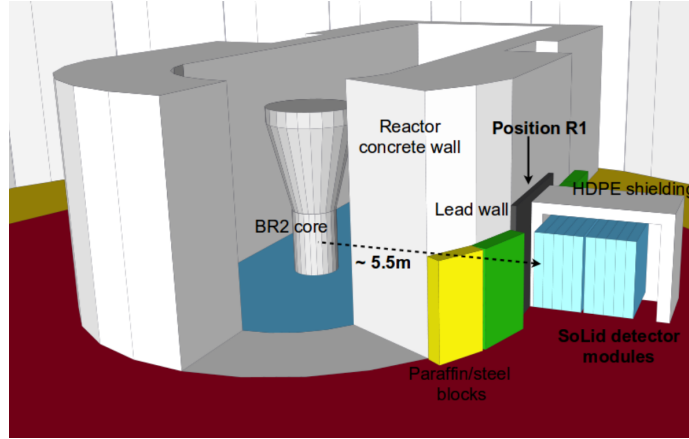


Figure 3.2: A SoLid module placed in the BR2 reactor hall. *Source:* [81] (edited).

BR2 is operated with ^{235}U as fuel, usually in cycles of three to four weeks [73] at 40...80MW thermal power [80].

A very intense neutrino flux of $\sim 10^{10}\bar{\nu}_e\text{s}^{-1}$ is expected [80] with the $\bar{\nu}_e$ energy spectrum peaking at $\sim 1\text{MeV}$ and ranging to $\sim 6\text{MeV}$, as shown in figure 3.3 [82].

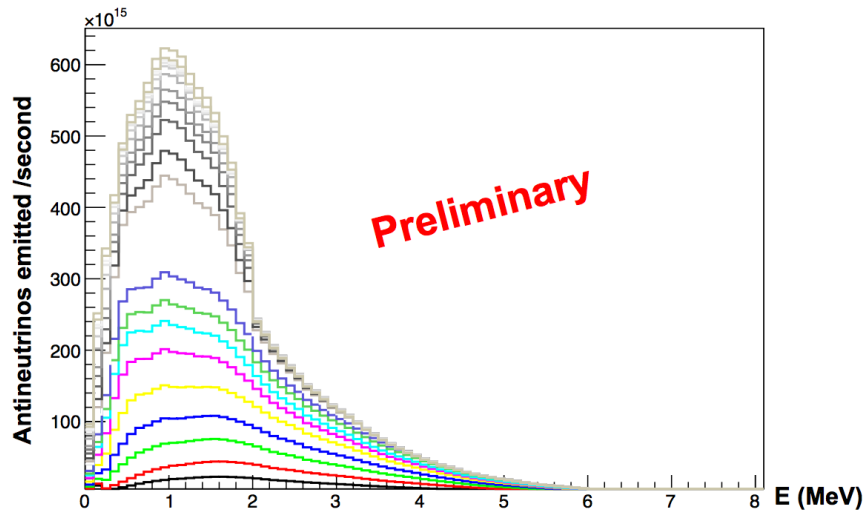


Figure 3.3: Preliminary calculations of the $\bar{\nu}_e$ energy spectrum of the BR2 reactor. Different colours indicate different measurement periods. *Source:* [82].

3.2 IBD Capture

Reactor neutrino detection is based on Inverse β -Decay (IBD),

$$\bar{\nu}_e + p \rightarrow e^+ + n, \quad (3.1)$$

with an energy threshold of 1.8MeV [83]. Equation 3.1 refers to the same process as

$$\bar{\nu}_e + udu \rightarrow W^+ + \bar{\nu}_e + udd \rightarrow e^+ + udd \quad (3.2)$$

shown in figure 3.4, the quark triplet udu equating to a p , and the triplet udd equating to a n . It has a well-known cross section of [84] [85]

$$\sigma_{\text{IBD}} = 0.952 \left(\frac{E_e p_e}{1\text{MeV}^2} \right) \times 10^{-43} \text{cm}^2. \quad (3.3)$$

The products of the IBD process are a positron (e^+) and a neutron (n). These product are easily detectable. At SoLid, the products are measured using two different scintillating materials for conversion into visible photons: Polyvinyl toluene – or PVT – for e^+ capture and Lithium-6 Silver-doped Zinc Sulphide (${}^6\text{LiF} : \text{ZnS}(\text{Ag})$) layers for n capture.

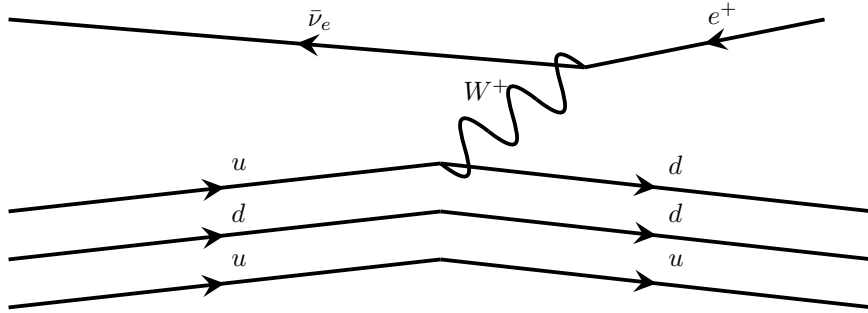


Figure 3.4: Feynman diagram of Inverse β -decay $\bar{\nu}_e + p \rightarrow e^+ + n$.

3.2.1 Detector Components

The SoLid module is built out of 10 planes, which each contain 256 cubes containing the scintillation materials. The scintillators capture the IBD products and convert them into light to be guided to the photon sensors. A sketch of a full detector module is shown in figure 3.6.

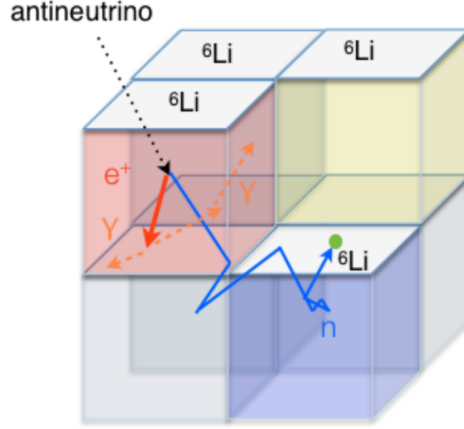


Figure 3.5: An array of PVT cubes with ${}^6\text{LiF} : \text{ZnS}(\text{Ag})$ -layers. The PVT is used for positron capture, while the ${}^6\text{LiF} : \text{ZnS}(\text{Ag})$ -sheets capture the neutrons. *Source:* [86].

The Cube consists of PVT and measures $5\text{cm} \times 5\text{cm} \times 5\text{cm}$. A layer of ${}^6\text{LiF} : \text{ZnS}(\text{Ag})$ is attached to one side of the cube. Several cubes are arranged discretely as an array (see figure 3.5). Each cube contains four grooves for placement of Wavelength-Shifting (WLS) fibres which guide the light to the photosensors. The single cubes are optically shielded from each other by being wrapped in TYVEK paper. [87] The assembly of a cube with one WLS fibre can be seen in figure 3.7.

The Plane consists of 256 cubes, arranged as a 16×16 array, with the photosensors being placed at the frame and the read-out electronic modules being attached at one side. Since two Wavelength-Shifting Fibres cross each row both in the horizontal and the vertical direction, 64 photosensors are used per plane, also meaning that the electronics board is designed to read out 64 channels.

The Module which can be seen in figure 3.6 is built upon 10 planes. The modules are independent of each other mechanically as well as in terms of power supply, clock and control distribution, heat-exchanger and cooling-air blower, which means they can be operated separately for commissioning [31].

3.2.2 Positron Capture

PVT is used as the scintillator material which catches the positron. The positron is absorbed within $\mathcal{O}(10^{-8})\text{s}$ by the PVT and is emitted as a short ($\mathcal{O}(10^{-7})\text{s}$), intense light pulse [81] [89]. Thereafter, the positron annihilates with an electron coming from the detector via the process

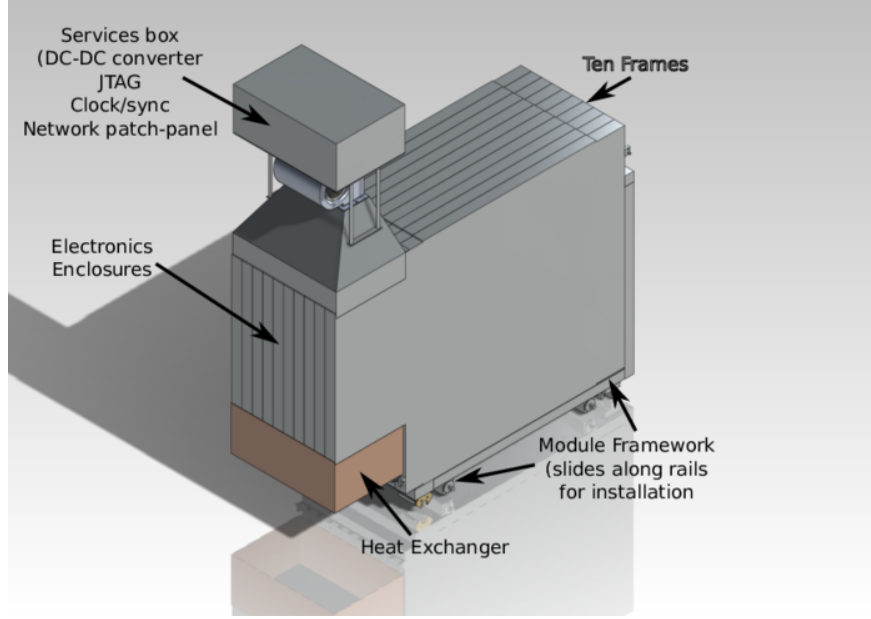


Figure 3.6: Three-dimensional rendering of a ten-plane SoLid module. *Source:* [31].

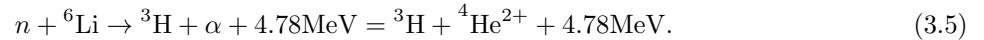
$$e^+ + e^- \rightarrow \gamma + \gamma \quad (3.4)$$

as depicted in figure 3.8. The γ s each have an energy of 511keV [87].

The light pulse is captured by the SiPMs. The total energy deposited in the cube can be used to reconstruct the $\bar{\nu}_e$ energy, when correcting for the small fraction of annihilation γ energy on average deposited in the interaction cube [89].

3.2.3 Neutron Capture

Whilst positrons are captured by the PVT scintillator, neutrons are caught by the ${}^6\text{LiF} : \text{ZnS}(\text{Ag})$ sheets. And while positrons cause a prompt response from the scintillator, neutrons do not; they undergo thermalisation while being scattered through the material before they are captured by ${}^6\text{Li}$ via the process



Both ${}^3\text{H}$ and the α -particle ($= {}^4\text{He}^{2+}$) contain sufficient energy to excite the electrons in the ZnS crystals. Scintillation light is emitted by de-excitation of these electrons over a longer period of $\mathcal{O}(10^{-6})$ s, thus one order of magnitude higher than the positron light pulse – this leads to a shape for the neutron light emission

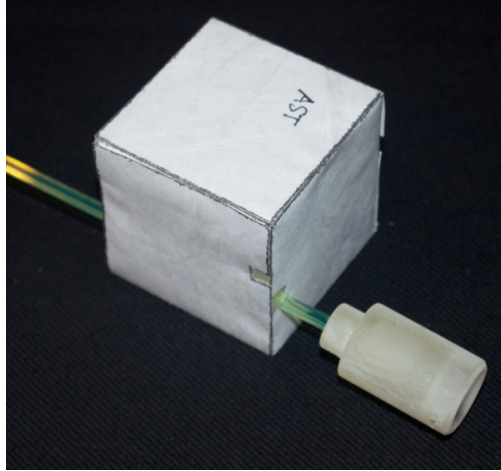


Figure 3.7: A PVT cube wrapped in TYVEK sheets as optical shielding and one WLS fibre attached to it. *Source:* [88].

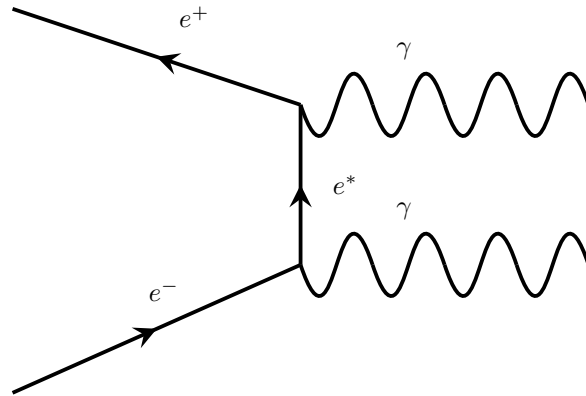


Figure 3.8: Feynman diagram of electron-positron annihilation $e^+ + e^- \rightarrow \gamma + \gamma$.

which is distinct from the short, high-amplitude pulse generated by positron scintillation. The neutron ${}^6\text{LiF} : \text{ZnS}(\text{Ag})$ scintillation is delayed by $\mathcal{O}(10^{-4})$ s when compared to the prompt response of the PVT scintillator to the positron. The difference of n and e^+ signal is shown in figure 3.9, with a sketch of the underlying interaction within the cube. [88] [89] [90]

3.2.4 Light Capture

Wavelength-Shifting Fibres collect and convert the light signals produced by n and e^+ capture within the cubes in order to transport them to the photosensors [91]. They absorb photons at a given wavelength and subsequently emit them isotropically at a longer wavelength, thus at a lower energy (see figure 3.10). The purpose of using WLS fibre is to randomise the direction of the emitted light, in order that a fraction

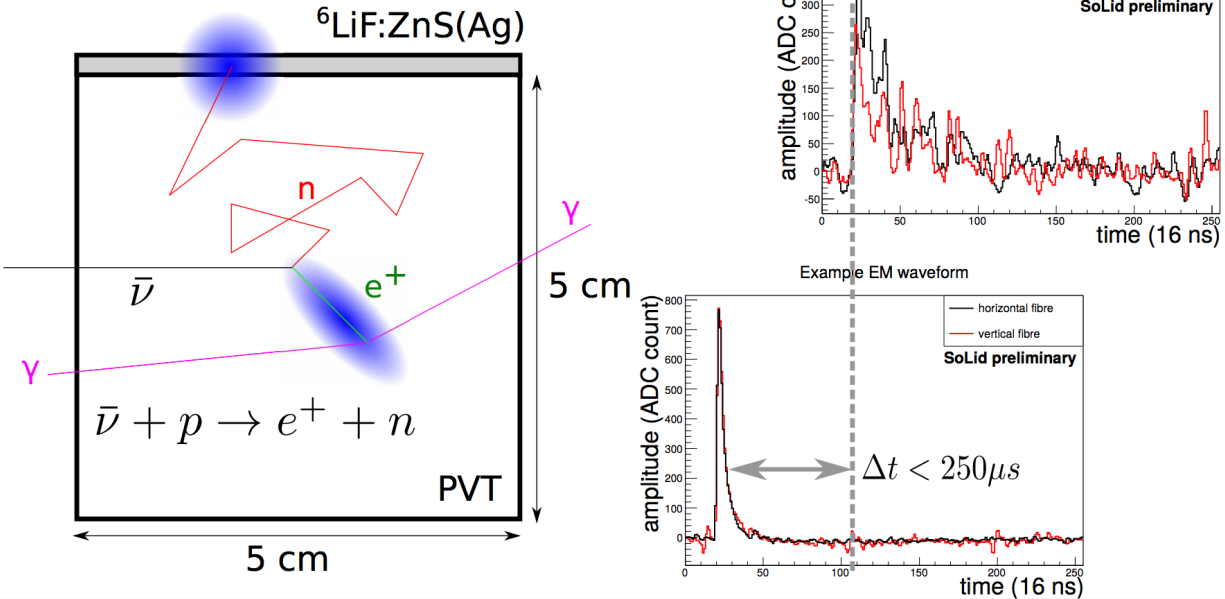
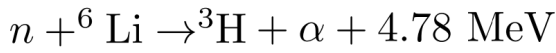


Figure 3.9: Right: Interaction of n and e^+ in the detector cube. Left: Comparison of the signals of n capture (upper) in ${}^6\text{LiF} : \text{ZnS}(\text{Ag})$, and e^+ capture in PVT (lower). *Source:* [89].

of the light can be captured by total internal reflection. The WLS fibre used at SoLid – SAINT-GOBAIN BCF-91A – consists of a polystyrene-based core and two layers of polymethyl methacrylate (PMMA), a highly transparent thermoplastic material, and shifts the light from blue to green spectrum. [92] [93] It is rectangular in shape and has a cross section of $3\text{mm} \times 3\text{mm}$, corresponding to the active area of the SiPM sensor (see [94] [95] for technical information).

Silicon Photomultipliers (SiPMs) – also referred to as Multi-Pixel Photon Counters (MPPCs) – are used as photosensors. SiPMs are pixel arrays of avalanche photodiodes operated 10...20% above breakdown voltage, in so-called Geiger mode [96]. Their advantages lie in their robustness, high photon-detection efficiency, single photon detection capability as well as their resolution, their low operational voltage and inexpensiveness. However, their high Dark-Count Rate (DCR) at room temperature, their excess noise due to inter-pixel cross-talk and their generation of after-pulses are disadvantages of the devices [97] [98]. DCR in SoLid is decreased by cooling down the detector module to 5°C . On SoLid, HAMAMATSU S12572-050 devices are employed, containing 3600 pixels each, peak sensitivity wavelength of 450nm and a Photon Detection Efficiency (also called *quantum efficiency*) of 0.35 and nominal DCR of typically 1kHz, decreased by one order of magnitude of by cooling down the detector [95] (see [73] for DCR–temperature dependence).

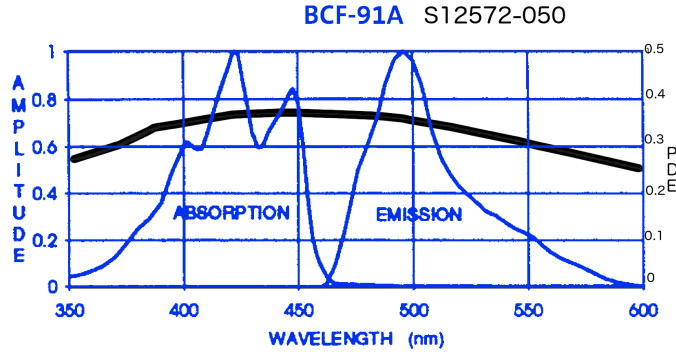


Figure 3.10: Absorption and emission spectra of the WLS fibre is shown in blue, Photon Detection Efficiency (PDE) of the SiPM is shown in black. *Source:* [94] [95] (edited).

Figure 3.10 shows the absorption and emission spectra of the WLS fibre, as well as Photon Detection Efficiency (PDE) of the SiPM.

3.2.5 Background

As SoLid is an overground experiment in proximity to the reactor core, a significant amount of background is faced in comparison to underground experiments [73]. These backgrounds include:

Cosmic Muons cause PVT scintillation when passing through the cube, thereby causing significant contribution to the background [88].

Cosmogenic Background is background caused by spallation reactions, such as decays of isotopes produced by muon-induced spallation reactions, spallation reactions caused by muon-induced neutrons entering from outside the detector, or nuclear recoils initiated by such neutrons [99]. Fast neutrons from cosmic ray showers might cause a similar signal to a positron signal by inducing a p recoil signal and being captured shortly after, mimicking an IBD signal. In order to reduce this effect, a water shield is built around the SoLid detector module. [92]

Intrinsic Background can occur by contamination of the ${}^6\text{LiF} : \text{ZnS}(\text{Ag})$ -layer by ${}^{214}\text{Bi}$ in the fabrication process. The ${}^{214}\text{Bi}$ isotope decays via β^- -decay to ${}^{214}\text{Po}$, emitting an e^- . The ${}^{214}\text{Po}$ itself decays by emitting an α -particle, looking signal-wise like a neutron. The e^- and α -particle can fake an IBD event [92] [100].



Figure 3.11: The SM1 prototype module. *Source:* [81].

3.3 Status of the experiment

SoLid is planned to enter its first large-scale data-taking phase in 2017. Two prototype phases have run earlier in order to demonstrate feasibility: NEMENIX and SM1.

3.3.1 NEMENIX

The first prototype, NEMENIX, was built in 2013. The 6kg-detector consists of 64 PVT cubes and 32 read-out channels, forming a detecting volume of approximately $20\text{cm} \times 20\text{cm} \times 20\text{cm}$. It was designed to provide proof of concept as well as acquire estimates of background and signal coincidence rates on the BR2 reactor site. [88] [100]

3.3.2 SM1

The SM1 prototype detector, shown in figure 3.11, contains 288kg of active scintillation material, arranged in 9 planes with 256 cubes each. A total of 100 channels is used for read-out. It took data in 2015 both when the BR2 reactor was running and when it was turned off. During the turn-off period, various radioactive sources have been used to investigate background conditions: ^{137}Cs , ^{60}Co , AmBe and ^{252}Cf . The latter two have been used for neutron studies, while ^{137}Cs and ^{60}Co were used for the calibration of the electromagnetic signals. [103] [100] An energy threshold trigger has been used for read-out [31].

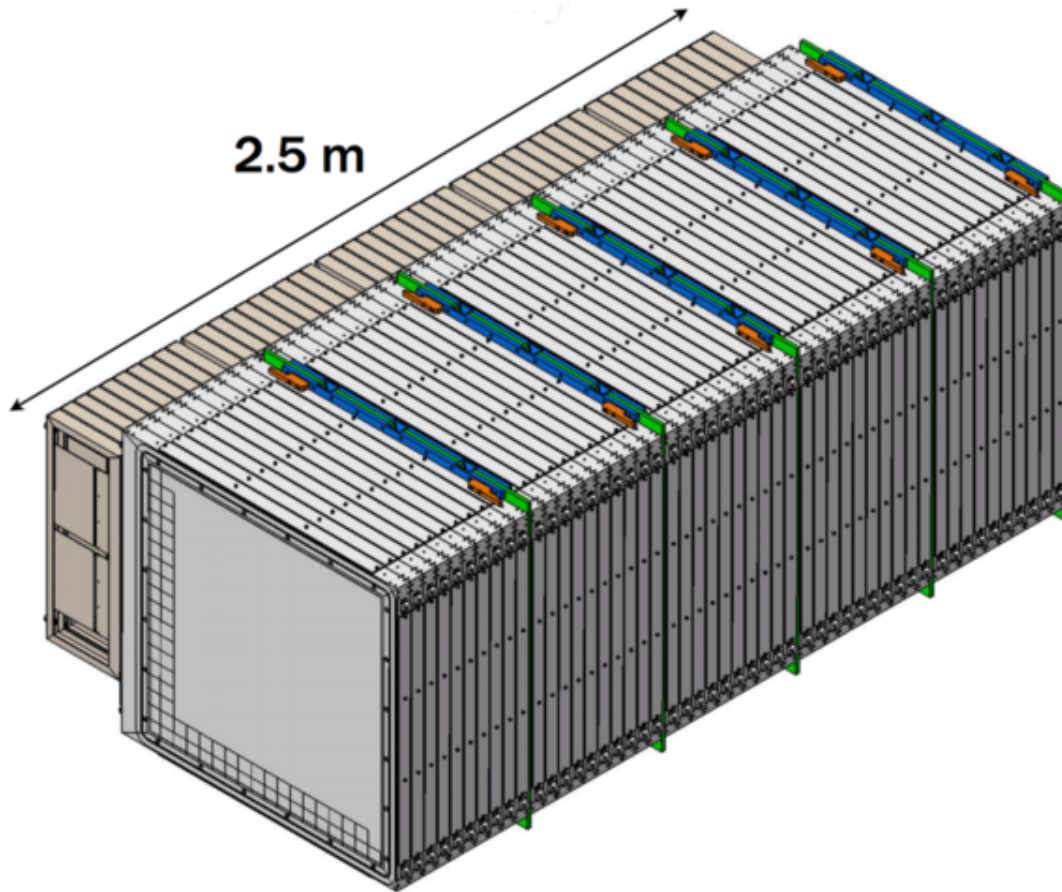


Figure 3.12: Three-dimensional rendering of the 1.6t-detector, consisting of 50 planes, used in Phase 1. *Source:* [101].

3.3.3 Phase 1

The first main run of SoLid – Phase 1 – will start in 2017. 1.6t of material is being used as scintillation material. 5 modules, thus 50 planes, are employed, and 3200 SiPM channels are used for read-out. [31] A rendering of the bare detector can be seen in figure 3.12 and the rendering of the detector placed in the container is shown in figure 3.13. Among upgrades in online software, storage, controls and detector technology – an additional ${}^6\text{LiF} : \text{ZnS}(\text{Ag})$ -layer will be added – a new trigger system will be implemented which significantly increases purity of the data and decreases data rate.

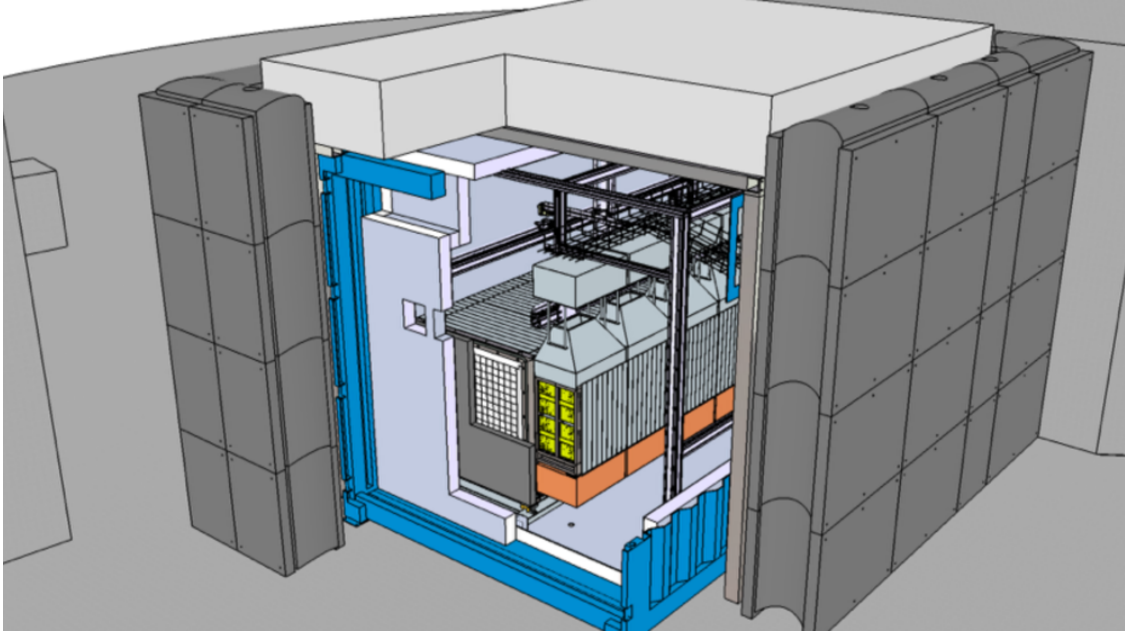


Figure 3.13: Three-dimensional rendering of Phase 1-detector placed in a container with surrounding water shielding. *Source:* [102].

3.3.4 Phase 2

The detector can be upgraded by adding more modules or by constructing an additional detector station with higher energy resolution. A potential upgrade which should be run as Phase 2 will have total sensitive mass up to 3t. [104] A sensitivity plot for both Phase 1 and Phase 2 can be seen on figure 3.14.

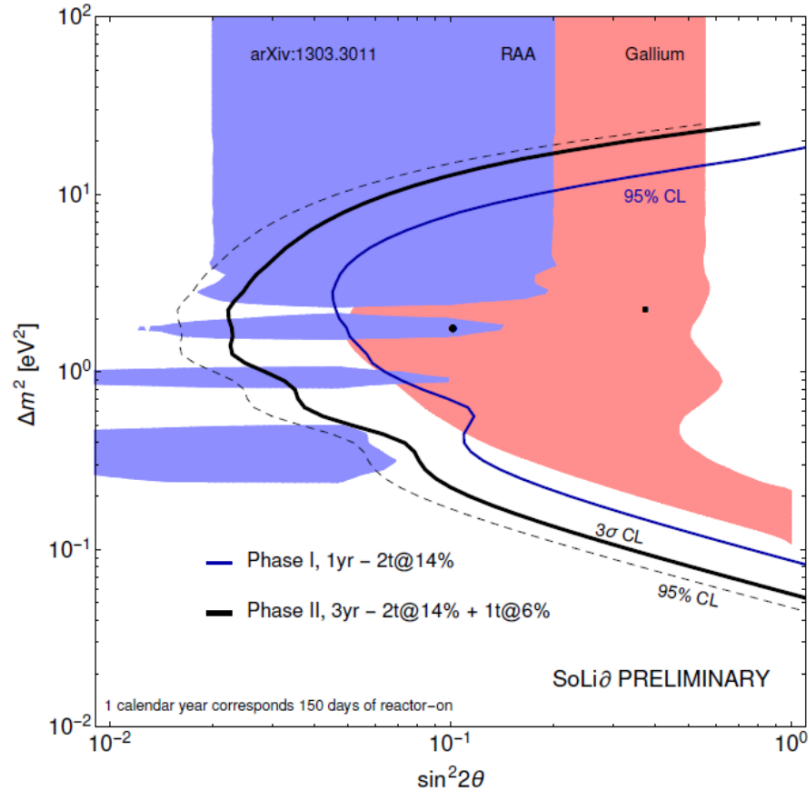


Figure 3.14: The estimated sensitivity of the SoLid experiment for Phase 1 (blue line) and Phase 2 (black line) to the reactor antineutrino anomaly (RAA) region (blue area) and the Gallium anomaly region (red area) as a function of Δm^2 and $\sin^2 2\theta$. The 95% C.L. are shown. *Source:* [89].

4 The SoLid Read-out System

The read-out system for acquiring the SiPM signals is composed out of two parts: the analogue front-end and the digital front-end, that also includes the trigger on a Field-Programmable Gate Array (FPGA) chip, as well as the power- and the I²C-board. The read-out electronics is placed on side of the frame containing the cubes, as shown in figure 4.1.

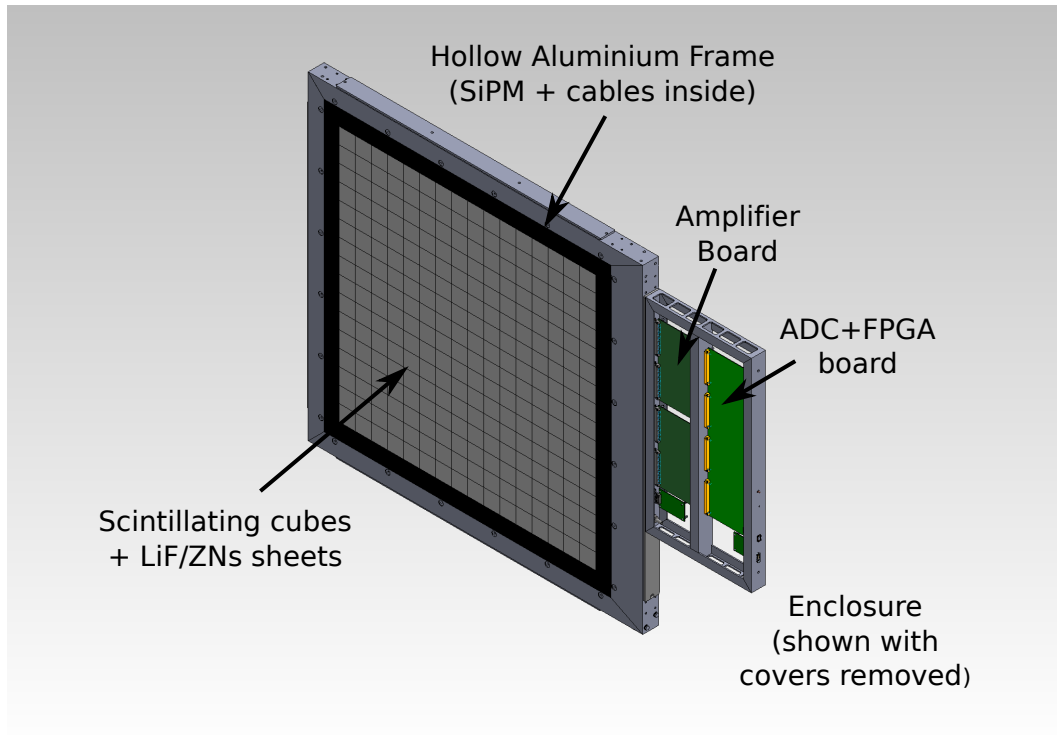


Figure 4.1: Three-dimensional rendering of a plane containing the cubes, the frame and the read-out electronics. *Source:* [31].

The boards are custom-made to serve the needs of the SoLid experiment.

As can be seen in the data flow diagram in figure 4.2, the SiPM sensor signals are shaped and amplified by a band-pass filter on the analogue front-end board before being sampled and processed by the digital board's components. The data then is sent out via Ethernet to the central online software.

4.1 Analogue Front-end

Two analogue front-end boards are used per plane, each serving 32 channels. Each board provides the bias voltage to the SiPMs, according to the value set by the digital board. On the input side, it receives, amplifies,

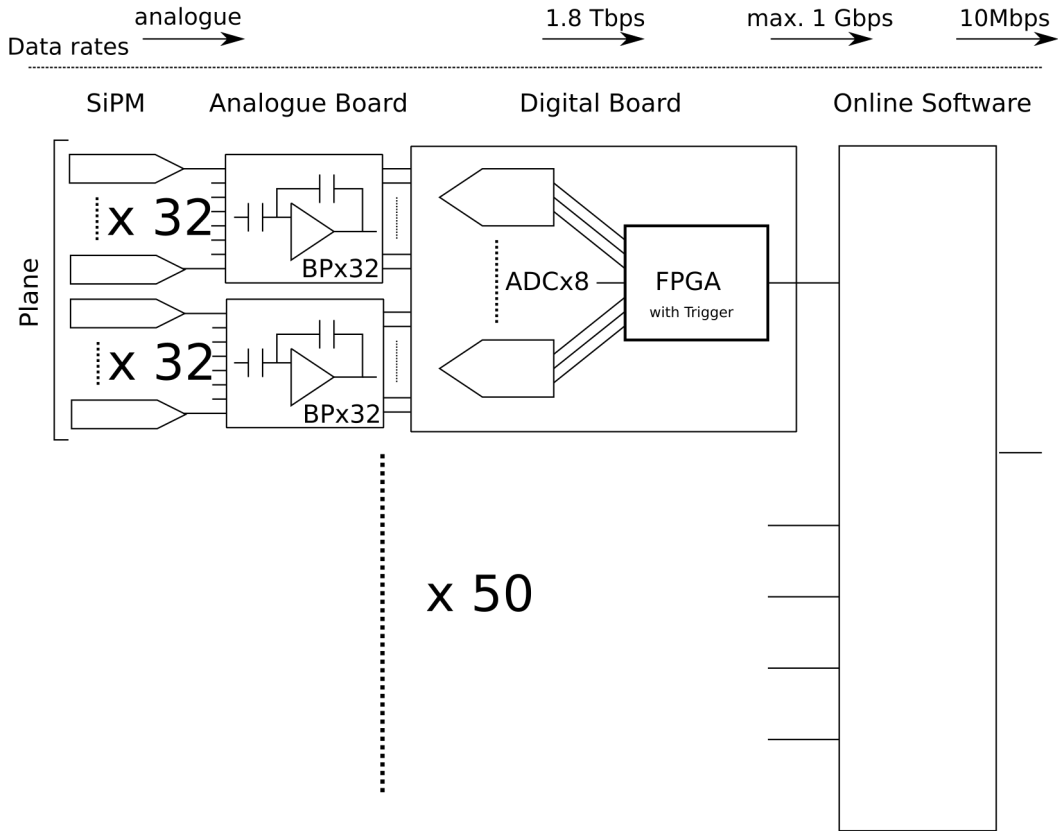


Figure 4.2: Flow of the signal: The SiPM input signal is shaped by the analogue board, then sampled and processed by the digital board before being fed into the online software. The expected data rate at each stage is outlined.

band-pass filters and shapes the signals. Accordingly, it is connected to the digital board on one end and to the SiPMs on the other, using differential signalling for the signals. [31]

4.2 Digital Front-end

The digital front-end board receives the signals from the analogue board. 8 Analogue-Digital Converters (ADCs) sample 8 channels each at a rate of 40MHz and a resolution of 14bit. The digitised signals are fed into the TRENZ FPGA module containing a XILINX ARTIX-7 FPGA chip. The digital board connects to JTAG over LVDS, contains a Gbit s^{-1} -Ethernet interface using Small Form-factor Pluggable transceivers (SFPs), direct 2.5Gbit s^{-1} links to neighbouring boards and is connected to the per-module clock and control signal distribution. A three-dimensional rendering can be seen in figure 4.3. [31]

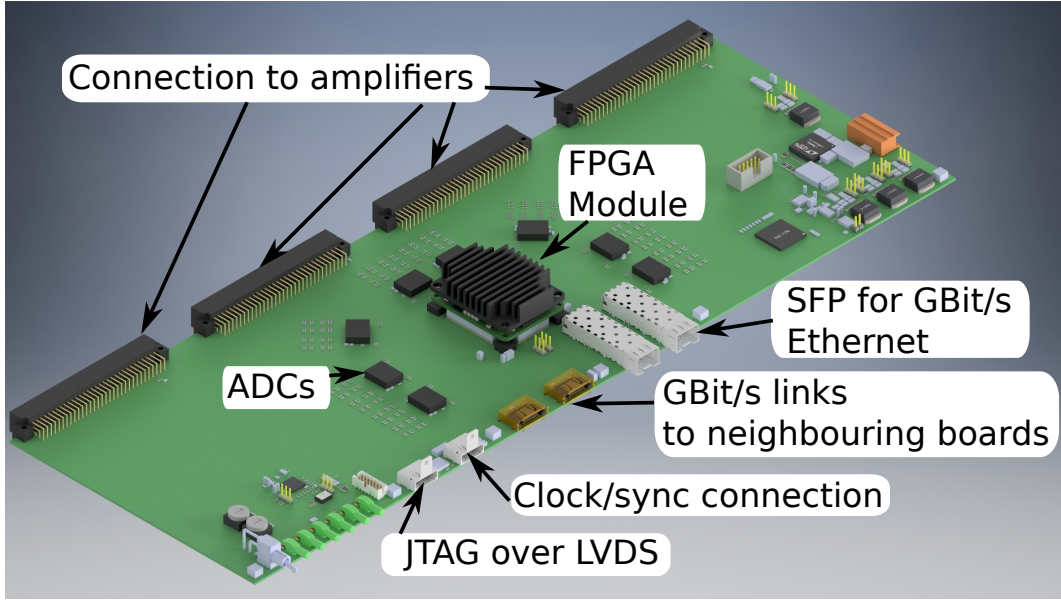


Figure 4.3: Three-dimensional rendering of a digital front-end board. *Source:* [31].

4.3 Other Boards

The read-out electronics assembly also contains two smaller boards, each designated for a specific function. The power board, located under the digital front-end board, provides 5V outputs for digital and analogue use each, -3.3V for the FPGA, and 70V for the SiPM bias voltage. The I²C board, which is positioned beneath the analogue board, contains an I²C communication interface.

4.4 Shielding

As the plane’s frame is made of hollow extruded aluminium sections that are connected together and to the read-out electronics boards, it is a Faraday cage blocking electrical fields. A sketch of the shielding scheme can be seen in figure 4.4.

4.5 Data Generation and Rates

SoLid faces a large amount of background signals due to it being an overground experiment in proximity to the reactor core. This requires the read-out system – and the trigger part – to reject as many background signals as possible. The extent to which this rejection has to take place is dependent on data generation on one side and on the data handling capacity of the online software on the other.

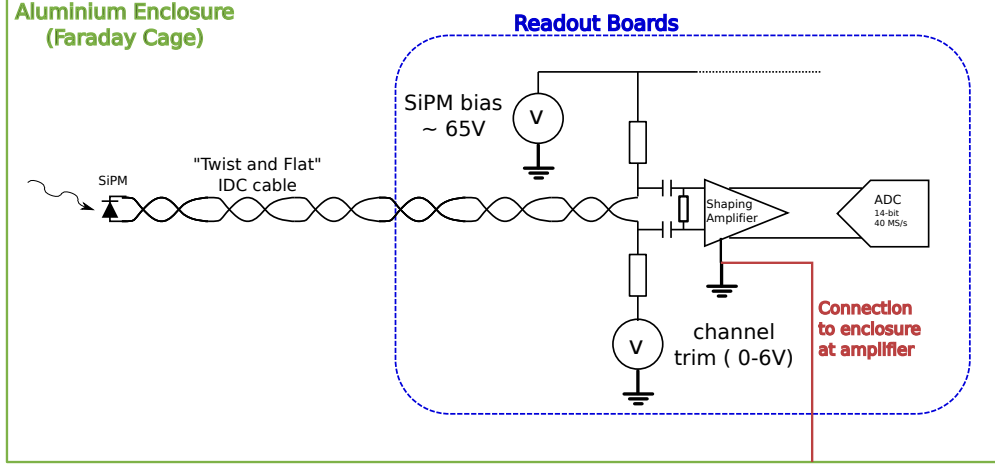


Figure 4.4: The shielding and grounding scheme of the read-out electronics. *Source:* [31].

Stage	Data rate $R[s^{-1}]$	Data rate $R[d^{-1}]$	Reduction factor r
Digital board	= 1.8Tbit	= 19PB	–
Online software (maximum)	~ 1.0 Gbit	~ 11 TB	~ 1800
Data storage	~ 10 Mbit	~ 100 GB	~ 100

Table 4.1: Data rates at the different stages of the data acquisition chain per second and per day. Reduction factor is given to the previous stage.

Data Generation is determined by sampling rate and resolution. Since a 14bit-ADC is used at a sampling frequency of 40MHz, with 64 channels per plane. The data rate – or bit rate – per plane amounts to

$$R_f = \#Channel \times Resolution \times Frequency = 64 \times 14\text{bit} \times 40\text{MHz} = 36\text{Gbit s}^{-1}. \quad (4.1)$$

Since 50 planes are employed on Phase 1, the data rate for the whole detector is

$$R_d = 1.8\text{Tbit s}^{-1}. \quad (4.2)$$

Data Handling Capacity is set by the capacity of the online software to process data. The software is estimated to be able to handle data up to a rate of $R_s \sim 1\text{Gbit s}^{-1}$ [105]. The minimum data reduction factor therefore is

$$r_d = \frac{R_d}{R_s} \sim 1800. \quad (4.3)$$

As reduction should be above the minimum limit in order to prevent data pile-up or even data loss, a reduction factor of $\mathcal{O}(10^4)$ is aimed for. The online software reduces the amount of data by additional two

order of magnitudes, leading to a data storage rate

$$R_s \sim 10\text{Mbit s}^{-1} \sim 100\text{GB d}^{-1}, \quad (4.4)$$

limited by the storage capacity at BR2. A summary of data rates and reduction factors is given in table 4.1. Obviously, the total reduction of the data rate by a factor of one million forms a challenge, in particular due to the fact that high efficiency is required and that a large amount of background data is faced. It is the task of the trigger to provide efficient, yet pure data reduction.

4.6 The SoLid Firmware

The SoLid FPGA firmware is responsible for buffering the data, triggering on it, and for communication with other planes as well as with the data acquisition device. Also, it has the slow-control for the SiPMs integrated in its functionality. It forms therefore a crucial part of the experiment's read-out chain. A block diagram with the firmware modules is shown in figure 4.8.

The firmware is based on the *IPbus* protocol, a gigabit Ethernet-based reliable high-performance protocol designed for particle physics experiments [106] [107]. Three tasks are carried out by the firmware: [108]

1. The *buffer*, that segments incoming data into chunks and applies zero-suppression (red in figure 4.8).
2. The *trigger*, that decides which part of the data is sent out (blue in figure 4.8).
3. The *control part*, that consists of the slow-control for SiPM and the communication link to the DAQ online system and to other planes of the detector (green in figure 4.8).

4.6.1 Buffer

The buffer stores the data coming from the ADC and prepares them to be sent out as soon as an event is triggered.

For each channel, data is fed through a channel pipeline, consisting of the deserialiser, the latency buffer, the zero suppression, the window buffer, channel read-out and the derandomiser. Each channel pipeline is connected to the main data buffer.

The **deserialiser** converts the serial data received from the ADC and converts them into 14bit words. Alternatively to the deserialiser, data can be fed into the buffer from a **pattern generator** or as **playback** of existing data. It hands the data to the trigger and the latency buffer.

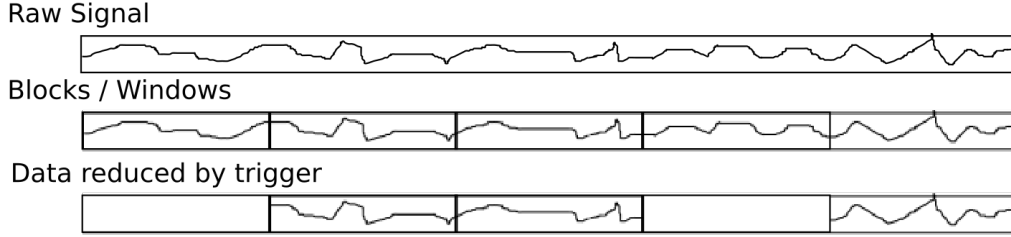


Figure 4.5: Raw data is segmented into defined blocks or time windows, usually consisting of 256 samples. The trigger decides on a block-by-block basis whether data should be read out.

Data is divided into different segments of equal size by the buffer, usually 256 samples, as shown in figure 4.5. A **latency buffer** holds the data streams for the time corresponding to two blocks in order to allow the trigger to make a decision.

The **zero suppression** suppresses data below a certain threshold. Hence it sets all data points below threshold θ to 0,

$$X(t) = \begin{cases} 0, & \text{if } X(t) < \theta, \\ X(t), & \text{otherwise,} \end{cases} \quad (4.5)$$

with expected data reduction by the factor of $\mathcal{O}(10)$. The samples put to 0 are removed and replaced by a marker. The marker contains information of how many sequential samples have been removed. The threshold θ can be varied depending on which type of trigger has been activated.

After zero suppression has been applied where appropriate, the **window buffer** holds the data for a certain time period to allow the trigger to initiate read-out of data recorded earlier. An overflow of the window buffer is critical as this would disrupt the pipeline in such a way that no more data may be read out until re-synchronisation.

The **channel read-out** hands single blocks to the derandomiser following a read-out request.

The **derandomiser** stores blocks for transfer into the main readout buffer. An overflow will result in ignorance of read-out requests, in which the deadtime monitor will account for the missed blocks.

All the 64 channel's derandomisers are fed into the main data buffer. [109]

4.6.2 Trigger

The **channel trigger** performs feature extraction and triggering on the buffer as data come in. It decides real-time on a block-by-block basis and forwards the decisions to the local trigger. Its parameters are programmable. The channel trigger is described in section 5.

The **local trigger** contains one or more trigger generator units. The local trigger is responsible for making the trigger decision for one plane. Trigger generator units form the local trigger based on information provided by the channel trigger values. Trigger decisions are passed to the readout sequencer, but also can be sent to neighbouring planes. Information is sent to the read-out controller on how many triggers are active and which features have caused them. At the current stage, the local trigger uses OR-logic, i.e. logical disjunction, to combine the channel trigger decisions, but can be extended to contain more sophisticated algorithms, as will be discussed in section 5.6.

The **deadtime monitor** records deadtime caused by overflow or other malfunction of the firmware for each channel and each trigger. Deadtime can occur both by suppression of individual blocks or triggers. [109]

4.6.3 Controls

The control part is responsible both for communication, including sending data out, and slow-control of the SiPMs.

The **read-out sequencer** translates all kinds of trigger decisions into the sequence of data blocks to be sent out. Each trigger type is linked to an offset and a block-count in a table that is used for the translation. Blocks tagged by multiple triggers are merged by the read-out sequencer. The read-out provides the read-out controller with information about the channels to be read out and whether read-out is skipped due to deadtime.

The read-out controller linked to the **header buffer** collects data from the channel buffers to the main data buffer. It formats the data and appends header and trailer information in order that the data sent out can be decoded.

The **IPbus controller** is responsible for the *IPbus* register and encodes and decodes communication from and to these registers.

The **timing/sync controller** controls clock synchronisation and generation from a distributed clock input.

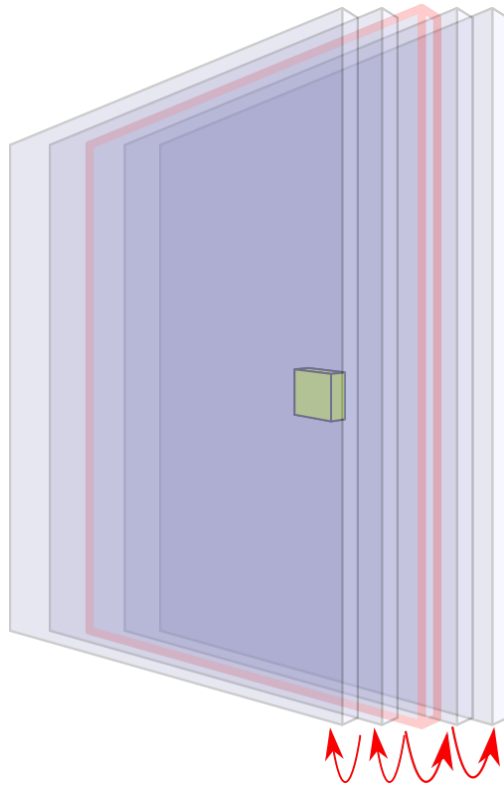


Figure 4.6: Following a trigger decision on one plane, the trigger can be spread along neighbouring planes.

	Logic cells	CLBs	DSPs	Block RAM [kbit]	I/Os
Total	215360	33650	740	13140	500
Per Channel	3365	526	12	205	8

Table 4.2: Available resources for the XILINX Artix 7-200T FPGA for the whole device and divided by the 64 read-out channels. *Source:* [111].

The **remote trigger** is able to spread trigger decision onto neighbouring planes via serial link (see figure 4.6). It also receives trigger decisions coming from remote planes and forwards them to the read-out sequencer and, where required, to other planes.

The **slow control** (not shown on the block diagram in figure 4.8) sets the bias voltages for the SiPM sensors.

4.6.4 Hardware

As buffer and trigger logic for 64 channels have to fit simultaneously on a single FPGA, a medium-density device – the XILINX Artix 7-200T FPGA – is used. The FPGA is placed on a commercial module by TRENZ ELECTRONICS shown in figure 4.7. The TRENZ board contains – beside the FPGA – a clock chip (SILICON



Figure 4.7: TRENZ module containing the XILINX Artix 7 FPGA. *Source:* [110].

LABS Si5338), 4 Multi-Gigabit Transceivers (MGT), 256Mbit Quad-SPI Flash memory, 1GB DDR3 SDRAM, DC-DC converters, 75 LVDS pairs and 4 single-ended I/O pins. [110] [112]

The XILINX 7-Series, to which the employed Artix 7-200T belongs, rely on 28nm technology. The Artix family is optimised for high logic throughput and low-power applications using serial links. A summary of key parameters can be seen in table 4.2. [111]

Irradiation can cause damage to the FPGA and other electronic parts [113]. However, the ionising radiation being faced is about the same as normal background levels. The increase in neutron and gamma flux by the reactor is compensated for by water and containment shielding of SoLid. Even if a Single Event Upset (SEU) occurs, the FPGA simply can be re-flashed due to it being connected to a JTAG link.

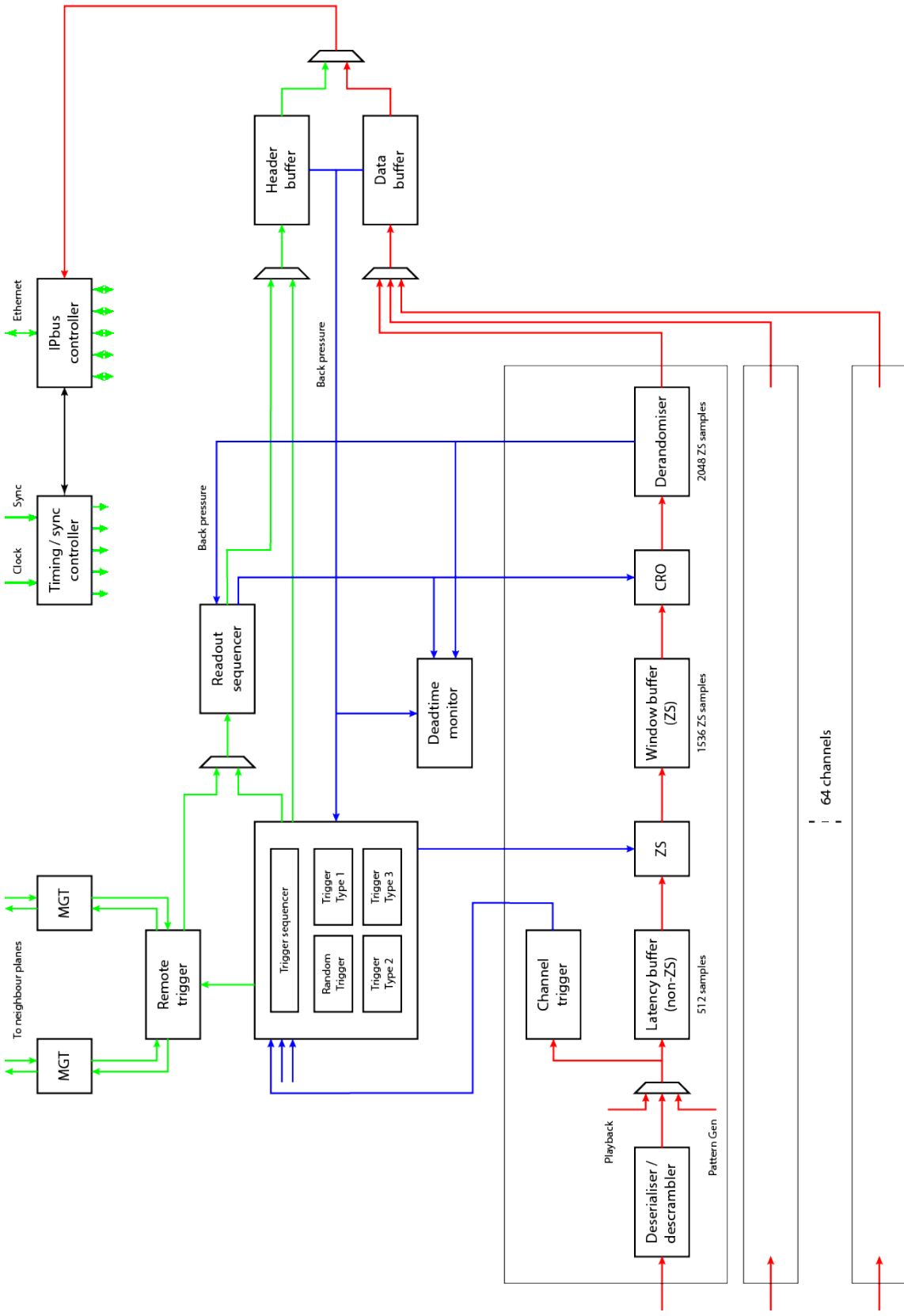


Figure 4.8: Block diagram of the firmware. *Source:* [31] (edited).

5 The SoLid Trigger

As data rate would be too high for sending out all incoming signals, a decision has to be made which data are probably meaningful in terms of their content and thereby sent for further processing. This decision is made by the *trigger*. A trigger thus classifies data on a rolling base into probably useful data – to be sent out – and probably meaningless data – to be discarded. Hence it can be seen as a *real-time classifier*, and statistical classification theory – as part of pattern recognition and machine learning theory – can be applied.

This section forms the part of the research carried out by me. A theoretical introduction in classification theory is given in section 5.2. Methodology and designs of feature extraction and machine learning algorithms are discussed in section 5.3. Discussion of evaluation results are shown in section 5.4. Finally, an implementation is presented in section 5.5 and prospect for the plane-level trigger is given in section 5.6. Conventions used in the mathematical representation of the trigger are given in the appendix A.2.

5.1 Trigger Types

As described in section 3.2, the IBD process produces a positron and a neutron. While the positron signals appear with no significant latency, the neutron signal is delayed by $\mathcal{O}(10^{-4})$ s. And while the positron signal forms a short light pulse, the neutron appears as a long signal of $\mathcal{O}(10^{-6})$ s. Therefore, different triggers are used for the two kinds of signal. The positron signal – due to its discriminability and briefness – is fairly easy to distinguish. A threshold trigger is used. However, designing the neutron trigger is more challenging, as its signals usually do not reach high amplitudes. This prevents the usage of a threshold trigger due to the length of the signal, as the number of non-neutrons mis-classified as neutrons must be limited. This section deals with theory, methods and results that were applied to evaluating the neutron trigger.

5.2 Classification Theory

5.2.1 Signal Space

Preliminary, the concept of *signal space* shall be introduced, often being credited to Wozencraft and Jacobs [114], as the data to be classified actually can be seen as a representation of its underlying – analogue – signal.

The idea is to view signal waveforms as vectors in a vector space called *signal space*. These vectors represent analogue, continuous signals. The constituent vectors are time-dependent finite-energy functions

$$u(t) : \mathbf{R} \rightarrow \mathbf{C}, \quad (5.1)$$

where the condition of being finite-energy within an interval $[a, b]$ equates to them being square-integrable, i.e.

$$\|u\|^2 = \int_a^b |u(t)|^2 dt = \int_a^b u(t)\overline{u(t)} dt \neq -\infty, \infty \quad (5.2)$$

This derives from the definition of their norm $\|u\|$ as the square root of the inner product with itself,

$$\|u\| = \sqrt{\langle x, x \rangle}, \quad (5.3)$$

and the definition of the inner product of any two vectors within the interval $[a, b]$

$$\langle v, w \rangle = \int_a^b v(t)\overline{w(t)} dt. \quad (5.4)$$

The signal space is a \mathbf{L}_2 Lebesgue Pre-Hilbert space. In the case the interval $[a, b]$ is set to $[-\infty, \infty]$, it even is a complete \mathbf{L}_2 Lebesgue Hilbert space. [115] However, for the purposes of the trigger, only the signal within a time-interval will be used. Also, as will be discussed later in section 5.3.3, due to considerations with regards to the FPGA resources, only time-domain features of the signals are used, leaving out features in complex frequency domain, hence all signals can be considered *real* for our purposes.

5.2.2 Discrete Time Domain

An \mathbf{L}_2 Hilbert space can be used as a representation for analogue signals, but the reality on an FPGA looks quite differently, as one can imagine. FPGAs, like any other digital device, handle signals $u(t)$ discretely both on the u (signal) and t (time) axis. Physically, this corresponds to the process of converting the SiPM signal input to a digital signal, as done by the Analogue-Digital Converter (ADC).

Discretisation in time is achieved by multiplying the signal u with the sampling function – or Dirac comb – $\text{III}_T(t)$ that is a periodic series with period T of Dirac delta functions δ [117],

$$\text{III}(u) = u(t) \cdot \text{III}_T(t) = u(t) \cdot \sum_{k=-\infty}^{\infty} \delta(t - kT). \quad (5.5)$$

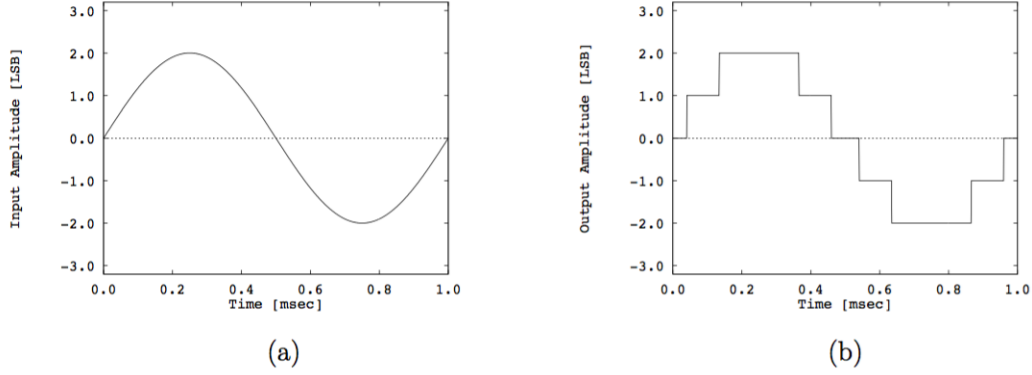


Figure 5.1: (a) Continuous input signal. (b) Signal after time-discretisation (Dirac deltas connected by lines) and quantisation. *Source:* [116].

Discretisation on the signal axis, called *quantisation*, or digitisation, can be formalised by [118]

$$Q(u) = \Delta \cdot \left\lfloor \frac{u}{\Delta} + \frac{1}{2} \right\rfloor, \quad (5.6)$$

for quantiser step size Δ , with $\lfloor \cdot \rfloor$ denoting the floor function. Combined time-discretisation and quantisation is a composition of the respective functions:

$$x(t) = Q \circ \text{III} \circ u(t), \quad (5.7)$$

with an example shown in figure 5.1. Equation 5.7 corresponds to an *ideal* ADC, while in the real case, channel noise \tilde{u} and effects caused by ADC non-linearity \tilde{Q} have to be considered:

$$x(t) = \left(Q + \tilde{Q} \right) \circ \text{III} \circ (u + \tilde{u})(t). \quad (5.8)$$

Two values with connection to time- and value-discretisation are of characteristic importance for the process: *Nyquist frequency* and *quantisation noise*.

According to the Nyquist-Shannon sampling theorem [119], all parts of a signal have to be below Nyquist frequency in order that they can be accurately reconstructed. Information for parts of the signal with higher frequency might be lost. Nyquist frequency f_n is half the sampling frequency f_s [120]:

$$f_n = \frac{1}{2} \cdot f_s. \quad (5.9)$$

Period T [ns]	Quantisation step size Δ [$\mu\text{V bit}^{-1}$]	Nyquist frequency f_n [MHz]	$SQNR_{max}$ [dB]
25	201.4	20	88.8

Table 5.1: Characteristic values for time-discretisation and quantisation.

Flooring values in the quantisation process leads to quantisation noise. Given the general formula of signal-to-noise ratio (SNR) [120],

$$\text{SNR} = \frac{\sigma_{\text{signal}}^2}{\sigma_{\text{noise}}^2} \quad (5.10)$$

where σ^2 is the variance of signal and noise, respectively, signal-to-quantisation-noise can be approximated by [121]:

$$\text{SQNR} = \frac{3 \cdot 4^{n\text{bit}} \cdot P_{x^{n\text{bit}}}}{x_{max}^2} \sim \left(\log_{10} \left(\frac{P_{x^{n\text{bit}}}}{x_{max}^2} \right) + 6n\text{bit} + 4.8 \right) [\text{dB}], \quad (5.11)$$

with $n\text{bit}$ being the number of bits used and $P_{x^{n\text{bit}}}$ being calculated by the probability distribution function $pdf(x)$:

$$P_{x^{n\text{bit}}} = \int x^2 pdf(x) dx = E[x^2]. \quad (5.12)$$

As the exact pdf is not known, the maximum SQNR is more feasible to calculate and might be sufficient, simplifying equation 5.11 to:

$$\text{SQNR}_{\text{max}} = 3 \cdot 4^{n\text{bit}_{\text{max}}} \sim (6n\text{bit}_{\text{max}} + 4.8) [\text{dB}]. \quad (5.13)$$

A table with the values indicated in equations 5.5 to 5.13 is shown in table 5.1. The short positron light pulse is expected to have a bandwidth of $\sim 10\text{MHz}$, thus lies below Nyquist frequency.

5.2.3 Data Representation

For usability, discrete signals are often represented as vectors, with the Dirac combs being mapped to the integer vector items:

$$\mathbf{X}_k^{\mathbf{R}^n} = x(T \cdot k + C), \quad (5.14)$$

with the time offset C chosen so that the Dirac combs are located at time $(T \cdot k + C)$ and dimensionality n equate to the number of entries. One could take a step closer to reality, and map this vector into Boolean space \mathbf{B}^n or $\mathbf{B}^{m \times n}$,

$$\mathbf{X}_{((ij-1)+j)}^{\mathbf{B}^n} = \mathbf{X}_{ij}^{\mathbf{B}^{m \times n}} = j\text{th position in binary representation of } (\mathbf{X}_i^{\mathbf{R}^n}), \quad (5.15)$$

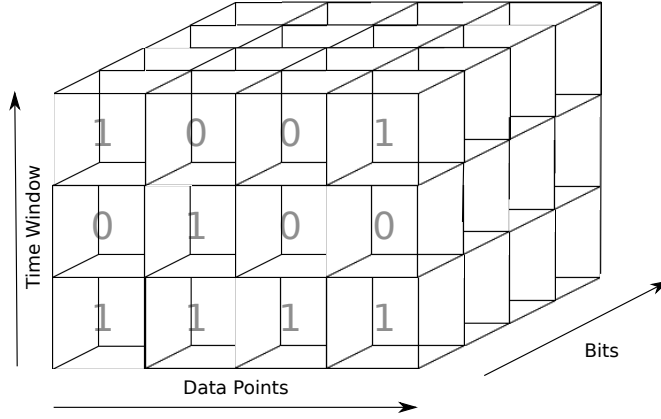


Figure 5.2: Data cube (or tensor) containing signal information. Corresponds to equation 5.16.

where rows i represent data points corresponding to $\mathbf{X}_i^{R^n}$ and columns j represented bit value in the case of a $\mathbf{X}^{B^{m \times n}}$ matrix, or position $i + j$ for the \mathbf{X}^{B^n} vector.

Data points can be further segmented into l time windows of length m , giving a multi-dimensional array, or tensor, or data cube $\in B^{l \times m \times n}$. This is the case for SoLid where data is segmented into packages. The new tensor will then be:

$$\begin{cases} \mathbf{X}_{kij}^{B^{l \times m \times n}} = \mathbf{X}_{uv}^{B^{m \times n}} \\ u = i + \lfloor \frac{k}{l} \rfloor \cdot i \\ v = j \end{cases}, \quad (5.16)$$

represented in figure 5.2. Note that the different notations of the discrete signal are isomorphic ($x \cong \mathbf{X}^{R^n} \cong \mathbf{X}^{B^n} \cong \mathbf{X}^{B^{m \times n}} \cong \mathbf{X}^{B^{l \times m \times n}}$).

As a convention within this thesis, if data vector \mathbf{X} appears without a superscript, it means the representation in $B^{l \times m \times n}$ is used.

5.2.4 Trigger Formalisation

The purpose of the trigger is data reduction. The data to be sent out should be much smaller than the acquired data on the trigger level, or

$$\dim \mathbf{X}_s \ll \dim \mathbf{X}, \quad (5.17)$$

achieved by discarding data points i in the $\mathbf{X}_{ij}^{\mathcal{B}^{m \times n}}$ representation of the data vector. Note that dimensionality for an $l \times m \times n$ structure is

$$\dim \mathbf{X} = l \times m \times n. \quad (5.18)$$

The size of each data point and the number of data points cannot be reduced. For SoLid, these are $n = 14$ and $m = 256$. It is therefore the number of windows l that is reduced. The decision whether a window l can be discarded or not is a binary classification problem.

The formal definition of a classifier $f(\mathbf{X})$ is [122] [123]

$$\hat{\mathbf{Y}} = f(\mathbf{X}), \quad (5.19)$$

where $\hat{\mathbf{Y}}$ denotes the *class* and \mathbf{X} is the data cube, or tensor, representing the data set. Each time window $\mathbf{X}_{k..}$ is mapped to a class $\hat{\mathbf{Y}}_i$, taking a value of a finite set of classes \mathbb{K} . \mathbb{K} in the present case is {discard, not discard} and can be represented as $\{0, 1\}$ in \mathcal{B} .

There is a problem in doing so: The dimensionality of each row k in Boolean space $\mathcal{B}^{l \times m \times n}$ can be high, and in fact too high for a computation device to practically handle. In the case of a time-wise segmented signal, such as for SoLid, the dimensionality is

$$\dim \mathbf{X}_k = m \times n = \frac{\text{length of time window}}{T} \cdot n\text{bit}_{\text{data point}}, \quad (5.20)$$

that for SoLid is $\dim X_k = 3584$. The classification in the FPGA has to be made as data come in, i.e. in real-time, not requiring more than a few clock cycles. Estimating the number of parallel operations o_p using

$$o_p \approx \frac{\dim \mathbf{X}_k}{I_{CLB} \cdot c_{max}} \quad (5.21)$$

with I_{CLB} being the number of Look-up Table (LUT) inputs and c_{max} being the maximum number of clock cycles, which can be put to $I_{CLB} = 6$ and $c_{max} \sim 5$, it is 120 parallel operations that would have to be processed per clock cycle. This is too high for a 64-channel FPGA to handle in real-time. The dimensionality therefore has to be *reduced*. This is commonly achieved by splitting classification into two parts: Feature extraction and application of the machine learning algorithm.

5.3 Trigger Design

The trigger classification function $f(\mathbf{X}_{l..})$ – operating on the matrix $\mathbf{X}_{l..}$ referring to a single time window l of the tensor \mathbf{X} – actually is a composite of two functions,

$$h \circ g(X) : \quad (5.22)$$

the mapping of

$$g(\mathbf{X}_{l..}) : \mathbf{X}_{l..} \in \mathbf{B}^{l \times m \times n} \mapsto \mathbf{F} \in \mathbf{B}^{l \times p \times n}, \quad (5.23)$$

with $p \ll m$, thus resulting in a feature vector \mathbf{F} having much lower dimensionality than the input data, and the actual classification $h(\mathbf{F})$, which is the application of the machine learning algorithm, giving the flow

$$\left(\mathbf{L}_2 \mathbf{H} \xrightarrow{\text{III}} \right) \mathbf{B}^{l \times m \times n} \xrightarrow{g} \mathbf{B}^{l \times (p \ll m) \times n} \xrightarrow{h} \mathbf{B}^l. \quad (5.24)$$

In terms of computation, the algorithm $g(\mathbf{X})$ should reduce the number of parallel processes by several orders of magnitude, while the splitting of the classification into two separate processes should increase computation time by just the factor of two.

For usability, the representation of \mathbf{F} as a real matrix $\mathbf{R}^{l \times p}$ shall be used, rather than the representation in Boolean space (that is closer to reality). As will be seen later in section 5.3.4, this representation – being a manifold on the original Hilbert space – contains a property very useful for classification

The function $g(\mathbf{X})$ is called *feature extraction*, with an allocated *feature space* $\mathbf{B}^{l \times p \times n}$. These should meet several requirements, namely

1. being a good practical representation of signal space,
2. having low dimensionality p (p indicates also the number of features),
3. allowing high-accuracy classification, and
4. being resource-efficient.

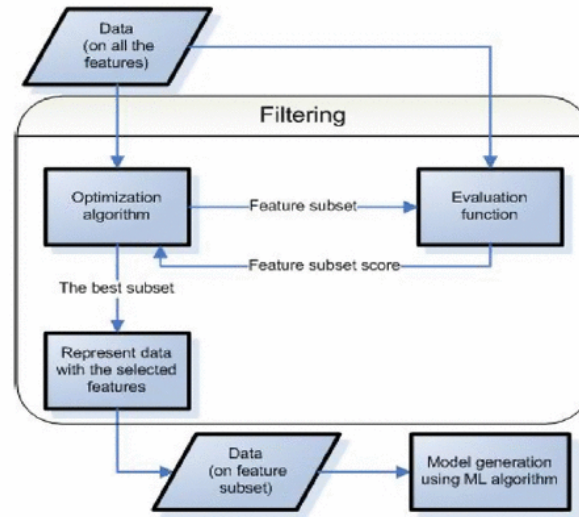


Figure 5.3: In the filter method, the quality of a feature space is evaluated using a score independent from the machine learning algorithm. *Source:* [124].

5.3.1 Metaheuristics

Finding a suitable feature space is a crucial, but also a complex task [125]. It consists of pre-processing the data, extracting features from the pre-processed data (called *feature extraction* or *feature engineering*), forming a primary feature space, and then finding a suitable subset of that space, usually of low dimensionality, forming the secondary feature space, a process that is called *feature selection*.

Feature selection is a well-investigated field – called *metaheuristics*. Two main approaches – or metaheuristic methods – exist for feature selection: The wrapper method, and the filter method. The wrapper method selects the feature set using evaluation by the classifier (see figure 5.4), while in the filter method, the selection of feature is independent from the used classifier (see figure 5.3). Also, hybrid methods exist. [126]

As the machine learning algorithm is not determined beforehand, the filter method is used for finding the SoLid trigger feature space. It will be explained later in section 5.3.4 that in the particular case of using a threshold function as the machine learning algorithm, the method is the same as the wrapper method. Individual algorithms are determined and evaluated on an individual basis. They will be ranked according to their performance, the correlation between them is determined and the most suitable chosen as the appropriate feature subset.

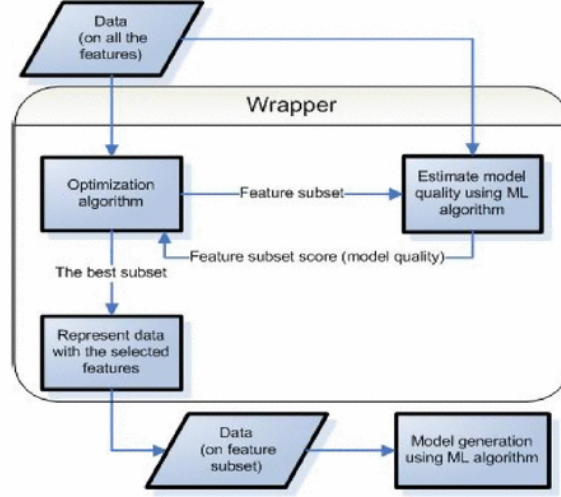


Figure 5.4: In the wrapper method, the quality of a feature space is evaluated using the machine learning algorithm. *Source:* [124].

5.3.2 Feature Evaluation

Evaluation is based on binary classifiers. The different algorithms are assessed individually, using a threshold classification function on each of the features,

$$h_i(\mathbf{F}_{li}, \theta_i) = \begin{cases} 1, & \text{if } x \geq \theta_i \\ 0, & \text{otherwise.} \end{cases} \quad (5.25)$$

The simple threshold trigger algorithm is one such function. For each feature \mathbf{F}_{li} , the threshold θ_i is swept from the minimum and maximum values within \mathbf{F}_{li} , leading to a Boolean binary classification vector $\hat{\mathbf{Y}} \in \mathbf{B}^l$. Assuming that a corresponding vector $\mathbf{E} \in \mathbf{B}^l$ exists representing whether the value \mathbf{F}_{li} is actually linked to a physical IBD event, four categories are defined: [127]

True positive (TP), correct hit:

$$h_i(\mathbf{F}_{li}) = \mathbf{E}_l = 1. \quad (5.26)$$

True negative (TN), correct pass:

$$h_i(\mathbf{F}_{li}) = \mathbf{E}_l = 0. \quad (5.27)$$

False positive (FP), false alarm:

$$h_i(\mathbf{F}_{li}) \neq \mathbf{E}_l = 0. \quad (5.28)$$

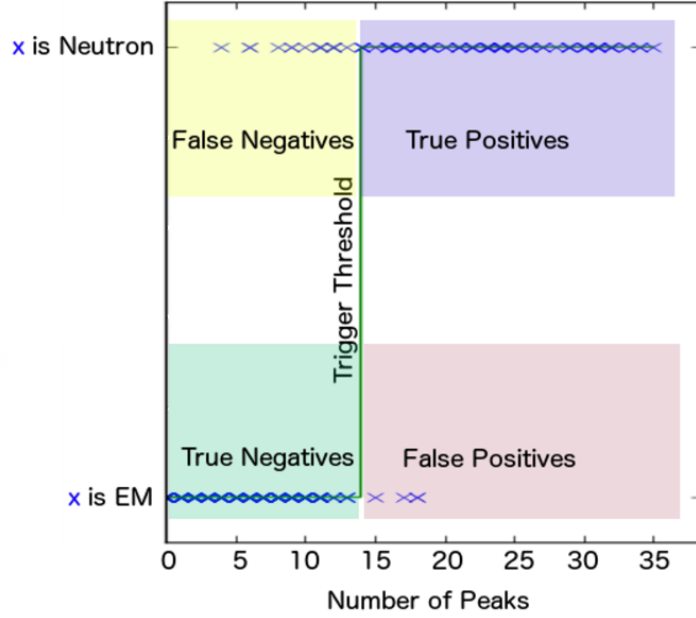


Figure 5.5: Example of categorisation for the Number-of-Peaks feature corresponding to i . The threshold θ_i is shown in green, the values \mathbf{F}_{li} in blue, and the value \mathbf{E}_i on the y -axis. The differently coloured areas mark the four different categories TP , TF , FP and FN .

False negative (FN), miss:

$$h_i(\mathbf{F}_{li}) \neq \mathbf{E}_l = 1. \quad (5.29)$$

An example for SoLid signals is shown in figure 5.5.

These abbreviations simultaneously stand for the number of how many times one of these categories has occurred within a given sample, i.e.

$$TP = |\{\mathbf{F}_{li} | \forall \mathbf{F}_{li} : h_i(\mathbf{F}_{li}) = \mathbf{E}_l = 1\}|, \quad (5.30)$$

$$TN = |\{\mathbf{F}_{li} | \forall \mathbf{F}_{li} : h_i(\mathbf{F}_{li}) = \mathbf{E}_l = 0\}|, \quad (5.31)$$

$$FP = |\{\mathbf{F}_{li} | \forall \mathbf{F}_{li} : h_i(\mathbf{F}_{li}) \neq \mathbf{E}_l = 0\}|, \quad (5.32)$$

and

$$FN = |\{\mathbf{F}_{li} | \forall \mathbf{F}_{li} : h_i(\mathbf{F}_{li}) \neq \mathbf{E}_l = 1\}|. \quad (5.33)$$

In addition, the positives P and the number of negatives N simply give the total numbers of these values in **E**.

Having these definitions, the following indicators for classification performance and accuracy can be used: [128]

Sensitivity or true positive rate (TPR) or trigger **efficiency**:

$$TPR = \frac{TP}{P} = \frac{TP}{(TP + FN)} \quad (5.34)$$

Precision or positive predictive value (PPV) or trigger **purity**:

$$PPV = \frac{TP}{(TP + FP)} \quad (5.35)$$

Fallout or false positive rate (FPR) or **fake rate** of the trigger:

$$FPR = \frac{FP}{N} = \frac{FP}{(FP + TN)} \quad (5.36)$$

Two characteristic plots can be obtained from those values: The receiver operating characteristic (ROC) curve, that shows efficiency versus fake rate, and a curve showing efficiency versus purity.

5.3.3 Feature Extraction Algorithms

The set of algorithms to be evaluated should contain high variety, as in this phase as many possible algorithms should be assessed in order to increase the likelihood to find well-performing algorithms. However, reasoning on which features will lead to effective classification is essential, bearing in mind that adding randomness to the creation of algorithms could cover the part that pure thought cannot. In other words, if \mathbb{G} is the set of all functions g_i mapping $\mathbf{B}^{m \times n} \rightarrow \mathbf{R}$, increasing the number of functions will cover more elements of that set \mathbb{G} .

The creation of some algorithms seem comprehensible, whereas others do not. As a high number of algorithms will be reduced after assessment on a later stage, that however cannot be considered to be a disadvantage. Fourier transformations on FPGAs usually use a lot of resources [129], often above 1000 LUTs [130]. As the FPGA usage of hardware resources has strict limits (see table 4.2), frequency-domain features hence will not be considered. Therefore only time-domain features are subsequently presented.

The single algorithms will be – in reference to equation 5.23 – be denoted as $g_i(X_{l..})$, mapping the signal from a given time window to one specific dimension of the feature vector. All the selected functions will then give g , i.e.

$$\mathbf{F} = \sum_i g_i(X_{l..}), \quad (5.37)$$

considering that all feature extraction functions g_i project to spaces orthogonal to each other.

The values $X[t]$ will be notated as elements of an array isomorphic to the discrete real array \mathbf{R}^n , as given in equation 5.14, with the notation rule

$$X[t] = \mathbf{X}_t^{\mathbf{R}^n}, \quad (5.38)$$

and the whole set X shall only consist of elements within a given time window l , i.e.

$$X = \{X[t-l], X[t-l+1], \dots, X[t]\}. \quad (5.39)$$

In addition to the function operating in the discrete signal, also a representation operating on the continuous signal $g_c(u) : \mathbf{L}_2\mathbf{H} \rightarrow \mathbf{R}$ is given where appropriate.

Maximum Amplitude Maximum amplitude is the feature used to trigger on the SM1 phase of SoLid. It simply uses the maximum value within a time window for triggering, i.e.

$$g_c(u) = \max u \quad (5.40)$$

for the continuous value and

$$g_i(X) = \max X \quad (5.41)$$

for the discrete value.

Number-of-Peaks The Number-of-Peaks feature counts the number of maxima above a certain threshold θ within a time window. An example is shown in figure 5.6. The threshold is set in order that pure noise-induced maxima are not considered. The reasoning behind this algorithm is that each time the ${}^6\text{LiF} : \text{ZnS}(\text{Ag})$ -layer is emitting a photon, a peak on the input signal occurs.

It may be expressed in continuous space as

$$g_c(u) = \left| \left\{ t \mid \forall t : u(t) > \theta \wedge \frac{du(t)}{dt} = 0 \wedge \frac{d^2u(t)}{dt^2} < 0 \right\} \right| \quad (5.42)$$

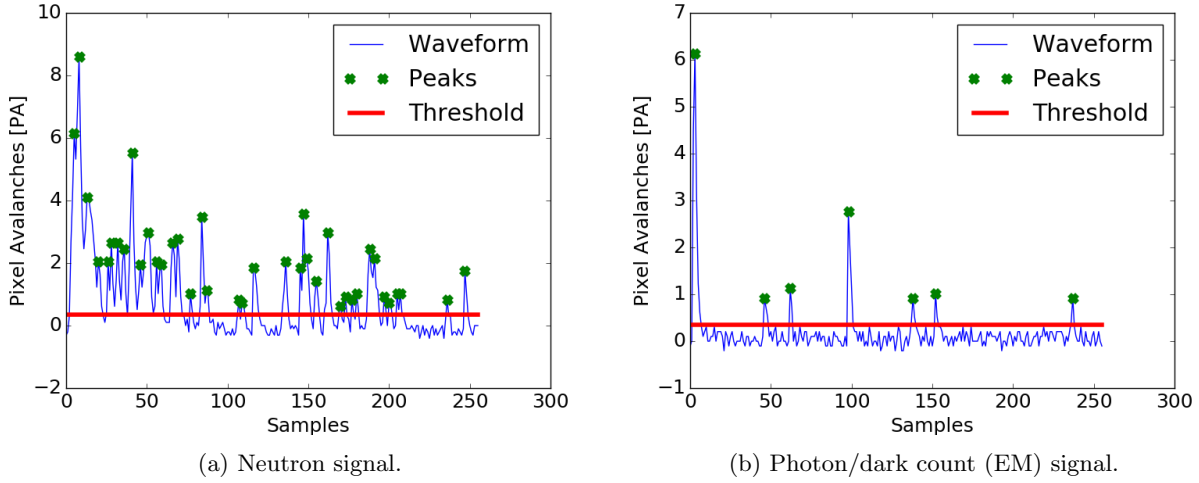


Figure 5.6: Peak finding algorithm. Green crosses represent found maxima above threshold.

and in discrete space either as

$$g_i(X) = |\{t|\forall t : X[t] > \theta \wedge \Delta X[t-1] \geq 0 \wedge \Delta X[t] < 0\}| \quad (5.43)$$

with the definition

$$\Delta X[a] = X[a] - X[a-1], \quad (5.44)$$

or

$$g_i(X) = |\{t|\forall t : X[t] > \theta \wedge X[t-1] \geq X[t-2] \wedge X[t] < X[t-1]\}|. \quad (5.45)$$

In other words, the cardinality – i.e. the number of elements – $|\cdot|$ of the set $\{\cdot\}$ of points that are a maximum above a certain threshold forms the feature.

One variation of the algorithm that also has been assessed is to add the condition that after a peak has found, following peaks will be ignored during a certain interval (*time veto*).

Weighted Peaks/Number of Photon Avalanches Another variation of the Number-of-Peaks feature is to weight the peaks by their amplitude. This equals to the number of pixel photon avalanches (PA). In continuous space this is expressed as

$$g_c(u) = \left| \left\{ u(t) \cdot t | \forall t : u(t) > \theta \wedge \frac{du(t)}{dt} = 0 \wedge \frac{d^2u(t)}{dt^2} < 0 \right\} \right| \quad (5.46)$$

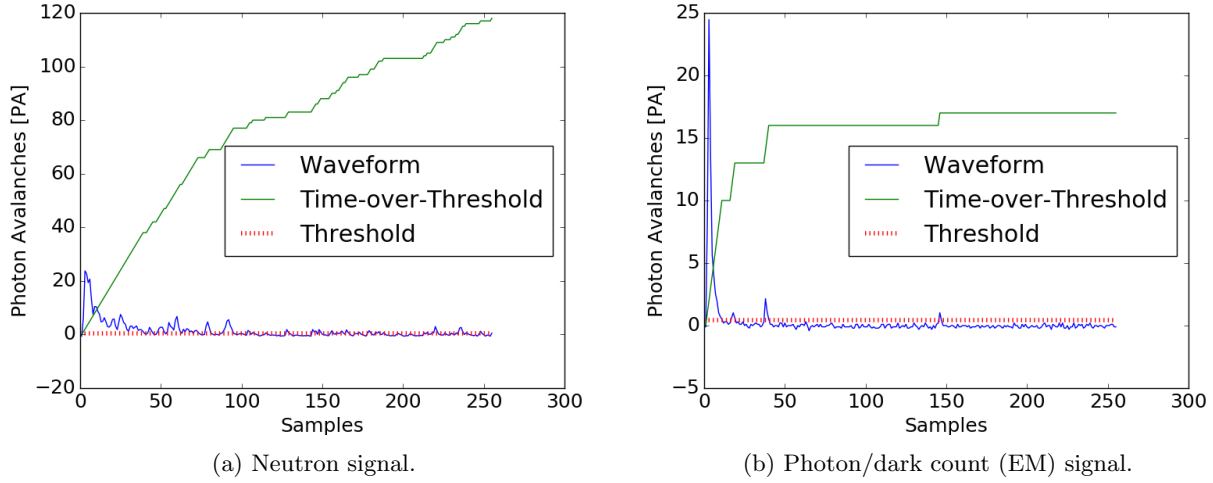


Figure 5.7: Time-over-Threshold algorithm.

and in discrete space as

$$g_i(X) = |\{X[t] \cdot t | \forall t : X[t] > \theta \wedge \Delta X[t-1] \geq 0 \wedge \Delta X[t] < 0\}|. \quad (5.47)$$

Time-over-Threshold The Time-over-Threshold measures the number of samples (i.e. length of time) a signal is above a certain threshold θ (see figure 5.7). This takes advantage of the fact that neutron signal last much longer than EM signals.

It is expressed as a a function of a continuous signal as

$$g_c(u) = \int \delta(t) dt \wedge \delta(t) = \begin{cases} 1, & \text{if } u(t) > \theta, \\ 0, & \text{otherwise} \end{cases} \quad (5.48)$$

and in discrete space as

$$g_i(X) = \sum_{t=1}^m \delta[t] \wedge \delta[t] = \begin{cases} 1, & \text{if } X[t] > \theta, \\ 0, & \text{otherwise.} \end{cases} \quad (5.49)$$

Decay Time *Falling time* means the time the signal undertakes until it falls below a certain percentage of its maximum value (see figure 5.8 for an example).

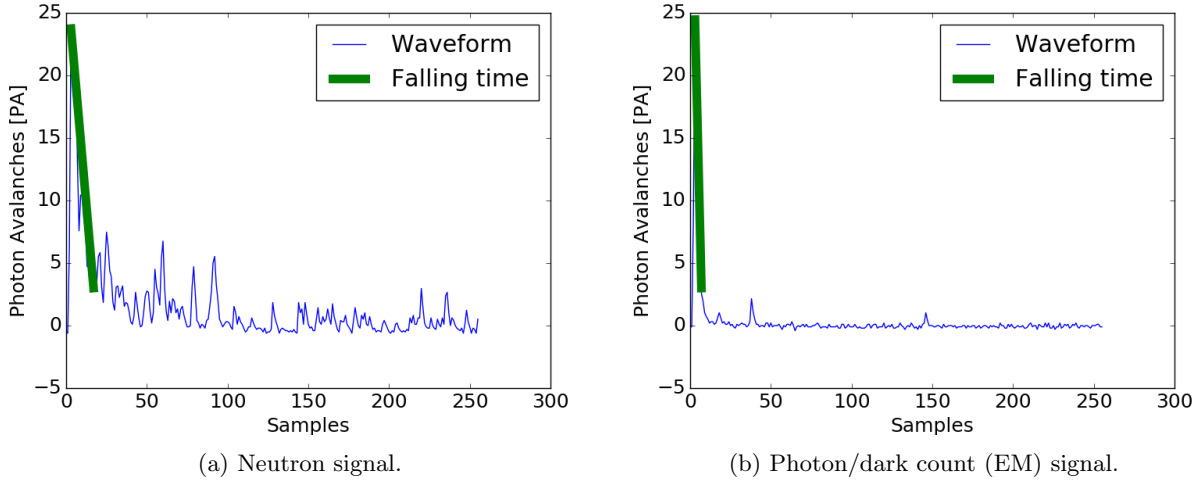


Figure 5.8: Falling time algorithm. The value is given as the x -axis projection of the green line.

Integral-over-Threshold and Integral The integral-over-threshold is calculated in continuous space as

$$g_c(u) = \int u(t)\delta(t) dt, \quad (5.50)$$

with $\delta(t)$ defined as in equation 5.48. This corresponds to the sum in discrete terms:

$$g_i(X) = \sum_{t=1}^m X[t]\delta[t], \quad (5.51)$$

with $\delta[t]$ defined as in equation 5.49.

For the integral feature, this simplifies to

$$g_c(u) = \int u(t) dt \quad (5.52)$$

and

$$g_i(X) = \sum_{t=1}^m X[t]. \quad (5.53)$$

Integral-over-Amplitude The Integral-over-Amplitude (or Integral/maximum Amplitude) divides the value obtained by equations 5.50 and 5.51 by division by maximum amplitude (equations 5.40 and 5.41), i.e.

$$g_c(u) = \frac{\int u(t) dt}{\max u(t)}. \quad (5.54)$$

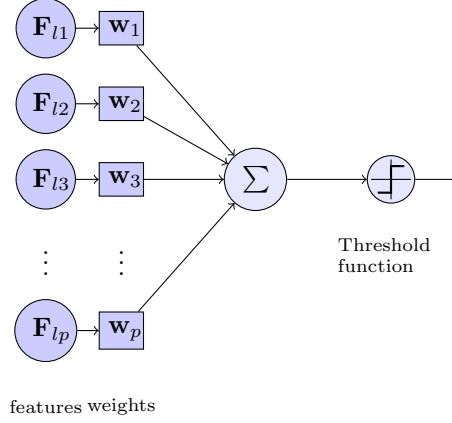


Figure 5.9: Block diagram of a perceptron.

This corresponds to the sum and a division in discrete terms:

$$g_i(X) = \frac{\sum_{t=1}^m X[t]}{\max X}. \quad (5.55)$$

Statistical Moments Statistical moments with their common definitions are considered such as *mean*,

$$g_i(X) = \frac{1}{m} \sum_{t=1}^m X[t], \quad (5.56)$$

and *standard deviation*:

$$g_i(X) = \sigma = \sqrt{\frac{1}{m} \sum_{t=1}^m (X[t] - \mu)^2}, \quad \text{where } \mu = \frac{1}{m} \sum_{t=1}^m X[t]. \quad (5.57)$$

5.3.4 Machine Learning Algorithms

Machine learning algorithms classify data using the features extracted. While feature extraction algorithms correspond to function $g(\mathbf{X})$ in equation 5.22, the machine learning algorithm corresponds to $h(\mathbf{F})$.

Threshold Function The simplest algorithm uses only one feature and triggers on this particular value. The threshold function is a step function [131] and in fact is the same as the function used for evaluation in equation 5.25. As evaluation and machine learning algorithms are the same in this case, the metaheuristics used for feature selection is the wrapper method rather than the filter method (see section 5.3.1).

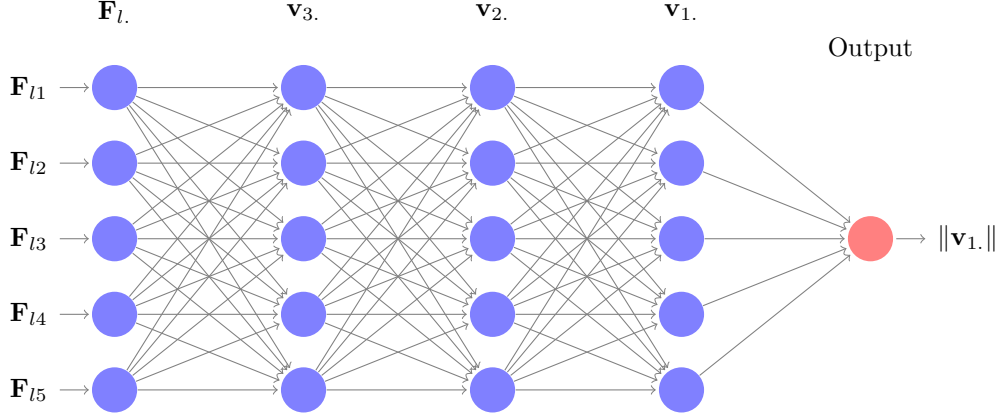


Figure 5.10: Block diagram of a feed-forward neural network.

Perceptron The single-layer perceptron, also called single-layer neural network or artificial neuron and suggested by Rosenblatt in 1958 [132] [133], triggers with a threshold θ on the inner product of the input or feature vector \mathbf{F}_l with a weight vector \mathbf{w} . This type of Artificial Neural Network (ANN) is the same as a linear classifier.

The feature vector \mathbf{F}_l of a single time window l of the feature matrix \mathbf{F} is considered. The space spanned by the feature vector \mathbf{F}_l can be seen as an \mathbf{R}^p manifold on the underlying analogue signal. This allows to apply the definition of the inner product, [134]

$$\langle x, y \rangle = x^T y = \sum_{i=1}^n x_i y_i = x_1 y_1 + \dots + x_n y_n, \quad (5.58)$$

in order to re-define the threshold function in equation 5.25 in order to get the perceptron function,

$$h(\mathbf{F}_l, \theta) = \begin{cases} 1, & \text{if } \langle \mathbf{F}_l, \mathbf{w} \rangle \geq \theta \\ 0, & \text{otherwise,} \end{cases} \quad (5.59)$$

or in other words: the single-layer perceptron triggers on the weighted sum of the individual features. A block diagram of the perceptron can be seen in figure 5.9. The weight vector has to be trained in terms of classification accuracy. [135]

Feed-Forward Neural Network The feed-forward neural network is an artificial neural network consisting of multiple layers [136]. Each of the nodes v_{ai} of one layer a connects to all the nodes of the neighbouring layers $a - 1, a + 1$. To each of the connections, a weight w_{aij} is assigned. Applying \mathbf{L}_1 metrics to \mathbf{v}_1 . (the

norm of a vector is defined as the sum of its elements), the output equates to the norm of the last layer \mathbf{v}_1 . A threshold function, as in equation 5.25, then can trigger on the output value.

The feed-forward neural network with number of layers χ can be formalised as

$$h(\mathbf{F}_1, \theta) = \begin{cases} 1, & \text{if } \|\mathbf{v}_1\| \geq \theta \\ 0, & \text{otherwise,} \end{cases} \quad (5.60)$$

with the recursive definition, again taking advantage of inner products (equation 5.58),

$$\mathbf{v}_{ai} = \begin{cases} \langle \mathbf{v}_{a+1}, \mathbf{w}_{ai} \rangle, & \text{if } a + 1 < \chi \\ \langle \mathbf{F}_j, \mathbf{w}_{ai} \rangle, & \text{otherwise.} \end{cases} \quad (5.61)$$

Dimensionality of the weight tensor \mathbf{w} increases exponentially with each added input variable or layer, leading to high computational demands for multi-layer, multi-input feed-forward neural networks. A block diagram of the feed-forward neural network is shown in figure 5.10.

5.4 Results

5.4.1 Test Setup

Test data have been used for feature evaluation, as data from the SM1 did not have sufficient quality. The test setup uses an $^{241}\text{AmBe}$ α -particle source, located $\sim 3\text{cm}$ from a PVT cube. The test detector catches signals with two SiPMs and a PMT. The test setup is sketched in figure 5.11. α -particle signals are very similar to neutron signals as both are caught by the $^6\text{LiF} : \text{ZnS}(\text{Ag})$ -layer [137], thus can be used to emulate IBD neutrons. Data read-out was triggered using a PMT signal, as the PMT delivers much more accurate signals than the SiPMs. Based on the PMT signal, the answer vector \mathbf{E} was created stating whether a signal is a neutron or not. The algorithm for creating the reference vector uses a maximum amplitude threshold as well as Time-over-Threshold for PMT neutron identification. 120000 events were acquired for the test data set, of which 2400 are neutron signals and the rest are electro-magnetic/dark-count signals.

Using the test setup gives rise to two uncertainties: One is that the degree is unknown on which test conditions reflect conditions faced during the actual reactor-on phase. The other is uncertainty about how accurately the PMT signal classifies signals into neutrons. However it is assumed that algorithms being

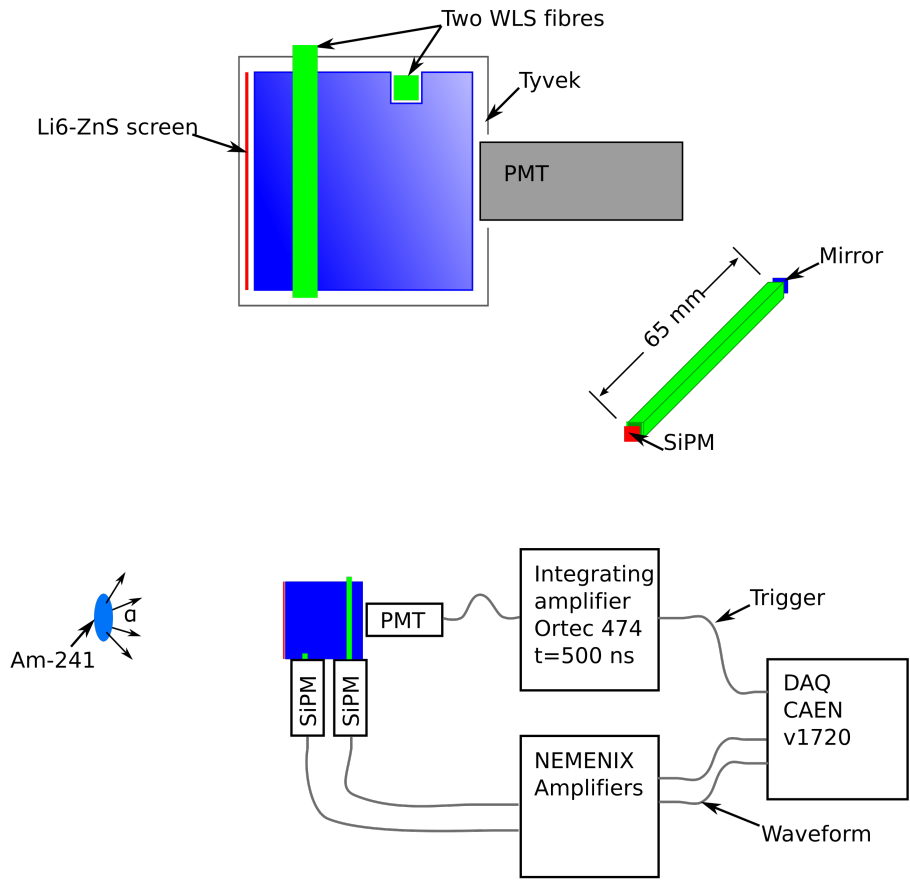


Figure 5.11: Test setup for taking data of an AmBe source for neutron trigger evaluation.

Algorithm	Optimum threshold θ[PA]
Number-of-Peaks	0.35
Time-over-Threshold	0.45

Table 5.2: Optimum thresholds θ for the Number-of-Peaks and Time-over-Threshold algorithms acquired by parameter sweeps.

evaluated as having good performance in test data will also perform well at the reactor site, and that mis-classification by using the PMT signal is negligible.

5.4.2 Feature Extraction Algorithms

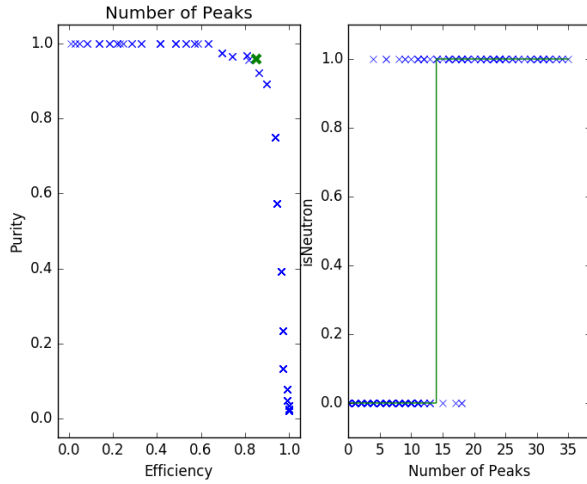
Features are assessed using the evaluation outlined in section 5.3.2. The threshold θ_i is swept from the minimum to the maximum value within the feature set in order to extract the corresponding curve. The procedure for selected features can be seen in figure 5.12: Each trigger threshold will produce a value on the purity-efficiency plane. Higher thresholds usually correspond to higher purity and lower efficiency, while lower thresholds correspond to higher efficiency and lower purity. Those features that perform well both in terms of efficiency and purity can be considered suitable for triggering.

Tuning Many features have free parameters, such as the threshold θ in the Number-of-Peaks (equation 5.42) and Time-over-Threshold (equation 5.48) algorithms. These parameters have to be tuned for the optimum value. This can be achieved by sweeping the free parameter [138].

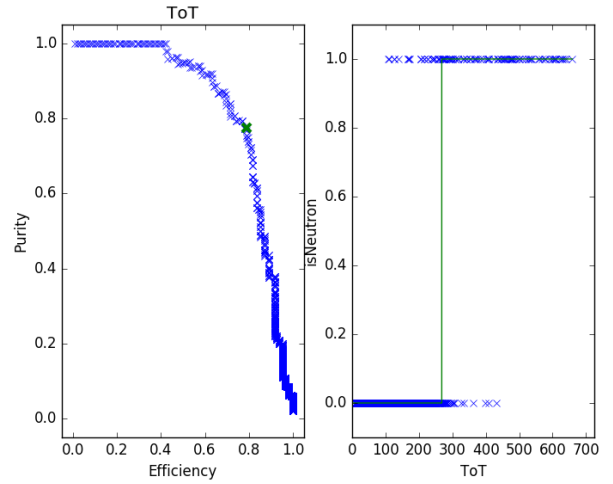
An illustration of feature tuning on the example of the Time-over-Threshold algorithm is shown in figures 5.13 and 5.14, with the threshold value being swept from 0 to 4.5. On the surface plot a peak is visible in the range of 0.5PA. This indicates that optimum performance is achieved with the threshold in this range.

The optimum thresholds are listed in table 5.2.

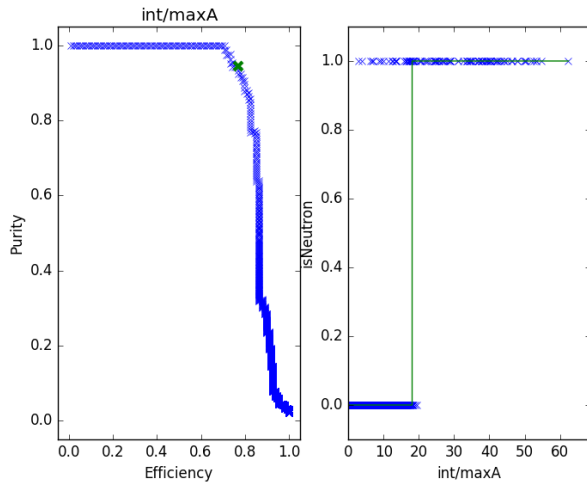
Comparison The overall comparison of features is used to reduce the number of potential features by short-listing those that perform well, i.e. that yield high efficiency, high purity and low fake rate simultaneously. Features yielding these characteristics allow a good distinction between neutrons and non-neutrons, in contrast to those having bad performance (a visualisation can be seen in figure 5.15). High efficiency (see equation 5.34) correlates with how many IBD physics events are caught. High purity (see equation 5.35) correlates with contamination of IBD events with backgrounds. And a low fake rate means that few non-IBD events are acquired (see equation 5.36).



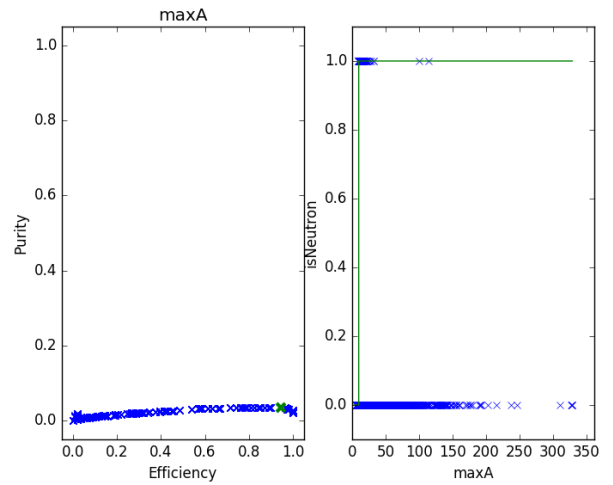
(a) Number-of-Peaks.



(b) Time-over-Threshold (non-optimum θ).



(c) Integral-over-Amplitude.



(d) Maximum Amplitude.

Figure 5.12: Evaluation of individual features for the Number-of-Peaks (a), Time-over-Threshold (b), Integral-over-Amplitude (c) and maximum amplitude (d) algorithms on the efficiency-purity plane (each left) and for categorisation (see figure 5.5) (each right). The green cross and green horizontal line indicate the optimum trigger threshold.

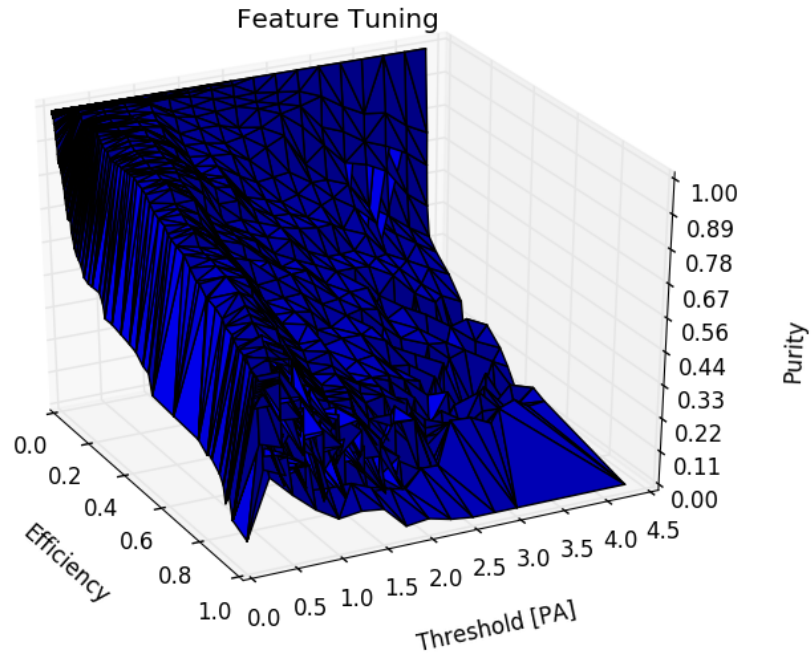


Figure 5.13: Surface plot for Time-over-Threshold feature tuning. Threshold is swept from 0 to 4.5PA with a mountain visible in the range of 0.5PA, indicating the optimum value.

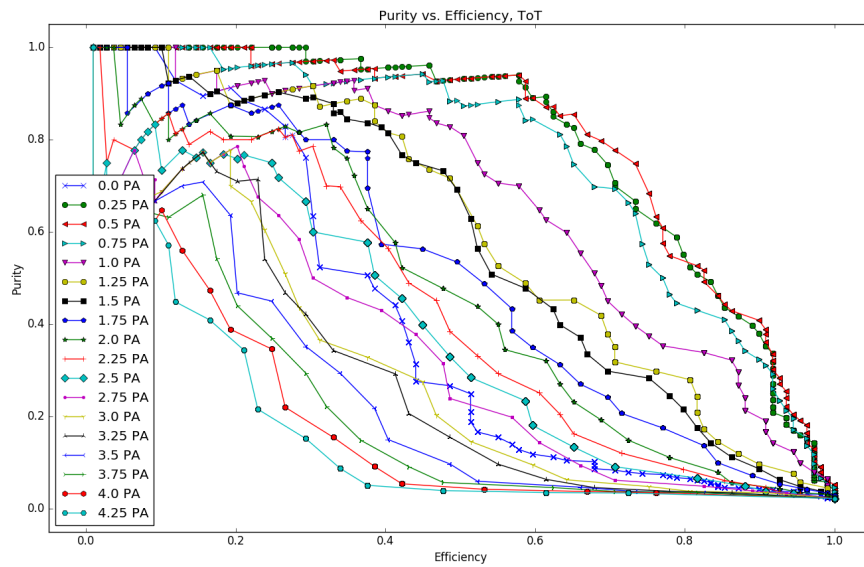
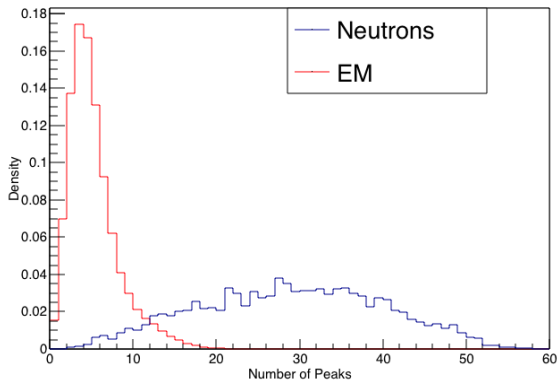
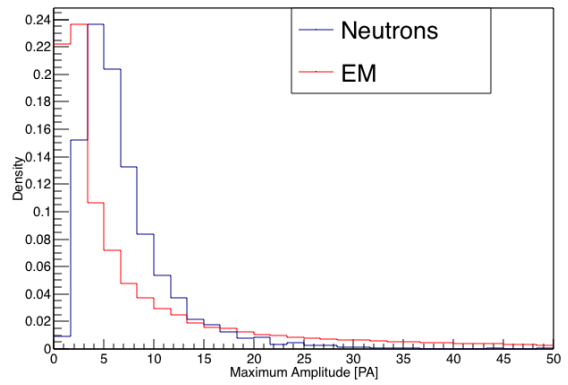


Figure 5.14: Line plot for Time-over-Threshold feature tuning.



(a) Number-of-Peaks.



(b) Maximum Amplitude.

Figure 5.15: Histograms for the number-of-peak (a) and for the maximum amplitude (b) values on the test data. Neutron signals and photon/dark count signals are clearly distinguishable, in contrast, the maximum amplitude feature values overlap for the most part.

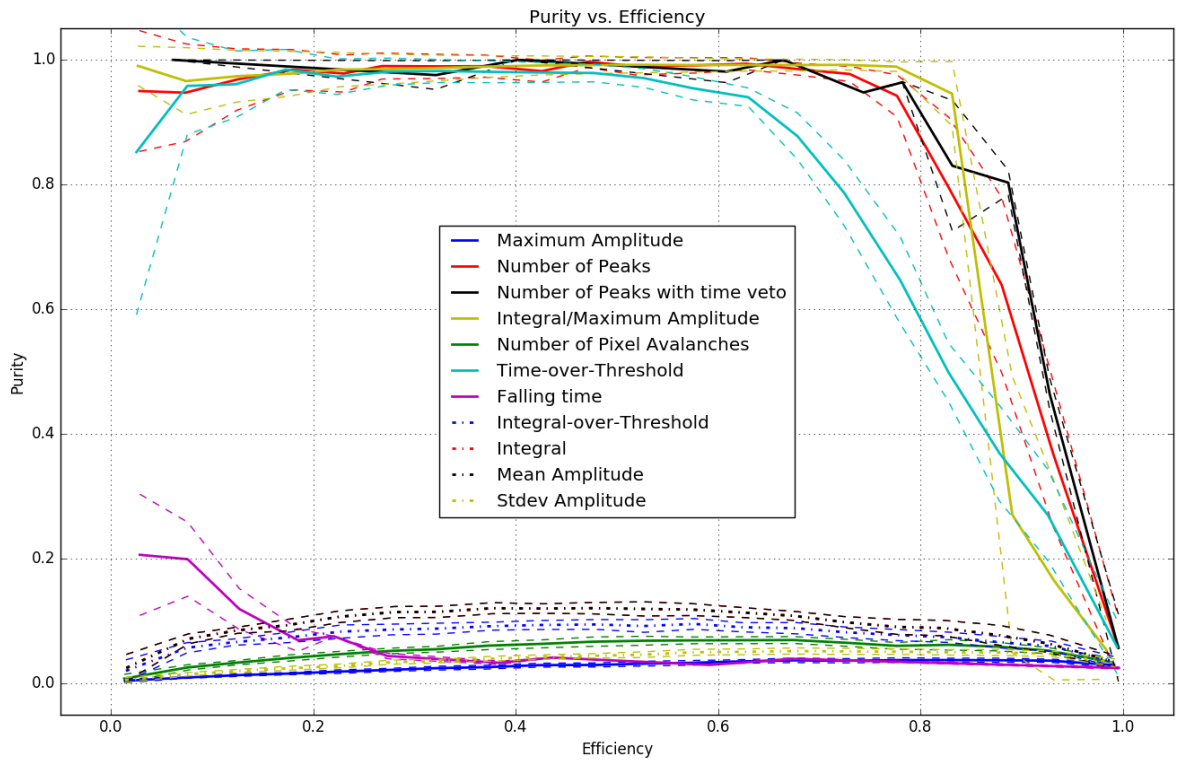


Figure 5.16: Results for feature evaluation on the purity-efficiency plane.

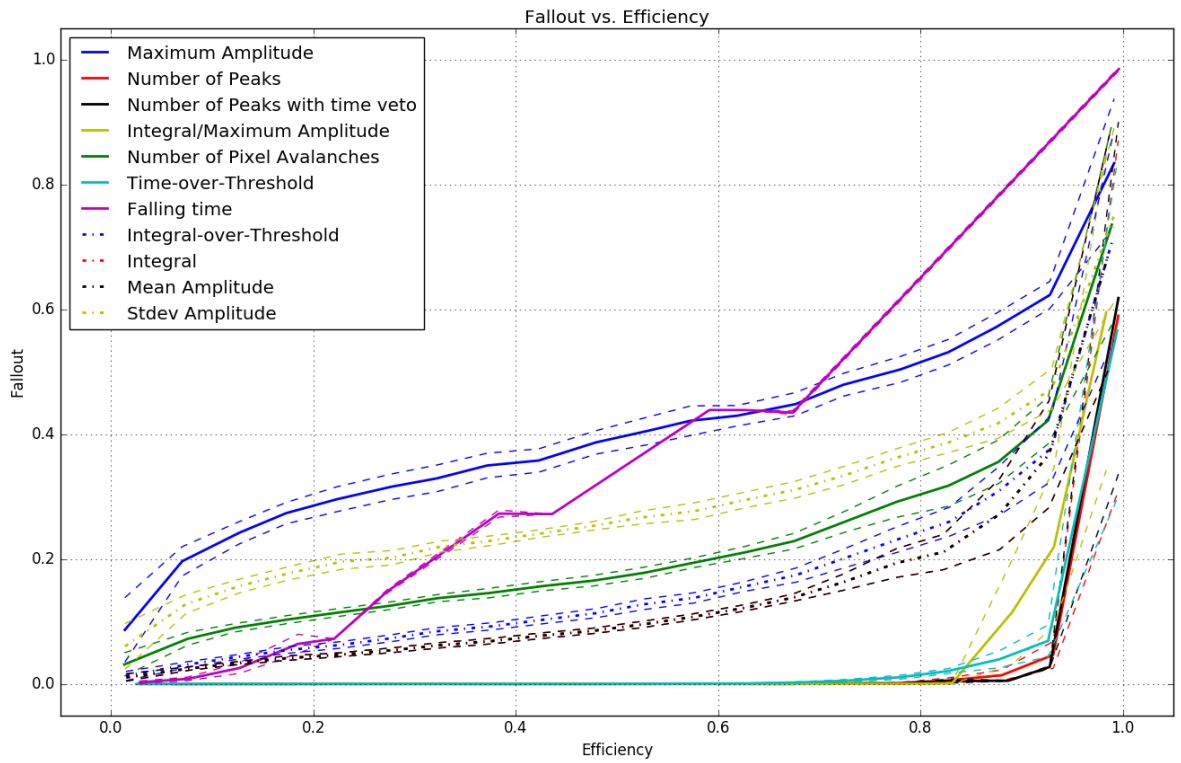


Figure 5.17: Results for feature evaluation on the purity-fake rate (false positive rate, fallout) plane. The ROC curve summarising fewer algorithms is shown in figure 6.1.

The results on the purity-efficiency plane are shown in figure 5.16, and those on the fake rate-efficiency plane are shown in figure 5.17, with the corresponding 1σ level (the ROC curve is shown in the conclusions section in figure 6.1). Results have been obtained on the same channel, but on 4 different data subsets.

The analysis on the final results allow to reduce the features to be considered to those performing well:

- Number-of-Peaks (with and without time veto),
- Time-over-Threshold, and
- Integral-over-Amplitude.

At 10% fake rate, efficiency is above 90% efficiency for these features, and efficiency is held above 65% – and even above $\sim 90\%$ without the Time-over-Threshold feature – for purity above 90%.

5.4.3 Machine Learning Algorithms

	ToT	nPeaks	weighted	maxA	int/maxA	Perceptr
ToT	1.00	0.90	0.87	0.86	0.60	0.82
nPeaks	0.90	1.00	0.73	0.71	0.62	0.87
weighted	0.87	0.73	1.00	0.99	0.45	0.73
maxA	0.86	0.71	0.99	1.00	0.43	0.61
int/maxA	0.60	0.62	0.45	0.43	1.00	0.92
Perceptr	0.82	0.87	0.73	0.61	0.92	1.00

Table 5.3: Correlation matrix for selected features and the perceptron on both neutrons and non-neutrons. Dark red indicates highest, white lowest correlation ($p = 1$, $p = 0$). *ToT*: Time-over-Threshold. *nPeaks*: Number-of-Peaks. *weighted*: Weighted Number-of-Peaks = Number of Photon Avalanches. *maxA*: Maximum Amplitude. *int/maxA*: Integral-over-Amplitude. *Perceptr*: Perceptron.

Correlations The more correlated features are and the worse they perform, the less information is gained by using a combination of different features. The decision whether or not one or several features are used is based on correlation between features and their individual performance. For correlation analysis, Pearson’s r , defined as [139]

$$r = \frac{\sum_{i=1}^n (x_i - \bar{x})(y_i - \bar{y})}{\sqrt{\sum_{i=1}^n (x_i - \bar{x})^2} \sqrt{\sum_{i=1}^n (y_i - \bar{y})^2}} = \frac{\text{cov}(X, Y)}{\sigma_X \sigma_Y} \quad (5.62)$$

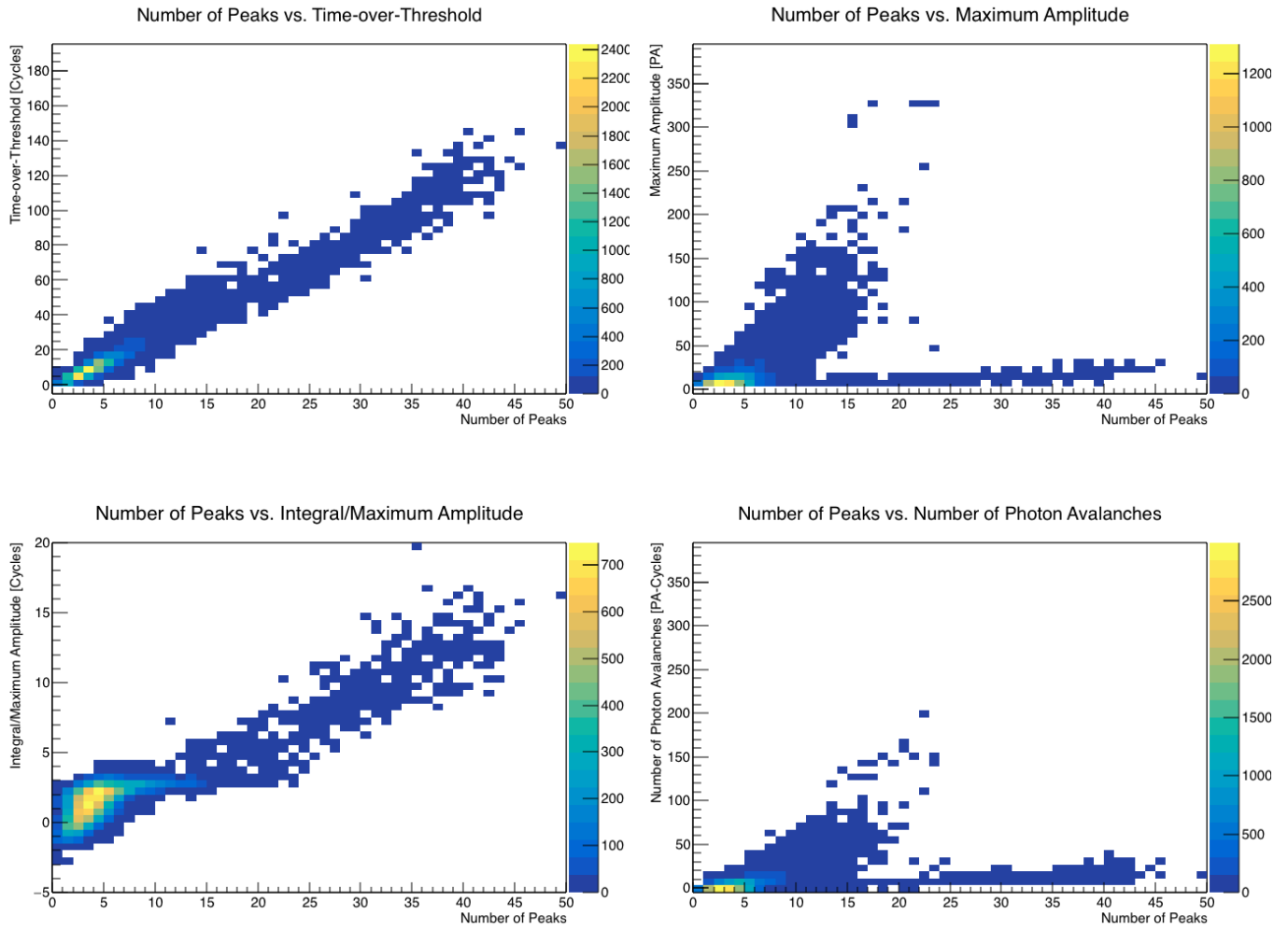


Figure 5.18: Two-dimensional histograms indicating correlation for both neutrons and non-neutrons between different features.

for data sets $X = \{x_1, x_2, \dots, x_n\}, Y = \{y_1, y_2, \dots, y_n\}$ is commonly used to indicate correlation. Results of the correlation analysis, mostly on features with good performance, on the data set including both neutrons and non-neutrons can be seen in table 5.3, with some of the corresponding two-dimensional histograms shown in figure 5.18. The correlation analysis has also been undertaken on data sets consisting only of neutrons and only of non-neutrons. The features examined are correlated to a very high degree, except the Integral-over-Amplitude, indicating that redundant information would be obtained when using more than one feature. From the results it can be concluded that no significant increase of performance can be expected when using more than one feature that is not the Integral-over-Amplitude feature. In section 5.5 it will be shown why the Integral-over-Amplitude feature cannot be used on the firmware-level trigger.

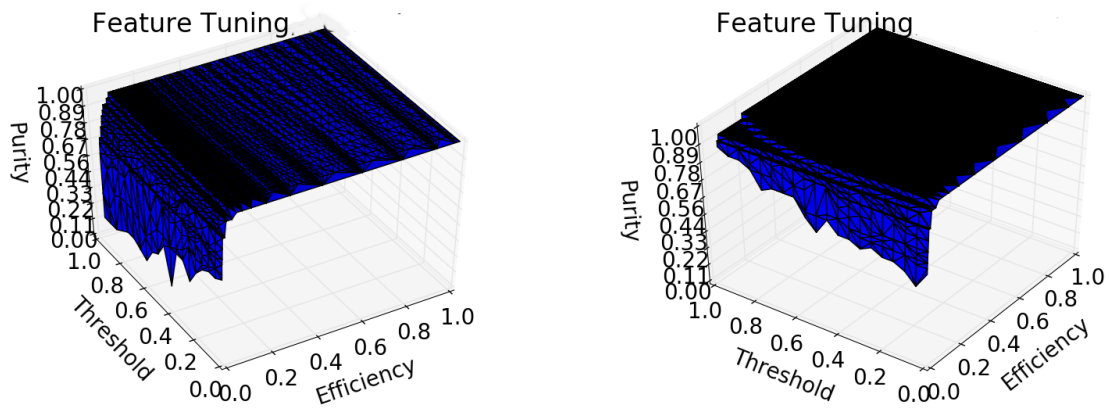
Perceptron Correlation analysis suggests that using a perceptron does not yield much better performance as information of different features are redundant. However, the perceptron has been evaluated using a normalised two input-node setup (one with Number-of-Peaks and Time-over-Threshold as inputs, one with Number-of-Peaks and Integral-over-Amplitude), in order to have only one parameter to sweep, w_1 . With the weight vector defined as $\mathbf{w} = (w_1, 1 - w_1)$, the parameter sweep shows clearly that changes in performance by using the perceptron are tiny (see figure 5.19).

Feed-Forward Neural Network The same conclusions as for the perceptron hold for the feed-forward neural network: Since features are highly redundant, only a tiny amount of information is gained. A two-layer two-input feed-forward neural network with Number-of-Peaks and Time-over-Threshold as input has been benchmarked, with the weight matrix (as in equation 5.61)

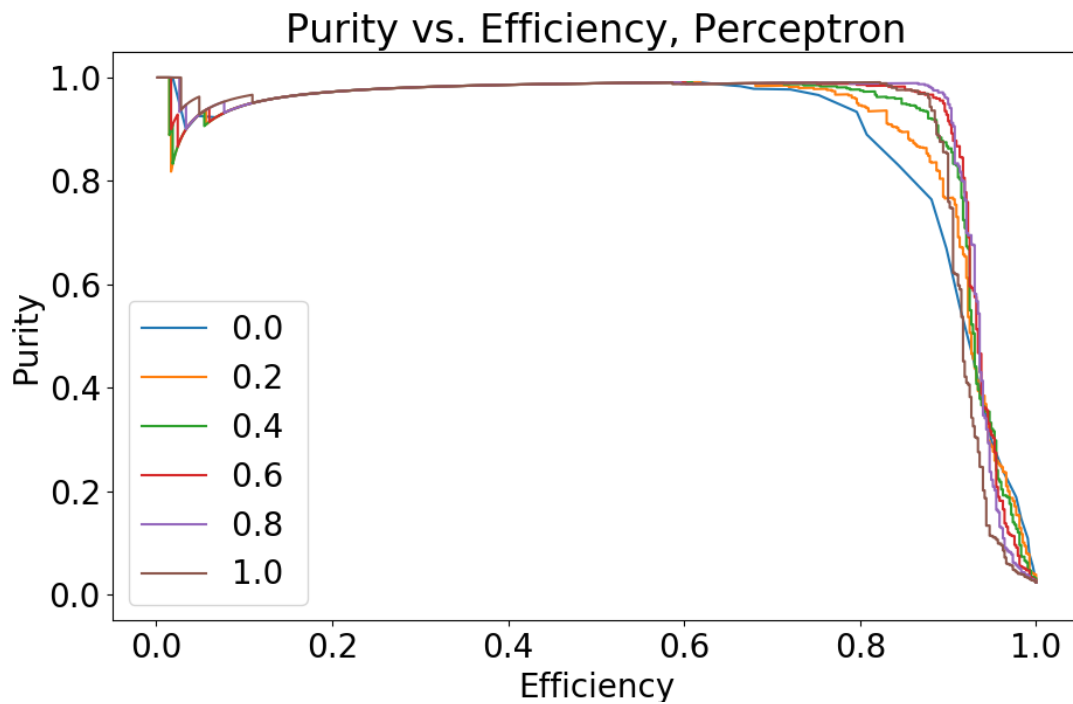
$$\mathbf{w} = \begin{pmatrix} w_1 & w_2 \\ 1 - w_1 & 1 - w_2 \end{pmatrix} \quad (5.63)$$

with two free parameters w_1, w_2 , resulting in the confirmation of the assumption that no significant increase in classification performance is achieved (see figures 5.20). For the ANN, no advanced training method has been used, as the number of free parameters were chosen low in order to have a model that can be evaluated by parameter sweeps.

Triggering The conclusion from correlation analysis is that only one feature will be used, hence a simple binary trigger (see equation 5.25) is implemented as the classification algorithm.



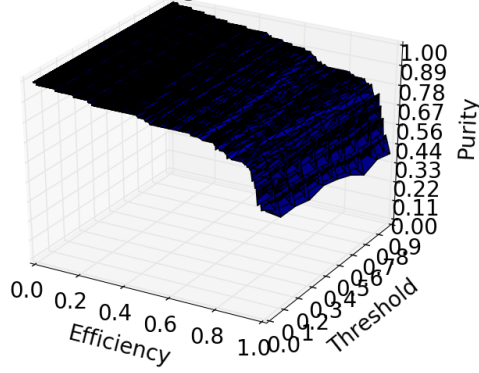
(a) Perceptron with Number-of-Peaks and Time-over-Threshold. (b) Perceptron with Number-of-Peaks and Integral-over-Amplitude.



(c) One-dimensional plot corresponding to the perceptron performance shown in 5.19b. Weight w_1 is swept from 0 (only Number-of-Peaks) to 1 (only Integral-over-Amplitude). The difference in purity between $w_1 = 1$ to the optimum at $w_1 = 0.8$ is less than 2%.

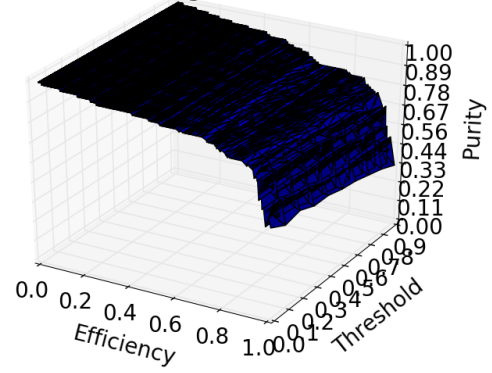
Figure 5.19: Perceptron evaluation.

Feature Tuning, Neural Network



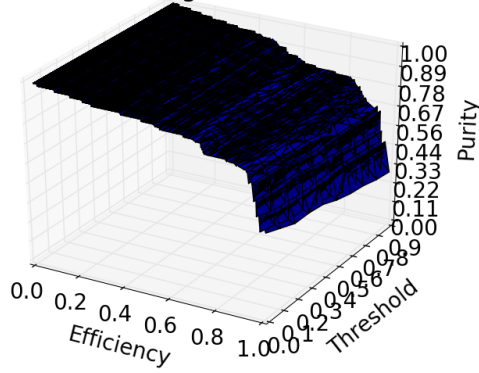
(a) Sweep of w_2 . $w_1 = 0.25$

Feature Tuning, Neural Network



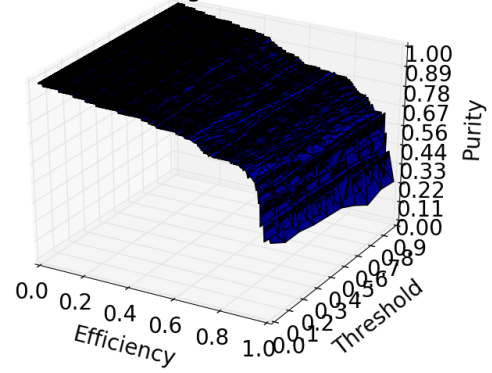
(b) Sweep of w_2 . $w_1 = 0.5$

Feature Tuning, Neural Network

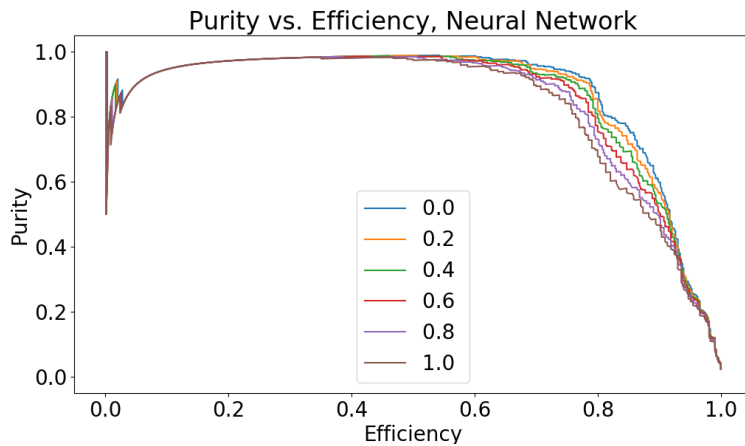


(c) Sweep of w_2 . $w_1 = 0.75$

Feature Tuning, Neural Network



(d) Sweep of w_2 . $w_1 = 1$



(e) $w_2 = 0.5$, sweep of parameter w_1 from 0 to 1. The optimum value is $w_1 = 0$, giving full weight to Number-of-Peaks.

Figure 5.20: Two-dimensional parameter sweep for a two-layer two-input (Number-of-Peaks and Time-over-Threshold) feed-forward neural network. No significant improvement in performance is achieved.

```

elsif rising_edge(clk) then
-----
-- Find Maximum --
-----
    delta :=      to_integer(unsigned(data_in))-delayed;
    delayed <=    to_integer(unsigned(data_in));
    delta_delayed<= delta;

    --Conditions
    maximum :=    (delayed > to_integer(unsigned(threshold)))AND (delta < 0) AND (delta_delayed >= 0); --//1 clock cycle
-----
-- Count Maxima --
-----
    case maximum is
        when False => maximum_start := 0;
                       shiftreg(0)  <= '0';
        when True  => maximum_start := 1;
                       shiftreg(0)  <= '1';
    end case;
    case shiftreg((2**windowlength)-2) is
        when '0' => maximum_end := 0;
        when '1' => maximum_end := 1;
    end case;

    for i in 1 to ((2**windowlength)-2) loop -- not first element
        shiftreg(i) <= shiftreg(i-1);
    end loop;

    npeaks_buf <= npeaks_buf + maximum_start - maximum_end; --//1 clock cycle
end if;
npeaks <=      std_logic_vector(to_unsigned(npeaks_buf,windowlength)); --//1 clock cycle

```

Figure 5.21: Code snipped from the VHDL Number-of-Peaks feature extraction source code.

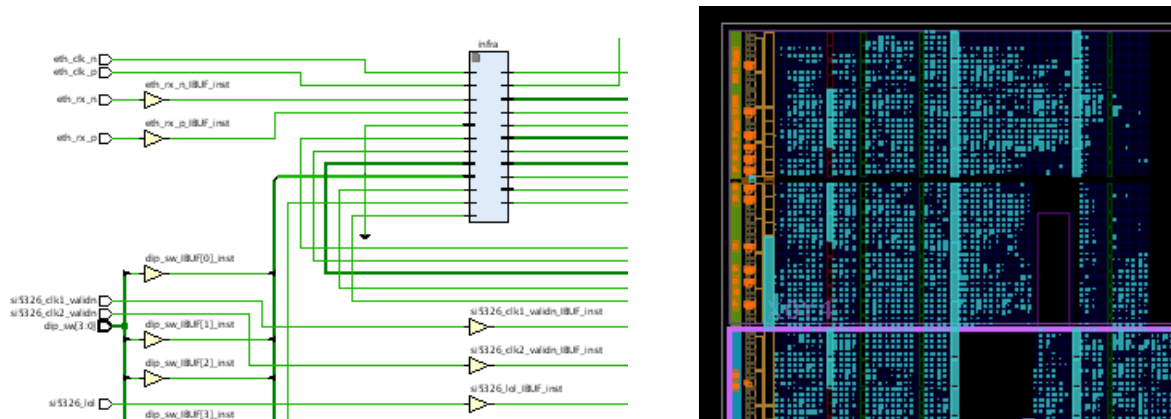
5.5 Implementation

The selected trigger algorithms are implemented via synthesis and routing from VHDL code, a hardware description language synthesisable into digital circuits [140], into the FPGA. A netlist (RTL) is generated from the HDL code input, and implementation and bitstream containing the FPGA circuit configuration is created using the netlist [141] [142]. For the toolchain, XILINX Vivado has been used for design and synthesis and MENTOR GRAPHICS Questasim for simulation and verification.

As 64 channel triggers plus the other firmware elements have to be synthesised on a single FPGA, hardware resources are strictly limited (see table 4.2). Therefore each of the algorithms has to be checked whether their resource usage fits the device’s resource availability. VHDL implementation of algorithms and their synthesis has been undertaken for the Time-over-Threshold, Number-of-Peaks (with and without time veto) and Integral-over-Amplitude features, as well as for the Integral feature. An example of an implementation workflow is shown in figures 5.21 and 5.22.

5.5.1 Resource Usage

As can be seen in equations 5.49, 5.43 and 5.45 and 5.53, the Integral, Time-over-Threshold, Number-of-Peaks features rely on comparators, sums and differences only, as integrals will turn to sums in discretisation, and



(a) Part of the RTL netlist generated from the VHDL code. (b) Snippet of the implementation of the RTL onto an Artix-7 FPGA.

Figure 5.22: From the code, an RTL netlist is generated (a) that is then implemented into FPGA (b).

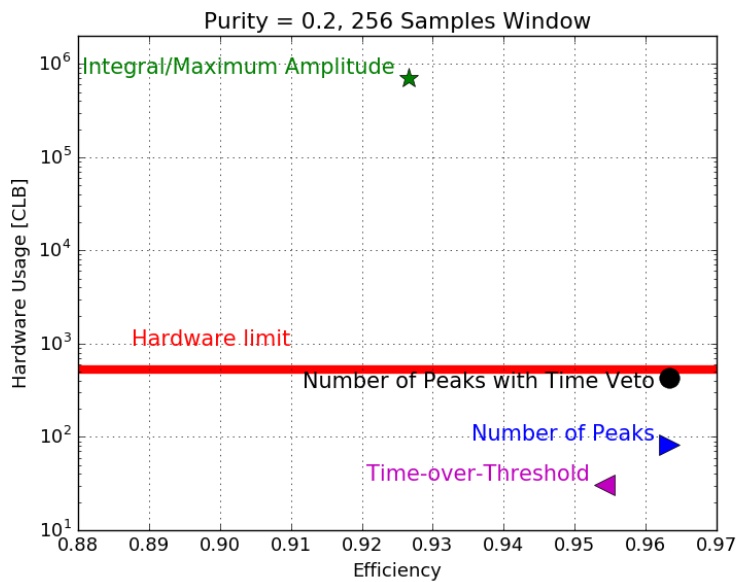


Figure 5.23: Hardware usage of different feature extraction algorithms versus efficiency at a 20% purity level and on a window size of 256 samples. The red line indicates hardware resource availability per channel.

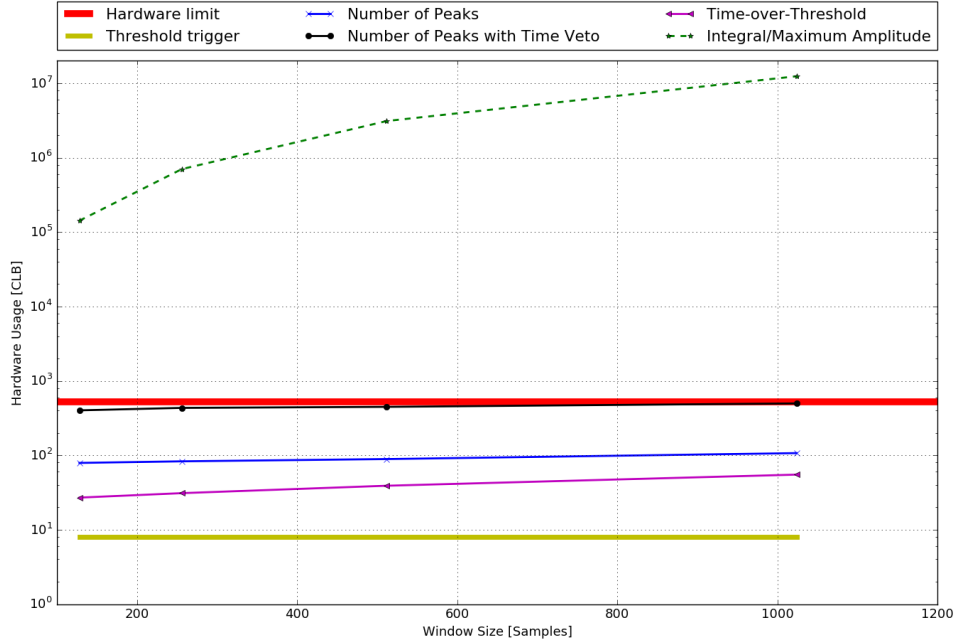


Figure 5.24: Hardware usage of different feature extraction algorithms versus time window size. The expected window size is 256 samples. The red line indicates hardware availability per channel.

differentials will turn to differences. Sums and differences can be easily implemented as adder-subtractors into digital logic [143]. However, the Integral-over-Amplitude algorithm contains a division, as can be seen in equation 5.55, an operation that is resource-intense on the FPGA. The usage of hardware resources is compared in figure 5.23 as a function of efficiency at a 20% purity level and in figure 5.24 as a function of window size. It can be seen that the Integral-over-Amplitude algorithm exceeds the hardware limit by far. The time veto-version of the Number-of-Peaks algorithms approaches the limit of what is implementable. Despite it is the best-performing feature, it has been dropped because of this issue, namely in consideration to the logic used for other functions of the FPGA.

The Number-of-Peaks algorithm has been tested both in the variation of equation 5.43 (using the zero crossing of the differential signal) and 5.45 (using amplitude comparison only), and the exact same logic usage has been determined for both algorithms. As both lead to the same results, performance stays the same for both variants.

Therefore, implementation into the firmware has been made for the Number-of-Peaks algorithm according to equation 5.43 without time veto, and the Time-over-Threshold feature extraction method.

Algorithm	Number of Channels	Current [A]	Power consumption [W]
Number-of-Peaks	2	1.31	
Number-of-Peaks	4	1.32	
Number-of-Peaks	6	1.33	
Number-of-Peaks	8	1.33	
Number-of-Peaks	10	1.34	
Number-of-Peaks	12	1.35	
Time-over-Threshold	2	1.48	
Time-over-Threshold	4	1.49	
Time-over-Threshold	6	1.49	
Time-over-Threshold	8	1.50	
Time-over-Threshold	10	1.51	
Time-over-Threshold	12	1.51	
Number-of-Peaks	1 (extrapolated)	0.007	
Time-over-Threshold	1 (extrapolated)	0.005	
Number-of-Peaks	64 (extrapolated)	1.72	8.6
Time-over-Threshold	64 (extrapolated)	1.79	9.0

Table 5.4: Current and power consumption for the trigger algorithms for different number of channels.

	Efficiency [%]	Purity [%]
Channel 0	96.2	20.4
Channel 0 \vee Channel 1	97.6	12.3
Channel 0 \wedge Channel 1	93.8	55.5

Table 5.5: Efficiency and purity values on Number-of-Peaks feature for the same threshold value and data set. In this example, by using logical conjunction, a small drop in efficiency is contrasted by a high increase in purity.

5.5.2 Power Consumption

Power consumption is limited to 12W by the DC-DC converter on the TRENZ module [144]. Therefore it has to be verified that FPGA power consumption meets the requirements. The full firmware including other firmware components has been synthesised in multiple variants, from 2 to 12 channels (the maximum number of channels that were available at the time of measurement), and the consumed power has been extrapolated to a single and to 64 channels. The results are shown in table 5.4, according to which power consumption should meet the requirements set by the DC-DC converter. However some uncertainty exists depending on the increase of power consumption when in operation.

5.6 Plane-level Trigger

The implemented trigger is a per-channel trigger. It decides on a rolling basis whether in the past m samples a neutron event has possibly occurred. If so, the block is tagged as trigger-positive and this decision forwarded to the plane-level trigger.

At the moment, a trigger on each channel causes a read-out, or in other words, the 64 channel triggers are logically disjunct ($\vee = \text{OR}$, [145]):

$$\hat{\mathbf{y}}_{\text{plane}} = \bigvee_{i=1}^{64} \hat{\mathbf{Y}}_i. \quad (5.64)$$

Several other logical connections can be implemented, such as the logical conjunction ($\wedge = \text{AND}$, [145]) of fibres in the same cube (two on the x and two on the y axis):

$$\hat{\mathbf{y}}_{\text{plane}} = \left(\bigvee_{i=1}^{16} \bigwedge_{j=2i-1}^{2i} \hat{\mathbf{Y}}_j \right) \wedge \left(\bigvee_{i=33}^{48} \bigwedge_{j=2i-1}^{2i} \hat{\mathbf{Y}}_j \right). \quad (5.65)$$

As only two channels on the same cube have been available on the test data, changes in performance has been evaluated using just these two highly correlated data sets. Results presented in table 5.5 show that, in the present example, when using logical conjunction instead of logical disjunction, a small drop in efficiency contrasts a high increase in purity, making this logical linking advisable for implementation on the plane level.

6 Conclusion

In order to define the channel firmware trigger, various feature extraction and machine learning algorithms have been evaluated. This includes a variety of feature extraction approaches, and a threshold trigger and two sorts of neural networks on the machine learning side. According to the findings, the most suitable trigger has been implemented, that are now the Number-of-Peaks and the Time-over-Threshold feature extraction algorithms (see summarising figure 6.1) and a threshold trigger on the feature extraction output value. These algorithms have been implemented and synthesised into firmware, and embedded into the *IPbus* framework. The commissioning of the trigger is still to come, and the surrounding software and firmware have to be made ready to write to the trigger parameter registers.

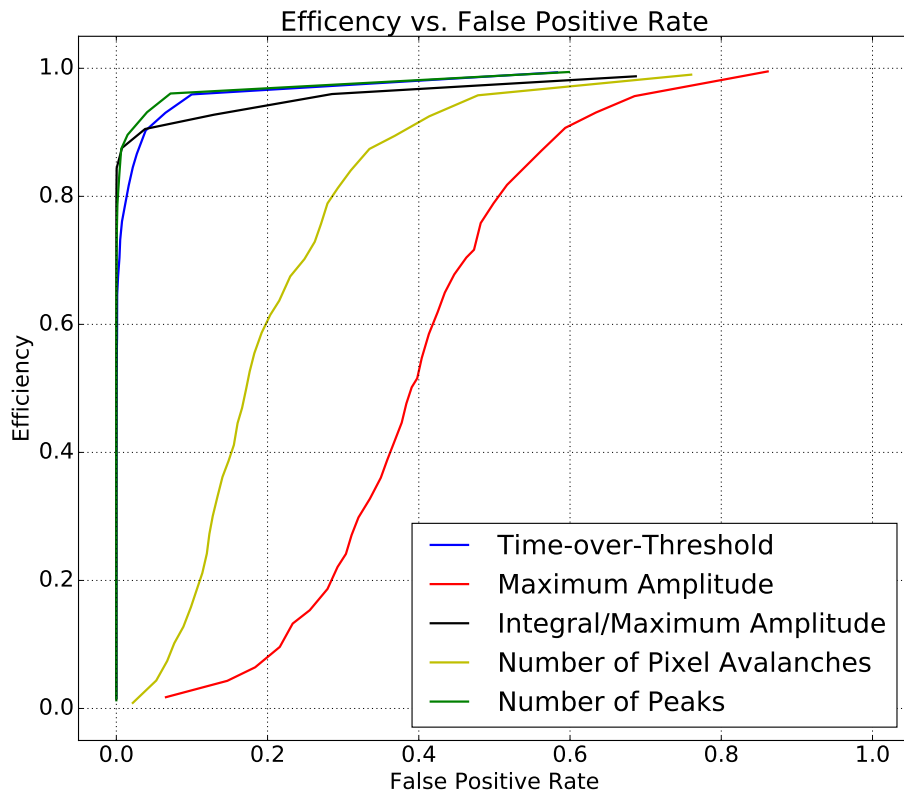


Figure 6.1: Summarising ROC curve of different features in terms of efficiency (TPR) and fake rate (fallout, FPR), with the Number-of-Peaks algorithm performing best on the test data set.

The trigger performance evaluation was carried out relative to the test data, and conditions at the reactor are not known at the moment. Therefore the decision on the trigger algorithm relies on the assumption that

the best performing algorithms on the test environment also perform well on the reactor site. However this might be wrong if background signals are qualitatively different from the test signals. This can be considered unlikely though, as the same detection scheme underlies both setups. The actual background rate determines at which efficiency level the trigger can operate. The tuning of the parameters for the trigger is performed at **calibration**. Calibration will aim not only for highest efficiency, but also for uniformity along the different channels. As trigger efficiency directly propagates to detector efficiency, optimal trigger calibration is essential for the quality of the experiment.

The hunt for sterile neutrinos in the very-short baseline range has started, and SoLid is about to start its first large-scale physics run. Whether or not the reactor anomaly – the deficit of neutrinos in the short-baseline range of neutrinos – can be reproduced very close to the reactor core is crucial in deciding the fate of the three-neutrino oscillation model. In the case the reactor anomaly cannot be reconfirmed, the results would fit nicely not only with the three-flavour neutrino oscillation model, but also with recent results from accelerator- and atmospheric-based neutrino experiments. In case SoLid, in line with other very short-baseline experiments, does find a deficit, a theorist has to seriously consider an update of the neutrino model currently most favoured, from having three to having four or even more neutrino flavour states by adding sterile neutrinos.

7 References

- [1] K.A. Olive et al. Review of Particle Physics. *Chin. Phys.*, C38:090001, 2014.
- [2] P. Langacker. Introduction to the Standard Model and Electroweak Physics. In *Proceedings of Theoretical Advanced Study Institute in Elementary Particle Physics on The dawn of the LHC era (TASI 2008)*, Boulder, USA, 2-27 Jun, 2008.
- [3] M. Herrero. The Standard model. *NATO Sci. Ser. C*, 534:1–59, 1999.
- [4] Y. Fukuda et al. Measurements of the solar neutrino flux from Super-Kamiokande’s first 300 days. *Phys. Rev. Lett.*, 81:1158–1162, 1998. [Erratum: *Phys. Rev. Lett.*81,4279(1998)].
- [5] J. Zhang and S. Zhou. Relic Right-handed Dirac Neutrinos and Implications for Detection of Cosmic Neutrino Background. *Nucl. Phys.*, B903:211–225, 2016.
- [6] P. Lipari. Introduction to neutrino physics. In *2001 CERN-CLAF School of High-Energy Physics, Itacuruca, Brazil, 6-19 May*, pages 115–199, 2001.
- [7] A. Dobrynina, A. Kartavtsev, and G. Raffelt. Helicity oscillations of Dirac and Majorana neutrinos. *Phys. Rev.*, D93(12):125030, 2016.
- [8] M. Goldhaber, L. Grodzins, and A.W. Sunyar. Helicity of Neutrinos. *Phys. Rev.*, 109:1015–1017, 1958.
- [9] S.F. King. Neutrino Mass Models: A Road map. *J. Phys. Conf. Ser.*, 136:022038, 2008.
- [10] B. Pontecorvo. Neutrino Experiments and the Problem of Conservation of Leptonic Charge. *Sov. Phys. JETP*, 26:984–988, 1968. [*Zh. Eksp. Teor. Fiz.*53,1717(1967)].
- [11] Q.R. Ahmad et al. Direct evidence for neutrino flavor transformation from neutral current interactions in the Sudbury Neutrino Observatory. *Phys. Rev. Lett.*, 89:011301, 2002.
- [12] Y. Fukuda et al. Evidence for oscillation of atmospheric neutrinos. *Phys. Rev. Lett.*, 81:1562–1567, 1998.
- [13] Z. Maki, M. Nakagawa, and S. Sakata. Remarks on the unified model of elementary particles. *Prog. Theor. Phys.*, 28:870–880, 1962.
- [14] M. Kobayashi and T. Maskawa. CP Violation in the Renormalizable Theory of Weak Interaction. *Prog. Theor. Phys.*, 49:652–657, 1973.

- [15] S. Eidelman, K.G. Hayes, K.A. Olive, et al. Review of particle physics. *Physics Letters B*, 592(1):1 – 5, 2004.
- [16] M. Czakon, M. Zralek, and J. Gluza. Are neutrinos Dirac or Majorana particles? *Acta Phys. Polon.*, B30:3121–3138, 1999.
- [17] Z.Z. Xing. Neutrino masses & flavor mixing. In *48. Internationale Universitätswochen für Theoretische Physik, Schladming, Austria, 27 Feb-6 Mar*, 2010.
- [18] C. Patrignani et al. Review of Particle Physics. *Chin. Phys.*, C40(10):100001, 2016.
- [19] F. Capozzi, E. Lisi, A. Marrone, D. Montanino, and A. Palazzo. Neutrino masses and mixings: Status of known and unknown 3ν parameters. *Nuclear Physics B*, 908:218 – 234, 2016. Neutrino Oscillations: Celebrating the Nobel Prize in Physics 2015.
- [20] C. Giunti and C.W. Kim. *Fundamentals of Neutrino Physics and Astrophysics*. Oxford University Press, 2007.
- [21] J. Kopp. *Phenomenology of Three-Flavour Neutrino Oscillations*. PhD thesis, Technische Universität München, 2006.
- [22] J.N. Abdurashitov et al. Measurement of the solar neutrino capture rate with gallium metal. III: Results for the 2002–2007 data-taking period. *Phys. Rev.*, C80:015807, 2009.
- [23] M. Altmann et al. Complete results for five years of GNO solar neutrino observations. *Phys. Lett.*, B616:174–190, 2005.
- [24] K. Eguchi et al. First results from KamLAND: Evidence for reactor anti-neutrino disappearance. *Phys. Rev. Lett.*, 90:021802, 2003.
- [25] M.H. Ahn et al. Measurement of Neutrino Oscillation by the K2K Experiment. *Phys. Rev.*, D74:072003, 2006.
- [26] P. Adamson et al. Measurement of Neutrino and Antineutrino Oscillations Using Beam and Atmospheric Data in MINOS. *Phys. Rev. Lett.*, 110(25):251801, 2013.
- [27] K. Abe et al. First Muon-Neutrino Disappearance Study with an Off-Axis Beam. *Phys. Rev.*, D85:031103, 2012.

- [28] K. Abe et al. Evidence for the Appearance of Atmospheric Tau Neutrinos in Super-Kamiokande. *Phys. Rev. Lett.*, 110(18):181802, 2013.
- [29] N. Agafonova et al. Discovery of τ Neutrino Appearance in the CNGS Neutrino Beam with the OPERA Experiment. *Phys. Rev. Lett.*, 115(12):121802, 2015.
- [30] Y. Abreu, Y. Amhis, L. Arnold, et al. A novel segmented-scintillator antineutrino detector. *JINST*, 12(04):P04024, 2017.
- [31] L. Arnold, W. Beaumont, D. Cussans, D. Newbold, N. Ryder, and A. Weber. The SoLid anti-neutrino detector’s readout system. *JINST*, 12(02):C02012, 2017.
- [32] G. Boireau et al. Online Monitoring of the Osiris Reactor with the Nucifer Neutrino Detector. *Phys. Rev.*, D93(11):112006, 2016.
- [33] A.V. Derbin, A.S. Kayunov, and V.N. Muratova. Search for Neutrino Oscillations at a Research Reactor. 2012.
- [34] D. Lhuillier. Future Short-Baseline Sterile Neutrino Searches with Reactors. In *XXVI International Conference on Neutrino Physics and Astrophysics (Neutrino 2014)*, Boston, USA, 2-7 Jul, 2014.
- [35] J. Haser. Search for eV sterile neutrinos at a nuclear reactor — the Stereo project. *J. Phys. Conf. Ser.*, 718(6):062023, 2016.
- [36] A. Serebrov et al. On possibility of realization NEUTRINO-4 experiment on search for oscillations of the reactor antineutrino into a sterile state. 2013.
- [37] A. Serebrov et al. Experiment for search for sterile neutrino at SM-3 reactor. *Phys. Part. Nucl.*, 47(6):1014–1023, 2016.
- [38] I.S. Yeo et al. Development of a gadolinium-loaded liquid scintillator for the Hanaro short baseline prototype detector. *J. Korean Phys. Soc.*, 64(3):377–381, 2014.
- [39] I. Alekseev et al. DANSS: Detector of the reactor AntiNeutrino based on Solid Scintillator. *JINST*, 11(11):P11011, 2016.
- [40] J. Ashenfelter et al. PROSPECT - A Precision Reactor Oscillation and Spectrum Experiment at Short Baselines. In *Proceedings, Community Summer Study 2013: Snowmass on the Mississippi (CSS2013)*, Minneapolis, MN, USA, 29 Jul-6 Aug, 2013.

- [41] C. Lane et al. A new type of Neutrino Detector for Sterile Neutrino Search at Nuclear Reactors and Nuclear Nonproliferation Applications. 2015.
- [42] Y. Abe et al. Indication for the disappearance of reactor electron antineutrinos in the Double Chooz experiment. *Phys. Rev. Lett.*, 108:131801, 2012.
- [43] Z. Wang. Highlights from the Daya Bay Neutrino Experiment. *EPJ Web Conf.*, 71:00138, 2014.
- [44] J.K. Ahn et al. Observation of Reactor Electron Antineutrino Disappearance in the RENO Experiment. *Phys. Rev. Lett.*, 108:191802, 2012.
- [45] T. Lasserre and H.W. Sobel. Reactor neutrinos. *Comptes Rendus Physique*, 6:749–757, 2005.
- [46] G. Gratta. Neutrino oscillation experiments at nuclear reactors. *Nucl. Phys. Proc. Suppl.*, 85:72–77, 2000.
- [47] J. Shirai. Reactor neutrinos and KamLAND. In *Particle physics at the year of 250th anniversary of Moscow University. Proceedings, 12th Lomonosov Conference on elementary particle physics, Moscow, Russia, 25-31 Aug*, pages 29–36, 2005.
- [48] L. Di Lella. Accelerator and reactor neutrino experiments. *Int. J. Mod. Phys.*, A15S1:257–282, 2000. [,257(1999)].
- [49] M. Nieto, A. Hayes, C. Teeter, W. Wilson, and W. Stanbro. Detection of anti-neutrinos for nonproliferation. 2003.
- [50] A.C. Hayes and P. Vogel. Reactor Neutrino Spectra. *Ann. Rev. Nucl. Part. Sci.*, 66:219–244, 2016.
- [51] J. Cao. Determining Reactor Neutrino Flux. *Nucl. Phys. Proc. Suppl.*, 229-232:205–209, 2012.
- [52] T.A. Mueller, D. Lhuillier, M. Fallot, A. Letourneau, S. Cormon, M. Fechner, L. Giot, T. Lasserre, J. Martino, G. Mention, A. Porta, and F. Yermia. Improved Predictions of Reactor Antineutrino Spectra. *Phys. Rev.*, C83:054615, 2011.
- [53] G. Mention, M. Fechner, T. Lasserre, T.A. Mueller, D. Lhuillier, M. Cribier, and A. Letourneau. The Reactor Antineutrino Anomaly. *Phys. Rev.*, D83:073006, 2011.
- [54] S. Gariazzo. Light sterile neutrinos and pseudoscalar interactions in cosmology. In *Neutrino Oscillation Workshop (NOW) 2016, Otranto, Italy, 5-10 Sep*, 2016.

- [55] Y. Abe et al. Improved measurements of the neutrino mixing angle θ_{13} with the Double Chooz detector. *JHEP*, 10:086, 2014. [Erratum: *JHEP*02,074(2015)].
- [56] S.B. Kim. New results from RENO and prospects with RENO-50. *Nucl. Part. Phys. Proc.*, 265-266:93–98, 2015.
- [57] F.P. An. Measurement of the Reactor Antineutrino Flux and Spectrum at Daya Bay. *Phys. Rev. Lett.*, 116:061801, Feb 2016.
- [58] F. Kaether, W. Hampel, G. Heusser, J. Kiko, and T. Kirsten. Reanalysis of the GALLEX solar neutrino flux and source experiments. *Phys. Lett.*, B685:47–54, 2010.
- [59] C. Giunti and M. Laveder. Statistical Significance of the Gallium Anomaly. *Phys. Rev.*, C83:065504, 2011.
- [60] J. Kopp, P.A.N. Machado, M. Maltoni, and Th. Schwetz. Sterile Neutrino Oscillations: The Global Picture. *JHEP*, 05:050, 2013.
- [61] A.A. Aguilar et al. Unexplained Excess of Electronlike Events from a 1-GeV Neutrino Beam. *Phys. Rev. Lett.*, 102:101802, Mar 2009.
- [62] A.A. Aguilar et al. Improved Search for $\bar{\nu}_\mu \rightarrow \bar{\nu}_e$ Oscillations in the MiniBooNE Experiment. *Phys. Rev. Lett.*, 110:161801, Apr 2013.
- [63] B. Armbruster et al. Upper limits for neutrino oscillations $\bar{\nu}_\mu \rightarrow \bar{\nu}_e$ from muon decay at rest. *Phys. Rev. D*, 65:112001, Jun 2002.
- [64] F. Dydak et al. A Search for Muon-neutrino Oscillations in the Δm^2 Range 0.3eV^2 to 90eV^2 . *Phys. Lett.*, B134:281, 1984.
- [65] P. Adamson et al. Active to sterile neutrino mixing limits from neutral-current interactions in MINOS. *Phys. Rev. Lett.*, 107:011802, 2011.
- [66] N. Agafonova et al. Search for $\nu_\mu \rightarrow \nu_e$ oscillations with the OPERA experiment in the CNGS beam. *Journal of High Energy Physics*, 2013(7):4, 2013.
- [67] M. Antonello et al. Experimental search for the “LSND anomaly” with the ICARUS detector in the CNGS neutrino beam. *Eur. Phys. J.*, C73(3):2345, 2013.

- [68] J. Beringer et al. Review of particle physics. *Phys. Rev. D*, 86:010001, Jul 2012.
- [69] H.W. Ke, J.H. Zhou, Sh. Chen, T. Liu, and X.Q. Li. The hidden symmetries in the PMNS matrix and the light sterile neutrino(s). *Mod. Phys. Lett.*, A30(27):1550136, 2015.
- [70] S. K. Kang, Y. D. Kim, Y. Ko, and K. Siyeon. Sterile neutrino analysis of reactor-neutrino oscillation. 2013.
- [71] C. Giunti and M. Laveder. 3+1 and 3+2 Sterile Neutrino Fits. *Phys. Rev.*, D84:073008, 2011.
- [72] G. H. Collin, C. A. Argüelles, J. M. Conrad, and M. H. Shaevitz. Sterile Neutrino Fits to Short Baseline Data. *Nucl. Phys.*, B908:354–365, 2016.
- [73] W. Van de Pontseele. Characterisation and modelling of correlated noise in silicon photomultipliers for the SoLid experiment. Master’s thesis, Universiteit Gent, 2016.
- [74] A. Gando et al. White paper: CeLAND - Investigation of the reactor antineutrino anomaly with an intense $^{144}\text{Ce} - ^{144}\text{Pr}$ antineutrino source in KamLAND. 2013.
- [75] F.P. An et al. Observation of electron-antineutrino disappearance at Daya Bay. *Phys. Rev. Lett.*, 108:171803, 2012.
- [76] J.H. Choi et al. Observation of energy and baseline dependent reactor antineutrino disappearance in the RENO experiment. *Phys. Rev. Lett.*, 116:211801, May 2016.
- [77] E. Christensen, P. Huber, P. Jaffke, and T.E. Shea. Antineutrino Monitoring for Heavy Water Reactors. *Phys. Rev. Lett.*, 113(4):042503, 2014.
- [78] M. Cribier. Neutrinos and non-proliferation in Europe. *Earth Moon Planets*, 99:331–341, 2006. [,331(2007)].
- [79] F. Joppen, E. Koonen, and S. Van Dijk. Periodic safety review of the BR2 reactor. In *International Conference on Research Reactors: Safe Management and Effective Utilization, Rabat, Morocco, 14-18 Nov, 2011*.
- [80] Y. Abreu. SoLid: An innovative antineutrino detector for searching oscillations at the SCK•CEN BR2 reactor (talk). In *The 14th Vienna Conference on Instrumentation, Austria, 16 Feb, 2016*.
- [81] I. Michiels. SoLid: Search for Oscillation with a ^6Li Detector at the BR2 research reactor. In *NuPhys2015: Prospects in Neutrino Physics (NuPhys) London, UK, 16-18 Dec, 2015*.

- [82] S. Kalcheva, M. Fallot, and L. Giot. Recent efforts for the BR2 reactor simulation and anti-neutrino spectrum. In *SoLid meeting, London, UK, 25 May, 2016*.
- [83] F. Boehm. Studies of neutrino oscillations at reactors. In *Current Aspects of Neutrino Physics*, 2000.
- [84] C. Bemporad, G. Gratta, and P. Vogel. Reactor based neutrino oscillation experiments. *Rev. Mod. Phys.*, 74:297, 2002.
- [85] G.S. Vidyakin, V.N. Vyrodov, I.I. Gurevich, Y.V. Kozlov, V.P. Martemyanov, S.V. Sukhotin, V.G. Tarasenkov, and S.Kh. Khakimov. Detection of Anti-neutrinos in the Flux From Two Reactors. *Sov. Phys. JETP*, 66:243–247, 1987. [Zh. Eksp. Teor. Fiz.93,424(1987)].
- [86] F. Yermia, G. Barber, J. Nash, A. Rose, A. Baird, N. Ryder, P.R. Scovell, A. Vacheret, A. Weber, S. Bouvier, J.M. Buhour, A.S. Cucuanes, M. Fallot, L. Giot, G Guilloux, B. Guillon, B. Coupé, S. Kalcheva, and E. Koonen. Search for Oscillation with Lithium-6 Detector at SCK•CEN BR2 research reactor. In *Seminar Conseil Scientifique IN2P3, Paris, France, 2013*.
- [87] C. Moortgat. Technology of the SoLid detector and construction of the first submodule. *PoS, EPS-HEP2015:080*, 2015.
- [88] I. Michiels. Investigation of the Muon Background for the NEMENIX prototype of the SoLid experiment. Master’s thesis, Universiteit Gent, 2015.
- [89] N. Ryder. First results of the deployment of a SoLid detector module at the SCK-CEN BR2 reactor. *PoS, EPS-HEP2015:071*, 2015.
- [90] M. Sweany, J. Brennan, B. Cabrera-Palmer, S. Kiff, D. Reyna, and D. Throckmorton. Above-ground antineutrino detection for nuclear reactor monitoring. *Nucl. Instrum. Meth.*, A769:37–43, 2015.
- [91] T. Schluter, W. Dunnweber, K. Dhibar, M. Faessler, R. Geyer, J.F. Rajotte, Z. Roushan, and H. Wohrmann. Large-Area Sandwich Veto Detector with WLS Fibre Readout for Hadron Spectroscopy at COMPASS. *Nucl. Instrum. Meth.*, A654:219–224, 2011.
- [92] M. Verstraeten. Optical transport in the SoLid detector. Master’s thesis, Universiteit Antwerpen, 2016.
- [93] P.H.F. Oliveira, S.T. Amancio-Filho, J.F. dos Santos, and E. Hage Jr. Preliminary study on the feasibility of friction spot welding in PMMA. *Materials Letters*, 64(19):2098 – 2101, 2010.

- [94] SAINT-GOBAIN. *Brochure Scintillating Optical Fibers*, 2014.
- [95] HAMAMATSU. *Datasheet MPPC®(multi-pixel photon counter) S12572-025, -050, -100C/P*, 2015.
- [96] P. Buzhan, B. Dolgoshein, A. Ilyin, V. Kantserov, V. Kaplin, A. Karakash, A. Pleshko, E. Popova, S. Smirnov, and Y. Volkov. An advanced study of silicon photomultiplier. *ICFA Instrum. Bull.*, 23:28–41, 2001.
- [97] V. Chmill, E. Garutti, R. Klanner, M. Nitschke, and J. Schwandt. On the characterisation of SiPMs from pulse-height spectra. *Nucl. Instrum. Meth.*, A854:70–81, 2017.
- [98] N. Otte. The Silicon Photomultiplier: A New Device for High Energy Physics, Astroparticle Physics, Industrial and Medical Applications. *eConf*, C0604032:0018, 2006.
- [99] C. Galbiati and J.F. Beacom. Measuring the cosmic ray muon-induced fast neutron spectrum by (n,p) isotope production reactions in underground detectors. *Phys. Rev.*, C72:025807, 2005. [Erratum: *Phys. Rev.*C73,049906(2006)].
- [100] B. Verreyken. Evaluating the SM1 calibration by use of radioactive sources and estimating its energy resolution for electromagnetic signals. Master’s thesis, Universiteit Antwerp, 2016.
- [101] A. Vacheret. Compact segmented antineutrino detector (talk). In *XXVII International Conference on Neutrino Physics and Astrophysics (Neutrino 2016), London, UK, 4-9 Jul, 2016*.
- [102] N. Ryder. The SoLid Experiment. In *Applied Anti-neutrino Physics, Liverpool, UK, 1 Dec, 2016*.
- [103] D. Saunders. Muon Calibration at SoLid. *PoS*, EPS-HEP2015:086, 2015.
- [104] Y. Abreu. SoLid: An innovative anti-neutrino detector for searching oscillations at the SCK•CEN BR2 reactor. *Nucl. Instrum. Meth.*, A845:467–470, 2017.
- [105] L. Arnold, L. Kalousis, M. Labare, N. Ryder, D. Saunders, and A. Vacheret. SoLid Software and Computing Infrastructure. 2016.
- [106] C. Ghabrous Larrea, K. Harder, D. Newbold, D. Sankey, A. Rose, A. Thea, and T. Williams. IPbus: a flexible Ethernet-based control system for xTCA hardware. *JINST*, 10(02):C02019, 2015.
- [107] S. Dasgupta and D. Cussans. Field Programmable Gate Arrays—Detecting Cosmic Rays. *JINST*, 10(07):C07006, 2015.

- [108] L. Arnold. Trigger for the SoLid Reactor Antineutrino Experiment. In *Prospects in Neutrino Physics (NuPhys2016)*, London, UK, 12-14 Dec, 2016.
- [109] D. Newbold. SoLid Bitbucket Wiki Entry: readout system / firmware_overview, https://bitbucket.org/solidexperiment/readout-system/wiki/firmware_overview, retrieved 20 Dec 2016, non-public, 2016.
- [110] TRENZ ELECTRONICS. Product Information "Micromodule Artix-7 XC7A200T-2C 4x5cm standard footprint (com. temp. range)", <https://shop.trenz-electronic.de/en/TE0712-02-200-2C-Micromodule-Artix-7-XC7A200T-2C-4x5cm-standard-footprint-com.-temp.-range?c=341>, retrieved 8 Jan 2017, 2016.
- [111] XILINX. *7 Series FPGAs Data Sheet: Overview v2.2*, 2016.
- [112] TRENZ ELECTRONICS. *Brochure All Programmable FPGA and SoC modules*, 2016.
- [113] L. Arnold. Irradiation Resistivity and Mitigation Measurement Design for Xilinx Kintex-7 FPGAs. Master's thesis, Fachhochschule Nordwestschweiz / University of Cambridge, 2015.
- [114] J.M. Wozencraft and I.M. Jacobs. *Principles of Communication Engineering*. Waveland Pr Inc, 1965.
- [115] R.G. Gallager. *Principles of Digital Communication*. Cambridge University Press, 2008.
- [116] R.A. Wannamaker. *The Theory of Dithered Quantization*. PhD thesis, University of Waterloo, 1997.
- [117] A. Córdoba. Dirac combs. *Letters in Mathematical Physics*, 17(3):191–196, 1989.
- [118] S.P. Lipshitz, R.A. Wannamaker, and J. Vanderkooy. Quantization and dither: A theoretical survey. *J. Audio Eng. Soc*, 40(5):355–375, 1992.
- [119] C.E. Shannon. Communication in the presence of noise. *Proc. Institute of Radio Engineers*, 37(1):10–21, 1949.
- [120] M. Hufschmid. *Information und Kommunikation. Grundlagen und Verfahren der Informationsübertragung*. Teubner, 2006.
- [121] B.P. Li. *Modern Digital and Analog Communication Systems*. Oxford University Press, 1998.
- [122] G. James, D. Witten, T. Hastie, and R. Tibshirani. *An Introduction to Statistical Learning*. Springer, 2013.

- [123] C.M. Bishop. *Pattern Recognition and Machine Learning 1st Edition*. Springer, 2013.
- [124] D. Mladenić. *Feature Selection for Dimensionality Reduction*. Springer, 2006.
- [125] H. Liu and H. Motoda. *Feature Extraction, Construction and Selection: A Data Mining Perspective (The Springer International Series in Engineering and Computer Science)*. Springer, 1998.
- [126] N. Sánchez-Maróño, A. Alonso-Betanzos, and M. Tombilla-Sanromán. Filter methods for feature selection: A comparative study. In *Proceedings of the 8th International Conference on Intelligent Data Engineering and Automated Learning, Birmingham, UK*, pages 178–187, 2007.
- [127] T. Fawcett. An introduction to ROC analysis. *Pattern recognition letters*, 27(8):861–874, 2006.
- [128] D.M.W. Powers. Evaluation: From precision, recall and f-measure to ROC, informedness, markedness & correlation. *Journal of Machine Learning Technologies*, 2(1):37–63, 2011.
- [129] I.S. Uzun, A. Amira, and A. Bouridane. FPGA implementations of fast Fourier transforms for real-time signal and image processing. *IEE Proceedings-Vision, Image and Signal Processing*, 152(3):283–296, 2005.
- [130] XILINX. *LogiCORE IP Fast Fourier Transform v7.1*, 2011.
- [131] R. Rojas. *Neural Networks: A Systematic Introduction*. Springer, 1998.
- [132] F. Rosenblatt. The perceptron: A probabilistic model for information storage and organization in the brain. *Psychological Review*, pages 65–386, 1958.
- [133] F. Rosenblatt. *Principles of Neurodynamics: Perceptrons and the Theory of Brain Mechanisms*. Spartan Books, Washington, 1962.
- [134] N. Cristianini and J. Shawe-Taylor. *An Introduction to Support Vector Machines and Other Kernel-based Learning Methods*. Cambridge University Press, 2000.
- [135] W. Cohen. Linear classifiers and the perceptron. 2008.
- [136] G. Bebis and M. Georgiopoulos. Feed-forward neural networks. *IEEE Potentials*, 13(4):27–31, 1994.
- [137] A. Stoykov, J. B. Mosset, U. Greuter, M. Hildebrandt, and N. Schlumpf. Use of Silicon Photomultipliers in ZnS:⁶LiF scintillation neutron detectors: signal extraction in presence of high dark count rates. *JINST*, 9:P06015, 2014.

- [138] A.E. Eiben and S.K. Smit. Parameter tuning for configuring and analyzing evolutionary algorithms. *Swarm and Evolutionary Computation*, 2011.
- [139] K. Pearson. Note on regression and inheritance in the case of two parents. *Proceedings of the Royal Society of London*, 58(347-352):240–242, 1895.
- [140] K. Skahill. *VHDL for programmable logic*. Addison-Wesley, 1996.
- [141] S. Brantschen, M. Pichler, and K. Schenk. *Digitale ASIC Schaltungstechnik. Ein Lehrgang zur Entwicklung von integrierten digitalen Schaltungen und FPGA*. Institut für Mikroelektronik, FHNW, 2008.
- [142] C.H. Roth Jr. and K.J. Lizy. *Digital Systems Design Using VHDL*. Cengage Learning, 2007.
- [143] Y. Nagaraj, K. Shrinivas, K. Veeresh, A. Veeresh, D. Madhu Patil, et al. FPGA implementation of different adder architectures. *International Journal of Emerging Technology and Advanced Engineering*, 2(8), 2012.
- [144] ALTERA. *Datasheet Enpirion®EN63A0QI 12A PowerSoC*, 2016.
- [145] P.B. Andrews. *An introduction to mathematical logic and type theory*. Springer, 2002.

A

A.1 \tilde{U}

$$\begin{aligned}
 & \begin{pmatrix} c_{14}U_{e1} & c_{14}U_{e2} & c_{14}U_{e3} & s_{14} \\ -s_{14}s_{24}U_{e1} + c_{24}U_{\mu1} & -s_{14}s_{24}U_{e2} + c_{24}U_{\mu2} & -s_{14}s_{24}U_{e3} + c_{24}U_{\mu3} & c_{14}s_{24} \\ -c_{24}s_{14}s_{34}U_{e1} - s_{24}s_{34}U_{\mu1} + c_{34}U_{\tau1} & -c_{24}s_{14}s_{34}U_{e2} - s_{24}s_{34}U_{\mu2} + c_{34}U_{\tau2} & -c_{24}s_{14}s_{34}U_{e3} - s_{24}s_{34}U_{\mu3} + c_{34}U_{\tau3} & c_{14}c_{24}s_{34} \\ -c_{24}s_{34}s_{14}U_{e1} - s_{24}c_{34}U_{\mu1} - s_{34}U_{\tau1} & -c_{24}s_{34}s_{14}U_{e2} - s_{24}c_{34}U_{\mu2} - s_{34}U_{\tau2} & -c_{24}s_{34}s_{14}U_{e3} - s_{24}c_{34}U_{\mu3} - s_{34}U_{\tau3} & c_{14}c_{24}s_{34} \end{pmatrix} \\
 & = \\
 & 105
 \end{aligned}$$

(A.1)

A.2 Conventions in Section 5

B – Boolean space

C – Complex space

L_2H – Lebesgue Hilbert or Pre-Hilbert space with L_2 metrics

R – Real space

Superscripts indicate number of elements for vectors, matrices and tensors.

E – class answer vector/matrix

F – feature vector/matrix

w – weight vector/matrix

x, X, \mathbf{X} – discrete signal as acquired by the FPGA. Superscripts indicate the space in which the signal is represented

\hat{Y} – predicted class

$\text{cov}(\cdot, \cdot)$ – covariance

$f(\cdot)$ – trigger function

$g(\cdot)$ – feature extraction

$h(\cdot)$ – machine learning algorithm

$\text{III}(\cdot)$ – sampling function

δ – Dirac function/comb

$|\cdot|$ – cardinality of a set/number of elements within a set

$\lfloor \cdot \rfloor$ – floor function

\cdot – for matrices and tensors, (\cdot) in conjunction with one or more other indices denotes the submatrix or subvector containing all the elements at the indicated location

A.3 Abbreviations

A.3.1 Particles

d – down-quark

e^- – electron

e^+ – positron

ℓ – lepton

n – neutron

p – proton

u – up-quark

W – W boson

α – alpha-particle

γ – gamma/photon

ν – neutrino

μ – muon

τ – tau

A.3.2 Atoms/Molecules/Materials

${}^6\text{LiF} : \text{ZnS}(\text{Ag})$ – Lithium-6 Silver-doped Zinc Sulphide

Am – Americium

Ar – Argon

Be – Beryllium

Bi – Bismuth

Cs – Caesium

Cf – Californium

Cl – Chlorine

Co – Cobalt

Cr – Chromium

Ga – Gallium

Gd – Gadolinium

Ge – Germanium
H – Hydrogen
He – Helium
Li – Lithium
Po – Polonium
Pu – Plutonium
PMMA – polymethyl methacrylate
PVT – polyvinyl toluene
U – Uranium

A.3.3 Physical Quantities

E, e – energy
 L – baseline
 m – mass
 p – momentum
 P – probability, power
 R – data/bit rate
 t – time
 v – speed
 W – work, energy

A.3.4 Units

B – Bel, Byte
bps – bit per second
 c_0 – speed of light in vacuum
eV – Electronvolt
g – gram
Hz – Hertz
 \hbar – reduced Planck constant

m – meter

PA – number of pixel photon avalanches

s – second

W – Watt

°C – degree Celsius

% – percent ($\frac{1}{100}$)

A.3.5 Unit Pre-fixes

n – nano (10^{-9})

μ – micro (10^{-6})

m – milli (10^{-3})

c – centi (10^{-2})

d – deci (10^{-1})

k – kilo (10^3)

M – Mega (10^6)

G – Giga (10^9)

T – Tera (10^{12})

P – Peta (10^{15})

A.3.6 Electronics

ADC – Analogue-Digital Converter

DAQ – Data Acquisition

DC – Direct Current

DCR – Dark-Count Rate

DDR – Double Data Rate

DSP – Digital Signal Processing

CLB – Custom Logic Block

FPGA – Field-Programmable Gate Array

HDL – Hardware Description Language

I²C – Inter-Integrated Circuit
I/O – Input/Output
JTAG – Joint Test Action Group
LVDS – Low-Voltage Differential Signalling
MGT – Multi-Gigabit Transceiver
MPPC – Multi-Pixel Photon Counter
PDE – Photon Detection Efficiency
PMT – Photo Multiplier Tube
RAM – Random -Access Memory
RTL – Register-Transfer Level
SDRAM – Synchronous Dynamic Random-Access Memory
SEU – Single Event Upset
SFP – Small Form-factor Pluggable transceiver
SiPM – Silicon Photomultiplier
SNR – Signal-to-Noise Ratio
SPI – Serial Peripheral Interface
SQNR – Signal-to-Quantisation-Noise Ratio
VHDL – VHSIC Hardware Description Language
VHSIC – Very High Speed Integrated Circuit
WLS – Wavelength-Shifting

A.3.7 Machine Learning

ANN – Artificial Neural Network
FN – False Negative(s)
FP – False Positive(s)
FPR – False Positive Rate
N – Negatives
P – Positives
PPV – Positive Predictive Value
ROC – Receiver Operating Characteristic
TN – True Negative(s)

TP – True Positive(s)

TPR – True Positive Rate

A.3.8 Other

act. – mass of active material

BR2 – Belgian Reactor 2

CDHSW – CERN Dortmund Heidelberg Saclay Warsaw

CERN – European Organization for Nuclear Research

CHORUS – CERN Hybrid Oscillation Research apparatus

CKM – Cabibbo–Kobayashi–Maskawa

C.L. – Confidence Level

DANSS – Detector of the reactor AntiNeutrino based on Solid Scintillator

e.g. – exempli gratia – for example

GALLEX – Gallium Experiment

GNO – Gallium Neutrino Observatory

IBD – Inverse Beta-Decay

ICARUS – Imaging Cosmic And Rare Underground Signals

i.d. – id est – that is

ILL – Institut Laue–Langevin

KamLAND – Kamioka Liquid Scintillator Antineutrino Detector

K2K – KEK to Kamioka

KARMEN – Karlsruhe Rutherford Medium Energy Neutrino experiment

KEK – The High Energy Accelerator Research Organization

LSND – Liquid Scintillator Neutrino Detector

MiniBooNE– Mini Booster Neutrino Experiment

MINOS – Main Injector Neutrino Oscillation Search

NEMENIX – Neutrino Measurement Non-Income Experiment

NOMAD – Neutrino Oscillation Magnetic Detector

NuLat – Neutrino Lattice

pdf – probability distribution function

POSEIDON – Position-Sensitive Detector of Neutrino

PMNS – Pontecorvo–Maki–Nakagawa–Sakata

OPERA – Oscillation Project with Emulsion-tracking Apparatus

r – Pearson’s correlation coefficient

RAA – Reactor Antineutrino Anomaly

Ref – Reference

RENO – Reactor Experiment for Neutrino Oscillation

SAGE – Soviet-American Gallium Experiment

SCK•CEN – Studiecentrum voor Kernenergie • Centre d’Étude de l’énergie Nucléaire

SM – Standard Model

SM1 – SoLid Module 1

SNO – Sudbury Neutrino Observatory

SoLid – Search for oscillations with a Lithium-6 detector

Super-K – Super-Kamiokande

T2K – Tokai to Kamioka

\mathcal{O} – order of

σ – standard deviation